Electric Power Systems Research 96 (2013) 211–217

Contents lists available at SciVerse ScienceDirect

Electric Power Systems Research

journal homepage: www.elsevier.com/locate/epsr

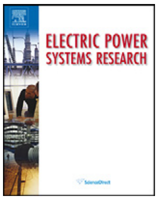

Thermal analysis of electrical contacts from pantograph–catenary system for power supply of electric vehicles

Costica Nituca*

Gheorghe Asachi Technical University of Iasi, Blvd. Dimitrie Mangeron, 73, Iasi 700050, Romania

ARTICLE INFO

Article history:
Received 7 May 2012
Received in revised form 8 October 2012
Accepted 15 November 2012
Available online 29 December 2012

Keywords:
Thermal analysis
Electric contacts
Pantograph–catenary

ABSTRACT

This paper describes a thermal model of electric contacts suitable for power circuits, especially for pantograph–catenary system used to supply the electric vehicles as tramways and trains. Because the contact pieces are made of different materials, the thermal model deals with two different thermal power loss using fractions of the total thermal power. The maximum contact heating and the heating distribution expressions have been established for both contact pieces. This model has been validated for an electric contact between a small pantograph and a copper disc with the aim to simulate the contact between the pantograph and the catenary. The model can be used to analyse the thermal behaviour of electric contacts made of different materials at different values of the electric current, contact force or ambient temperature, in steady-state conditions.

1. Introduction

Thermal analysis of electrical contacts represents an important aspect for many applications. A special domain is the contact between the pantograph and the contact line for the electric vehicles supplied from a catenary system, where the contact is realized between two different materials.

The problems regarding the contact between the pantograph and the contact wire are largely studied in the literature with important results, considering the pantograph–catenary models and simulations [1] but also the thermal aspects. In [2] it is assumed that the contact occurring between contact strip and contact wire is mostly influenced by the dissipated power at the contact due to arcing, friction effect and Joule effect. It establishes a 2D model for the evaluation of the thermal contact between the contact strip and the contact line. It has been concluded that mechanical and electrical parameters (speed, normal force, friction coefficient and current) are the essential parameters governing the heat transfer. There are also studies on the wear of the contact wire and of the collector strip including the thermal aspects [3,4], on the damages of the pantograph–catenary system due to the electrical faults [5] and on the pantograph arcing effects over the vehicle supply [6]. The contact resistance is also largely studied [7], including the electrical contact resistance of pantograph–catenary system in correspondence with the contact force and the electric current [8]. Different materials for the contacts were also studied [9,10] including researches for new contact strip materials [11].

Thermal analyses of electrical contacts are realized for different applications [12–14] but there are limited studies with thermal aspects of the contact between the pantograph and catenary.

Ocoleanu [15] performed a thermal analyses using experimental determination of temperature in contact pantograph–AC contact line for an asymmetric pantograph.

This paper describes a thermal model for heating electrical contacts based on cylindrical model in steady state conditions. The model is applied for a specific application, the contact between pantograph–catenary system used to supply the electric vehicles as trams and trains. The experimental data are determined for the materials used for pantograph (graphite) and contact line (copper). The model can be used to analyse the thermal behaviour of electric contacts made from different materials at different values of the electric current, contact force and ambient temperature, in steady-state conditions.

2. Thermal model

The goal of this study is to develop a mathematical model of a linear electric contact made from two different materials, for instance copper and graphite. A typical application is the linear contact between pantograph and copper contact line from the trams or trains. During this analysis, due to technological reasons for experimental tests, the actual contact line has been simulated with a copper disc. Hence, the linear electric contact is achieved between the pantograph strip made from graphite (material 1, Fig. 1), with frontal plane surface and the copper disc (material 2, Fig. 1), with frontal cylindrical surface, as presented in Fig. 1. These two pieces

---

* Tel.: +40 232 278680; fax: +40 232 254604.

0378-7796/$ – see front matter © 2012 Elsevier B.V. All rights reserved.
http://dx.doi.org/10.1016/j.epsr.2012.11.009

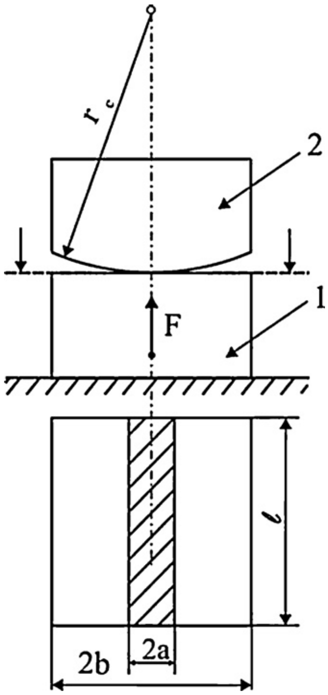

Fig. 1. The linear electric contact; 1 – graphite material and 2 – copper disc.

are in contact because of the press force F. The dimensions of the linear contact can be evaluated through the formula,

$$2al = \frac{F}{H} \tag{1}$$

In the above relation, the dimensions $2a$ and l (Fig. 1), actually mean the width and respectively the length of the rectangle which includes all the contact micro-points. The distance $2b$ means the width of the graphite material and r_c is the radius of the copper disc. In order to obtain the linear contact heating, it is necessary to introduce a physical model for this type of electric contact, as cylindrical model, Fig. 2. Taking into account this model, the contact between the graphite and the copper disc, is established through a cylinder of radius a, and the length l. The radius r_c of the copper disc has a relatively high value (13 cm), this piece being assimilated with a parallelepiped, Fig. 2. The equipotential surfaces have a semi-cylinder shape and the electric current lines are orthogonally on these semi-cylinders.

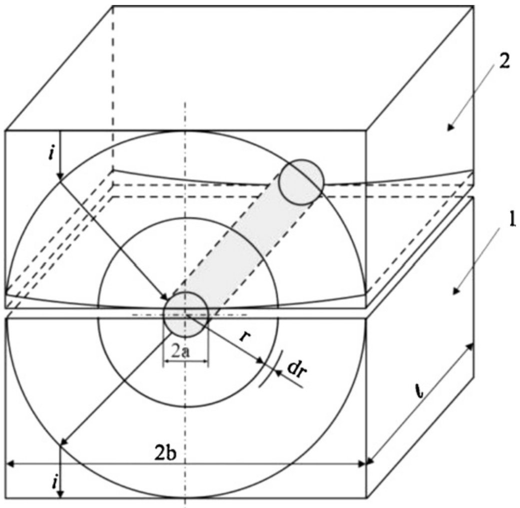

Fig. 2. The cylindrical model for the linear contact; 1 – graphite material and 2 – copper disc.

A three-dimensional stationary temperature field $\theta = \theta(r, \varphi, z)$ in cylindrical coordinates is described as a differential equation of the following type [16]:

$$\lambda\left(\frac{\partial^2\theta}{\partial r^2} + \frac{1}{r}\frac{\partial\theta}{\partial r} + \frac{1}{r^2}\frac{\partial^2\theta}{\partial\varphi^2} + \frac{\partial^2\theta}{\partial z^2}\right) + \rho(\theta)j^2 = 0 \tag{2}$$

where the first term represents the power removed from the element by thermal conduction and the second term means the heating power because of the current flow.

Considering the model symmetry there is no temperature variation with the angle φ, thus $\partial\theta/\partial\varphi = 0$. Also, the thickness of the copper disc is relatively small (5 mm) which means no important variation of the temperature with the coordinate z, so $\partial\theta/\partial z = 0$. Therefore, the temperature field for $r \geq a$, is given by the following equation,

$$\frac{1}{r}\frac{\partial\theta}{\partial r} + \frac{\partial^2\theta}{\partial r^2} + \frac{\rho j^2}{\lambda} = 0 \tag{3}$$

For the electrical resistivity a linear variation with the temperature has been considered [17]

$$\rho = \rho_0[1 + \alpha_R(\theta - \theta_a)] \tag{4}$$

and with the notation for the heating ϑ,

$$\vartheta = \theta - \theta_a \tag{5}$$

the following relation is obtained:

$$\frac{\partial^2\vartheta(r)}{\partial r^2} + \frac{1}{r}\frac{\partial\vartheta(r)}{\partial r} + \frac{\alpha_R\rho_0 I^2}{\lambda\pi^2 l^2}\frac{\vartheta(r)}{r^2} + \frac{\rho_0 I^2}{\lambda\pi^2 l^2}\frac{1}{r^2} = 0 \tag{6}$$

or:

$$r^2\frac{\partial^2\vartheta(r)}{\partial r^2} + r\frac{\partial\vartheta(r)}{\partial r} + m\vartheta(r) + n = 0 \tag{7}$$

This is a non-homogeneous differential equation type Euler and with the substitution,

$$r = e^t \quad \text{or} \quad t = \ln r \tag{8}$$

the above equation becomes:

$$\frac{\partial^2\vartheta(t)}{\partial t^2} + m\vartheta(t) = -n \tag{9}$$

with the solution:

$$\vartheta(t) = A\ \cos(\sigma t) + B\ \sin(\sigma t) - \frac{n}{m} \tag{10}$$

where A and B are integration constants and σ is the complex root of the characteristic equation:

$$p(\sigma) = \sigma^2 + m = 0 \tag{11}$$

Taking into account the substitution (8) and the relation (11), the solution is given by the following equation:

$$\vartheta(r) = A\ \cos(\sqrt{m}\ \ln r) + B\ \sin(\sqrt{m}\ \ln r) - \frac{n}{m} \tag{12}$$

The above solution can be written for both type of materials, copper and graphite, as follows,

$$\begin{aligned} \vartheta_1(r) &= c_1\ \cos(\sqrt{m_1}\ \ln r) + c_2\ \sin(\sqrt{m_1}\ \ln r) - \frac{n_1}{m_1} \\ \vartheta_2(r) &= c_3\ \cos(\sqrt{m_2}\ \ln r) + c_4\ \sin(\sqrt{m_2}\ \ln r) - \frac{n_2}{m_2} \end{aligned} \tag{13}$$

The integration constants c_1, c_2, c_3 and c_4 can be obtained from the following limit conditions. At the boundary, $r = a$, the heating on the graphite side of the contact is equal with the heating on the copper side of the contact and equal with the maximum contact heating $\vartheta_{c\max}$,

$$\vartheta_1(r)\Big|_{r=a} = \vartheta_2(r)\Big|_{r=a} = \vartheta_{c\max} \tag{14}$$

If βP_c, $0 < \beta < 1$, is the fraction of the thermal power P_c (generated at the contact area, due to the contact resistance during current conduction, $P_c = U_c I$), conducted to the graphite side of the contact, then the fraction $(1-\beta)P_c$ is conducted to the copper side of the contact [18]. Therefore, at $r = a$:

$$-\lambda_1 \frac{\partial \vartheta_1}{\partial r}\bigg|_{r=a} = \frac{\beta P_c}{\pi a l}; \quad -\lambda_2 \frac{\partial \vartheta_2}{\partial r}\bigg|_{r=a} = \frac{(1-\beta)P_c}{\pi a l} \tag{15}$$

At the distances $r = r_1$ ($r_1 = 0.04$ m) and $r = r_2$ ($r_2 = 0.04$ m) on the graphite side of the contact and respectively, on the copper side of the contact, there are the heating values ϑ_1 and ϑ_2 which can be established from the measurements [19]:

$$\vartheta_1(r)\Big|_{r=r_1} = \vartheta_1; \quad \vartheta_2(r)\Big|_{r=r_2} = \vartheta_2 \tag{16}$$

From the solutions (13) and the above limit conditions, the following expression for the parameter β, has been obtained:

$$\begin{aligned}\beta = {} & \frac{\pi l}{P_c} \cdot \frac{1}{((tg(\sqrt{m_1}\ln(r_1/a)))/\lambda_1\sqrt{m_1}) + ((tg(\sqrt{m_2}\ln(r_2/a)))/\lambda_2\sqrt{m_2})} \\ & \times \left[\frac{\vartheta_2 + (n_2/m_2)}{\cos(\sqrt{m_2}\ln(r_2/a))} - \frac{\vartheta_1 + (n_1/m_1)}{\cos(\sqrt{m_1}\ln(r_1/a))} + \frac{n_1}{m_1} - \frac{n_2}{m_2}\right] \\ & + \frac{1}{(\lambda_2\sqrt{m_2})/(\lambda_1\sqrt{m_1}) \cdot (tg(\sqrt{m_1}\ln(r_1/a)))/(tg(\sqrt{m_2}\ln(r_2/a))) + 1}\end{aligned} \tag{17}$$

Eq. (17) is valid for different materials and for different dimensions of the contact pieces. If the same material is used for the contact pieces, the parameters α_R, ρ and λ are identical. From Eq. (17) and the limit condition (15), the expression for the maximum contact heating is computed:

$$\begin{aligned}\vartheta_c = {} & \frac{\vartheta_1 + (n_1/m_1)}{\cos(\sqrt{m_1}\ln(r_1/a))} \\ & + \frac{1}{1 + ((\lambda_1\sqrt{m_1})/(\lambda_2\sqrt{m_2})) \cdot (tg(\sqrt{m_2}\ln(r_2/a))/tg(\sqrt{m_1}\ln(r_1/a)))} \\ & \times \left[\frac{\vartheta_2 + (n_2/m_2)}{\cos(\sqrt{m_2}\ln(r_2/a))} - \frac{\vartheta_1 + (n_1/m_1)}{\cos(\sqrt{m_1}\ln(r_1/a))} + \frac{n_1}{m_1} - \frac{n_2}{m_2}\right] \\ & + \frac{P_c}{\pi l} \cdot \frac{1}{(\lambda_1\sqrt{m_1}/tg(\sqrt{m_1}\ln(r_1/a))) + (\lambda_2\sqrt{m_2}/tg(\sqrt{m_2}\ln(r_2/a)))} - \frac{n_1}{m_1}\end{aligned} \tag{18}$$

After computations of the integration constants c_1, c_2, c_3, c_4 and using the equations (13), it results the expressions for the heating distribution in steady-state conditions for both contact pieces:

$$\begin{aligned}\vartheta_1(r) = {} & \frac{1}{\cos(\sqrt{m_1}\ln(r_1/a))}\left[\left(\vartheta_1 + \frac{n_1}{m_1}\right)\cos(\sqrt{m_1}\ln a) + \frac{\beta P_c}{\pi\lambda_1\sqrt{m_1}l}\sin(\sqrt{m_1}\ln r_1)\right]\cos(\sqrt{m_1}\ln r) + \frac{1}{\cos(\sqrt{m_1}\ln(r_1/a))} \\ & \times \left[\left(\vartheta_1 + \frac{n_1}{m_1}\right)\sin(\sqrt{m_1}\ln a) - \frac{\beta P_c}{\pi\lambda_1\sqrt{m_1}l}\cos(\sqrt{m_1}\ln r_1)\right]\sin(\sqrt{m_1}\ln r) - \frac{n_1}{m_1}\end{aligned} \tag{19}$$

$$\begin{aligned}\vartheta_2(r) = {} & \frac{1}{\cos(\sqrt{m_2}\ln(r_2/a))}\left[\left(\vartheta_2 + \frac{n_2}{m_2}\right)\cos(\sqrt{m_2}\ln a) + \frac{(1-\beta)P_c}{\pi\lambda_2\sqrt{m_2}l}\sin(\sqrt{m_2}\ln r_2)\right]\cos(\sqrt{m_2}\ln r) + \frac{1}{\cos(\sqrt{m_2}\ln(r_2/a))} \\ & \times \left[\left(\vartheta_2 + \frac{n_2}{m_2}\right)\sin(\sqrt{m_2}\ln a) - \frac{(1-\beta)P_c}{\pi\lambda_2\sqrt{m_2}l}\cos(\sqrt{m_2}\ln r_2)\right]\sin(\sqrt{m_2}\ln r) - \frac{n_2}{m_2}\end{aligned} \tag{20}$$

3. Discussion of the results

Further on, the influence of the main physical parameters upon contact temperature is analysed. As mentioned in the previous section, the electric contact is made from two pieces, a copper disc with the thickness of 5 mm and the radius about 130 mm. The cross-section of the graphite piece is 20 mm × 15 mm. To compute the heating distribution the following material parameters have been considered: $\rho = 1.73 \times 10^{-8}\ \Omega\,\mathrm{m}$, $\lambda = 393\ \mathrm{W/m\,^\circ C}$, $\alpha = 4 \times 10^{-3}\ /^\circ\mathrm{C}$ for the copper, and $\rho = 1.7 \times 10^{-6}\ \Omega\,\mathrm{m}$, $\lambda = 160\ \mathrm{W/m\,^\circ C}$, $\alpha = 1.3 \times 10^{-3}\ /^\circ\mathrm{C}$ for the graphite.

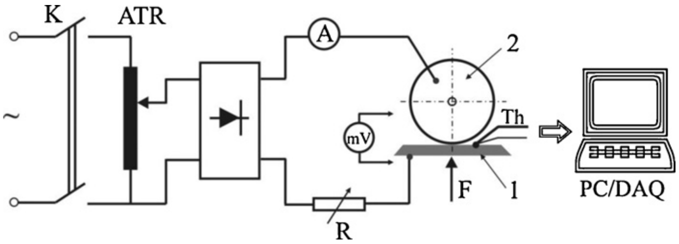

Fig. 3. The main electric circuit for experimental tests; 1 – graphite material and 2 – copper disc.

Heat transfer across the interface of two solids can take place by three different modes: 1 – conduction at the microcontacts, 2 – conduction through the interstitial fluid in the gap between the contacting solids, and 3 – thermal radiation. The radiation heat transfer remains small and can be neglected when surface temperatures are not too high [20]. The interstitial fluid is assumed to be absent, thus the only remaining heat transfer mode is conduction through the micro-contacts.

Due to surface roughness, contact between two surfaces occurs only over microscopic contacts, which are located in the contact plane. The real area of contact, i.e., the total area of microcontacts, is a small fraction of the nominal contact area, typically a few percent [21,22]. Heat flow is constricted to pass through the macrocontact and then microcontacts. This phenomenon is observed through a relatively high temperature drop across the interface between the electrical contact pieces. However, many service failures of sliding contacts occur by slow chemical and metallurgical reactions at the contact area and the influence which this temperature rise has on the reaction rate can significantly affect long term operating performance of the pantograph–catenary system.

In order to compute the values for the parameter β, and especially, for the heating distribution $\vartheta(r)$ and $\vartheta(r)$, on both contact pieces, copper and graphite, some measurements of the voltage drop on electric contact have been performed. An electric circuit diagram used for experimental tests is shown in Fig. 3. The main switch K, supplies with low voltage the autotransformer ATR. Using a power rectifier bridge, the direct current is obtained through the power circuit. The current value is measured by the ammeter A, and its value can be adjusted through the power variable resistor R. Also, the current value can be varied from the secondary voltage of the autotransformer ATR. The main direct current flows through the power resistor R, graphite piece 1 and the copper disc 2 and

Table 1
Experimental data for voltage drop and heating for limit conditions at different currents and contact forces.

	F [N]								
	10			20			30		
	U_c [V]	ϑ_1 [°C]	ϑ_2 [°C]	U_c [V]	ϑ_1 [°C]	ϑ_2 [°C]	U_c [V]	ϑ_1 [°C]	ϑ_2 [°C]
I = 15 A	0.47	10.1	8.7	0.33	8.9	7.7	0.285	8.2	6.8
I = 25 A	0.69	21.7	16.0	0.44	19.1	15.3	0.38	18.4	13.9
I = 40 A	0.98	46.1	31.9	0.7	37.4	26.1	0.557	33.5	24.4

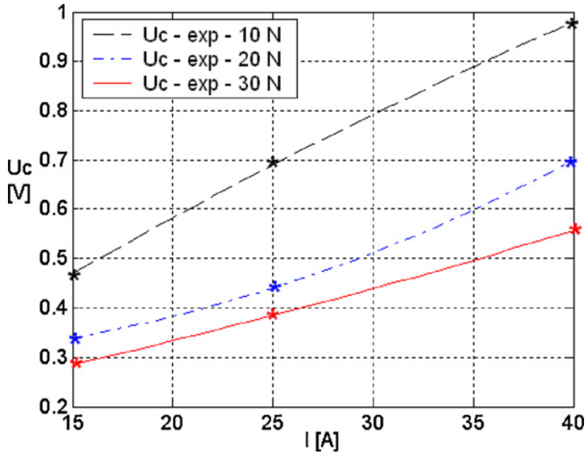

Fig. 4. The voltage drop variation against electric current at different contact forces (10 N, 20 N and 30 N).

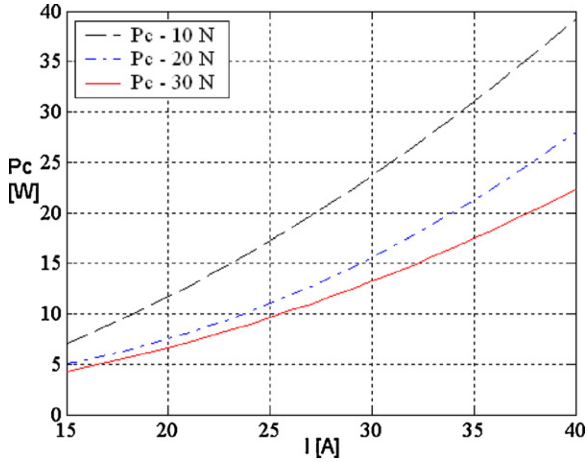

Fig. 5. Contact power loss variation against electric current at different contact forces (10 N, 20 N, 30 N).

back to the power rectifier bridge. The voltage drop on the electric contact can be measured with a milli-voltmeter mV. The contact force F can be varied through a controlled electromagnetic device type actuator.

Hence, the voltage drop values have been measured at different electric current (15–40 A) and contact force values (10–30 N). The results are reported in Table 1 and the voltage drop variation against current values at different contact forces is presented in Fig. 4. It is to observe that contact voltage drop increases when the electric current increases too. On the other hand, when the contact force increases, the voltage drop decreases. This is explained by the fact that, on the electric contact areas, when the contact force increases, the contact resistance decreases, thus, the contact voltage drop decreases too. The same observations apply to the contact power losses ($P_c = U_c I$) variation against electric current at different contact forces, Fig. 5. The power loss has a higher increase than the voltage drop (Fig. 4) at the same electric current increasing. This is explained through the fact that the power loss actually has a parabolic variation with the electric current which flows through the contact ($P_c = R_c I^2$). After contact's voltage drop values have been measured, the parameter β and the heating distribution have been computed. The variations of the parameter β against electric current at different contact forces are presented in Fig. 6. It is to observe that the fraction of the thermal power in the contact decreases when the electric current increases. Also, when the contact force increases from 10 to 30 N, the fraction of the power loss in the contact decreases (i.e., from about 0.22 to 0.18 at electric current of 15 A). It implies that when the contact force increases, the fraction of the thermal power loss in the contact becomes more important to the copper side of the electric contact.

From Figs. 7–9, the temperature rise distributions at different current and force contact values are presented. There is a maximum heating in the middle of the electric contact and then the heating decreases both on copper and graphite contact side. In all cases, the decreasing of the temperature rise is more emphasized on the copper side, because the copper has a thermal conductivity (393 W/m °C) bigger than the graphite one (160 W/m °C). The heating has the higher values at less contact force, 10 N, Fig. 7. In this situation, the maximum heating ϑ is about 61.2 °C for an electric current of 40 A, and decreases to 31 °C on the copper side at a distance of 50 mm from the contact centre. On the graphite side, the decreasing is only up to 45.4 °C at the same distance of 50 mm from the contact centre. At a current value of 25 A, the maximum heating is about 28.8 °C and at 15 A, the highest value for the heating is 13.6 °C. In case when the contact force is 20 N, Fig. 8, the maximum heatings are 47.5, 23.6 and 11.3 °C for the current values of 40, 25 and 15 A, respectively. For the situation when the contact force is 30 N, Fig. 9, the heating has the following maximum values: 41.6, 21.5 and 10 °C when the electric current is 40, 25 and 15 A, respectively. It is to notice that when the contact force increases,

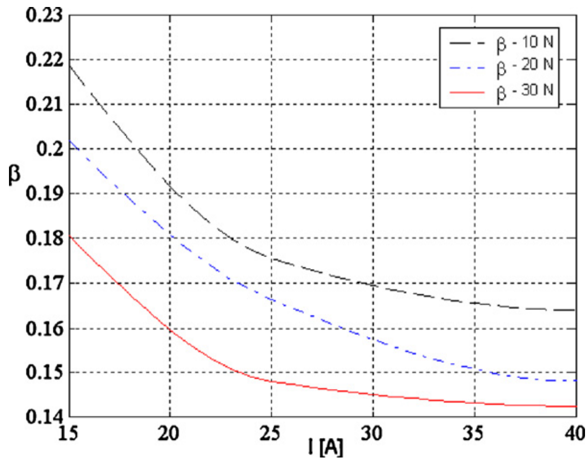

Fig. 6. The fraction of the contact thermal power variation against electric current at different contact forces (10 N, 20 N and 30 N).

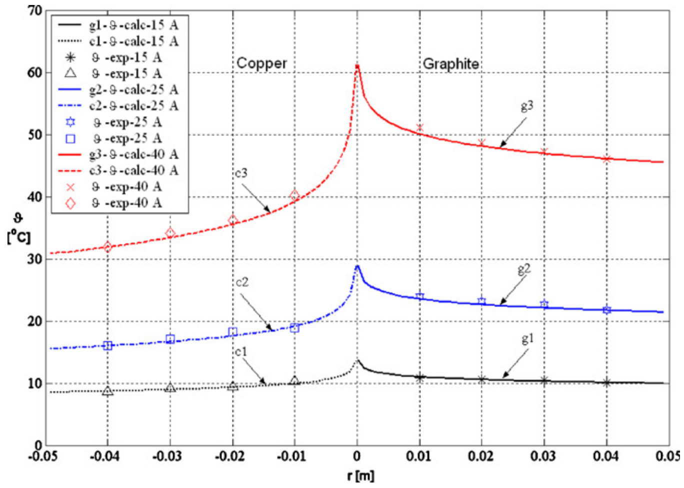

Fig. 7. Heat distribution at different current values (15, 25 and 40 A) and contact force of 10 N. Comparison between computed (g(c)1(2)(3)-ϑ-calc-15 A, g(c)1(2)(3)-ϑ-calc-25 A and g(c)1(2)(3)-ϑ-calc-40 A) and experimental values (ϑ-exp-15 A, ϑ-exp-25 A and ϑ-exp-40 A).

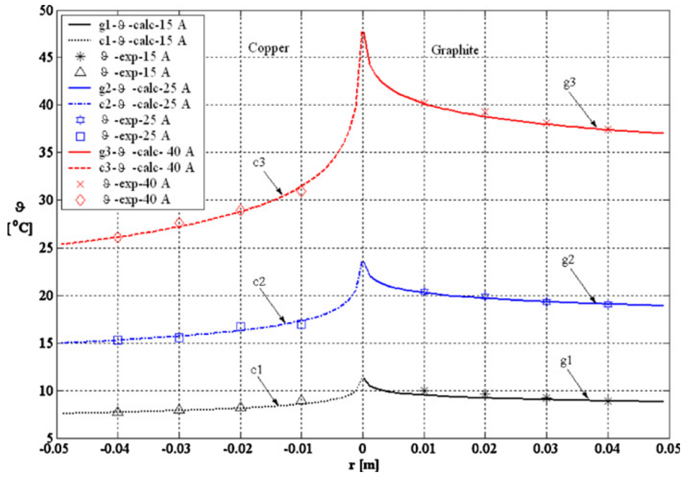

Fig. 8. Heat distribution at different current values (15, 25 and 40 A) and contact force of 20 N. Comparison between computed (g(c)1(2)(3)-ϑ-calc-15 A, g(c)1(2)(3)-ϑ-calc-25 A and g(c)1(2)(3)-ϑ-calc-40 A) and experimental values (ϑ-exp-15 A, ϑ-exp-25 A and ϑ-exp-40 A).

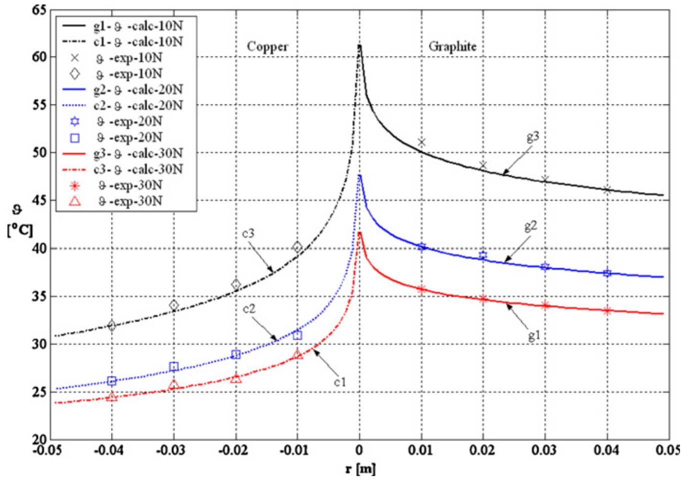

Fig. 9. Heat distribution at different current values (15, 25 and 40 A) and contact force of 30 N. Comparison between computed (g(c)1(2)(3)-ϑ-calc-15 A, g(c)1(2)(3)-ϑ-calc-25 A and g(c)1(2)(3)-ϑ-calc-40 A) and experimental values (ϑ-exp-15 A, ϑ-exp-25 A and ϑ-exp-40 A).

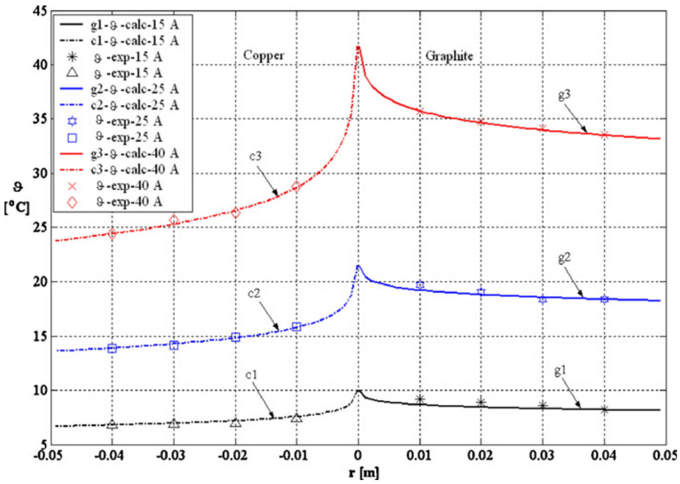

Fig. 10. Heat distribution at different contact force values (10, 20 and 30 N) and electric current of 40 A. Comparison between computed (g(c)1(2)(3)-ϑ-calc-10 N, g(c)1(2)(3)-ϑ-calc-20 N and g(c)1(2)(3)-ϑ-calc-30 N) and experimental values (ϑ-exp-10 N, ϑ-exp-20 N, and ϑ-exp-30 N).

the maximum heating decreases for the same current value. This is explained because at electric contacts when the press force is increased, the contact resistance decreases. Therefore, the thermal contact power loss decreases and finally, the heating decreases too. This observation is outlined in the Fig. 10 which presents the heating distribution at different contact force values, from 10 to 30 N, but at the same electric current of 40 A. As mentioned for the above figures, there is an important decreasing of the temperature rise on the copper side because its thermal conductivity is bigger than the graphite one. It can be noticed when the contact force increases from 10 to 30 N, the maximum heating decreases from 61.2 to 41.6 °C.

Moreover, for the cylindrical model, it was analysed the heat distribution on the two contact pieces, copper and graphite, for different geometrical values 2*a* and *l*. In Fig. 11 it is presented the heat distribution at different values of the copper disc thickness (*l*1 = 2 mm, *l*2 = 5 mm, *l*3 = 8 mm), a contact force of 10 N and for different current values (15 A, 25 A, 40 A). It is to notice the highest heat values of the maximum heat when the thickness is *l*1 = 2 mm, with different heat values depending on current: 19.1 °C (ϑg-15 A),

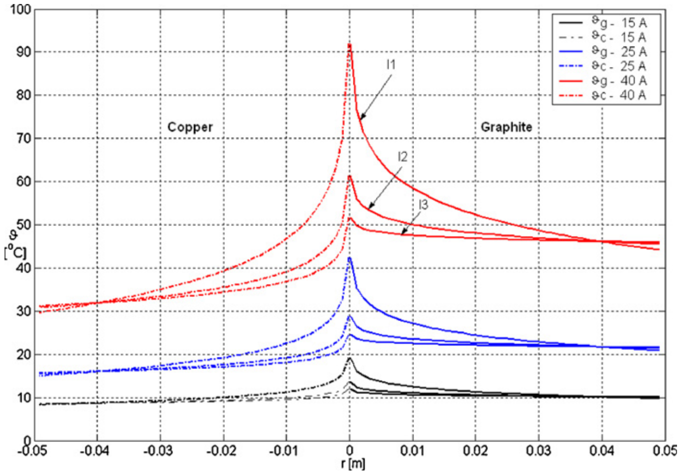

Fig. 11. Heat distribution at different length values (*l*1 = 2 mm, *l*2 = 5 mm, and *l*3 = 8 mm) and contact force of 10 N. Comparison between different current values (ϑg,c-15 A, ϑg,c-25 A, and ϑg,c-40 A).

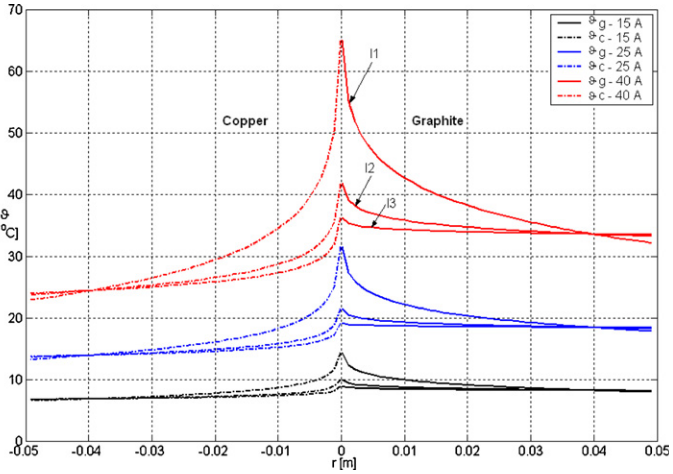

Fig. 12. Heat distribution at different length values (*l*1 = 2 mm, *l*2 = 5 mm, and *l*3 = 8 mm) and contact force of 30 N. Comparison between different current values (ϑg,c-15 A, ϑg,c-25 A, and ϑg,c-40 A).

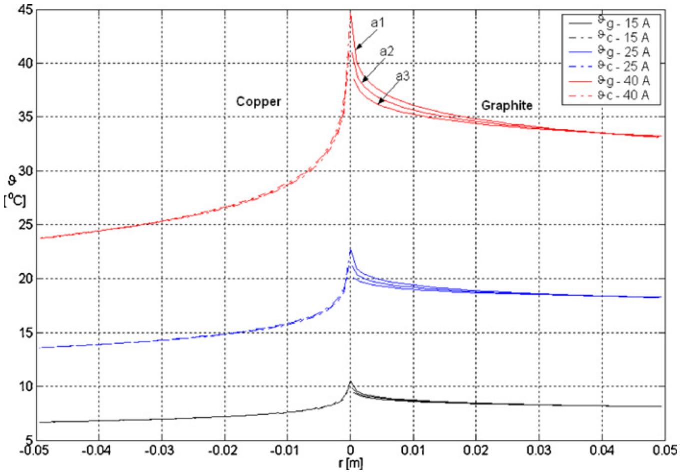

Fig. 14. Heat distribution at different radius values (*a*1 = 0.15 mm, *a*2 = 0.2 mm, and *a*3 = 0.5 mm) and contact force of 30 N. Comparison for different current values (ϑg,c-15 A, ϑg,c-25 A, and ϑg,c-40 A).

42.5 °C (ϑg-25 A) and respectively 92.6 °C (ϑg-40 A). By comparison, Fig. 12 presents the same heat distribution but for a force of 30 N. As it expected, the maximum heat values for all three currents are lower than the previous case. Thus, the maximum heat values for *l*1 = 2 mm are 14.3 °C (ϑg-15 A), 31.6 °C (ϑg-25 A) and respectively 65.2 °C (ϑg-40 A).

Fig. 13 presents the heat variation at different radius values of the cylindrical model (*a*1 = 0.15 mm, *a*2 = 0.2 mm, *a*3 = 0.5 mm), for a contact force of 10 N and the same currents as in previous cases, (ϑg,c-15 A, ϑg,c-25 A, ϑg,c-40 A). It is to notice that for *I* = 15 A and *I* = 25 A, the heat distribution is identically for both contact pieces, copper and graphite (ϑg,c-15 A, ϑg,c-25 A). For the graphite, when the current is 40 A and the distance is less than 0.02 m, there are some differences between the heat for all values of the radius (ϑg,c-40 A), but for the copper there are very small variations, Fig. 13. By comparison, Fig. 14 presents the same heat distribution when the contact force is 30 N. The maximum heat values are lower than the previous case: 10.7 °C (ϑg-15 A), 22.7 °C (ϑg-25 A) and respectively 45 °C (ϑg-40 A). As in previous case, there are almost identically heat values for different radius, especially for the copper. Only for a current of 40 A and the distance less than 0.02 m it is to notice some differences between the heat values.

Considering the influence of the ambient temperature onto the contact line [23] the temperature distribution is presented in Fig. 15. It has considered the maximum test current of 40 A and the maximum contact force of 30 N. The ambient temperature has been varied from 5 to 40 °C. It results a maximum temperature variation from 46.6 to 81.6 °C. Actually, there is a translation of the temperature curves both for copper and graphite side of the contact pieces when the ambient temperature varies.

With the aim to validate the thermal model, some experimental tests have been done. Using proper thermocouples Th, type K, the temperatures on the copper disc and graphite bar have been acquired. The small voltage signals provided by thermocouples have been amplified using a signal conditioning board type AT2F-16. The amplified signal was the input for a data acquisition board type PC-LPM-16. The testing current had the values ranging from 15 to 40 A and the contact force has been adjusted from the 10 to 30 N. The measurement points have been considered at 10, 20, 30 and 40 mm from the contact centre for both sides of the electric contact.

When the contact force was 10 N, Fig. 7, the heating experimental data (ϑ-exp-40 A) at 10 mm from the contact centre for graphite side is 51.7 °C and for copper side is 40.3 °C. The computed heating values at the same distance and the same test current of 40 A,

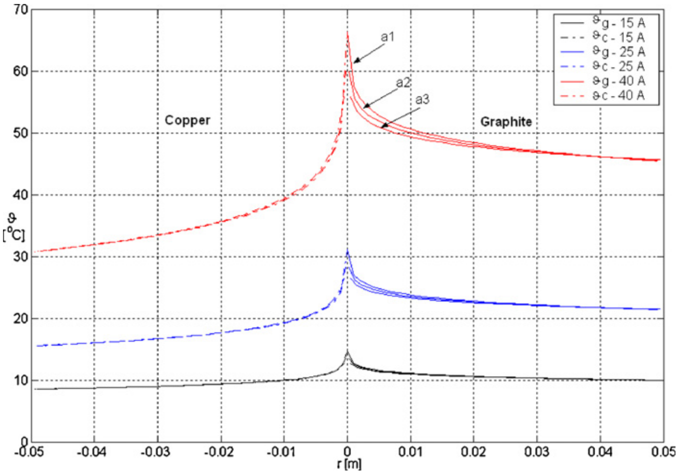

Fig. 13. Heat distribution at different radius values (*a*1 = 0.15 mm, *a*2 = 0.2 mm, and *a*3 = 0.5 mm) and contact force of 10 N. Comparison for different current values (ϑg,c-15 A, ϑg, -25 A, and ϑg,c-40 A).

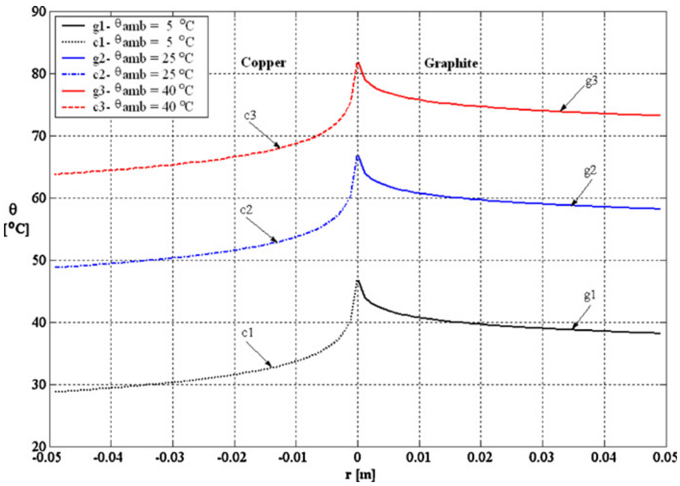

Fig. 15. Temperature distribution at different ambient temperature (5, 25 and 40 °C), electric current of 40 A and contact force of 30 N.

are: 50 °C on graphite side (g3-ϑ-calc-40 A) and 39.1 °C on copper side (c3-ϑ-calc-40 A). At the distance of 40 mm from the contact centre, the heating experimental data is 46.5 °C for graphite side and 32.1 °C for copper side. These values are very close to the computed ones: 46.3 °C – graphite and 32 °C – copper. Hence, in the case of current value of 40 A, the big differences between experimental and computed heating values are at small distance from the contact centre (10 mm) and there are very small differences between heating values at big distance from the contact centre (40 mm). When the test current is decreased at 15 A, the variations between experimental (ϑ-exp-15 A) and computed heating values on graphite side (g1-ϑ-calc-15 A) and copper side (c1-ϑ-calc-15 A) at 10 mm from the contact centre, are very small: 0.25 °C – graphite and 0.48 °C – copper. At 40 mm distance from the contact centre, the differences between experimental and computed heating values on graphite side (0.16 °C) and copper side (0.20 °C) are very small too. Therefore, when the tested current decreases, the differences between experimental and computed heating values decrease too. The same conclusion can be outlined in the case of tested current of 40 A and different contact forces, Fig. 10. At contact force of 30 N and 10 mm distance from the contact centre, the differences between experimental (ϑ-exp-30 N) and computed heating values are 1.43 °C on graphite side (g3-ϑ-calc-30 N) and 1.12°C on copper side (c3-ϑ-calc-30 N). At 40 mm distance from the contact centre, the differences between experimental and computed heating values are 0.14 °C on graphite side and 0.08 °C on copper side. When the contact force is 10 N, the differences between experimental and computed heating values at both 10 or 40 mm distance from the contact centre, are very small (around 0.12 °C).

In the situations when the contact force is 20 N, Fig. 8, and 30 N, Fig. 9, it is to be observed that there are no important differences between experimental data (ϑ-exp-15(25)(40)A) and computed heating values on both graphite side (g1(2)(3)-ϑ-calc-15(25)(40)A) and copper side (c1(2)(3)-ϑ-calc-15(25)(40)A) at both 10 or 40 mm distance from the contact centre. On the other hand, the differences between the temperature values resulting from experimental tests and those obtained during computations are due to various factors: measurement errors, thermal model simplifications and mounting test conditions. Nevertheless, the maximum difference between the experimental and computation results is less than 2 °C.

4. Conclusion

To understand and to optimize the operating mechanisms of pantograph–catenary interaction, the thermal behaviour of the electric contacts and its application are of major interest. A thermal model has been proposed in order to evaluate the temperature distribution on the electric contact made from different materials in steady-state conditions. The contact thermal model allows establishing the heating values near the contact centre on the both sides of the contact at different values of the electric current, contact force or ambient temperature. The model can be used to evaluate the maximum heating of the electric contact and to design new types of contacts with a better heating distribution under different mechanical or electrical stresses.

Appendix A. List of symbols

F	contact force
H	material hardness
l	length of the linear contact (disc thickness)
a	cylinder radius of linear contact model
U_c	contact voltage drop
I	electric current through the contact
r_c	contact resistance
j	current density
ρ	electrical resistivity
λ	thermal conductivity
θ	temperature
θ_a	ambient temperature.
α_R	coefficient of electrical resistivity variation with temperature
m_1	by definition $m_1 = \frac{\alpha_{R1}\rho_{01} I^2}{\lambda_1 \pi^2 l^2}$
n_1	by definition $n_1 = \frac{\rho_{01} I^2}{\lambda_1 \pi^2 l^2}$
m_2	by definition $m_2 = \frac{\alpha_{R2}\rho_{02} I^2}{\lambda_2 \pi^2 l^2}$
n_2	by definition $n_2 = \frac{\rho_{02} I^2}{\lambda_2 \pi^2 l^2}$

References

[1] A. Collina, S. Bruni, Numerical simulation of pantograph–overhead equipment interaction, Vehicle System Dynamics 38 (2002) 261–291, Swets & Zeitlinger.

[2] S. Walters, A. Rachid, A. Mpanda, On modelling and control of pantograph catenary systems, in: International conference on Pantograph Catenary Interaction Framework for Intelligent Control, PACIFIC 2011, Amiens, 2011.

[3] G. Bucca, A. Collina, A procedure for the wear prediction of collector strip and contact wire in pantograph–catenary system, Wear 266 (2009) 46–59.

[4] T. Ding, G.X. Chen, X. Wang, M.H. Zhu, W.H. Zhang, W.X. Zhou, Friction and wear behavior of pure carbon strip sliding against copper contact wire under AC passage at high speeds, Tribology International 44 (2011) 437–444.

[5] V. Mihalcea, L. Cantemir, C.G. Cantemir, G. Chiriac, The necessity of current collecting study at the pantograph of the electric locomotive in real conditions, vol. 5, Buletinul Institutului Politehnic Iaşi L (LIV), Fasc., 2004, pp. 1159–1164.

[6] A. Plesca, About o new type of fuse based on the controllable fusing effect, Advances in Electrical and Computer Engineering Journal 9 (2009) 34–37.

[7] D. Bansal, Tribological investigation of electrical contacts, Doctoral thesis, Georgia Institute of Technology, 2009.

[8] W. Wang, A. Dong, G. Wu, G. Gao, L. Zhou, B. Wang, Y. Cui, D. Liu, D. Li, T. Li, Study on characterization of electrical contact between pantograph and catenary, in: 57th Holm Conference on Electrical Contacts (Minneapolis), 2011, pp. 1–6.

[9] M. Susan, L.G. Bujoreanu, The metal–tool contact friction at the ultrasonic vibration drawing of ball-bearing steel wires, Revista de Metalurgia 35 (1999) 379–383.

[10] L.G. Bujoreanu, On the influence of austenitization on the morphology of α-phase in tempered Cu–Zn–Al shape memory alloys, Materials Science and Engineering A 481–482 (2008) 395–403.

[11] D.H. Hea, R. Manory, A novel electrical contact material with improved self-lubrication for railway current collectors, Wear 249 (2001) 626–636.

[12] M. Bahrami, J.R. Culham, M.M. Yovanovich, Modeling thermal contact resistance: a scale analysis approach, Journal of Heat Transfer 126 (2004) 896–905.

[13] M.H. Shojaefard, M. Ghaffarpour, A.R. Noorpoor, Thermal contact analysis using identification method, Heat Transfer Engineering 29 (1) (2008) 85–96.

[14] C. Fieberg, R. Kneer, Determination of thermal contact resistance from transient temperature measurements, International Journal of Heat and Mass Transfer 51 (2008) 1017–1023.

[15] C.F. Ocoleanu, I. Popa, Gh. Manolea, A.I. Dolan, S. Vlase, Temperature investigation in contact pantograph – AC contact line, International Journal of Circuits, Systems and Signal Processing 3 (2009) 154–163.

[16] A. Plesca, Busbar heating during transient conditions, Electric Power Systems Research 89 (2012) 31–37.

[17] A. Plesca, Numerical thermal analysis of fuses for power semiconductors, Electric Power Systems Research 83 (2012) 144–150.

[18] M.P. Paisios, C.G. Karagiannopoulos, P.D. Bourkas, Model for temperature estimation of dc-contactors with double-break main contacts, Simulation Modelling Practice and Theory 15 (2007) 503–512.

[19] A. Plesca, Busbar temperature monitoring and correlation with protection electrical apparatus, International Review of Electrical Engineering 6 (2011) 2659–2665, Praise Worthy Prize.

[20] L. Kogut, K. Komvopoulos:, Electrical contact resistance theory for conductive rough surfaces separated by a thin insulating film, Journal of Applied Physics 95 (2004) 576–585.

[21] C.G. Aronis, C.S. Psomopoulos, C.G. Karagiannopoulos, P.D. Bourkas, A model regarding electrical contacts in advance degradation, International Journal of Modelling and Simulation 26 (2006) 169–173.

[22] C.G. Karagiannopoulos, C.S. Psomopoulos, P.D. Bourkas, A theoretic and experimental investigation in stationary electric contacts, Inst. of Phys. Pub., Modelling and Simulation in Materials Science and Engineering 9 (2001) 181–192.

[23] C. Niţucă, L. Cantemir, G. Chiriac, A. Gheorghiu, Aspects regarding the influence of the temperature range over the contact line, vol. 5, Buletinul Institutului Politehnic Iaşi, L (LIV), Fasc., 2004, pp. 1165–1170.

Hindawi
Modelling and Simulation in Engineering
Volume 2018, Article ID 7329014, 12 pages
https://doi.org/10.1155/2018/7329014

Research Article

Numerical Analysis of a Real Photovoltaic Module with Various Parameters

Costica Nituca,[1] Gabriel Chiriac ,[1] Dumitru Cuciureanu,[2] Guoqiang Zhang,[3] Dong Han,[3] and Adrian Plesca[1]

[1] *Faculty of Electrical Engineering, "Gheorghe Asachi" Technical University of Iasi, Profesor Dimitrie Mangeron, No. 23, 700050 Iasi, Romania*
[2] *Q SRL, Stradela Sfantul Andrei, No. 13, Iasi, Romania*
[3] *Institute of Electrical Engineering, Chinese Academy of Sciences, No. 6, Beiertiao, Zhongguancun, Beijing, China*

Correspondence should be addressed to Gabriel Chiriac; gchiriac@tuiasi.ro

Received 19 December 2017; Accepted 29 January 2018; Published 20 March 2018

Academic Editor: Ricardo Perera

This article presents a real photovoltaic module with modeling and simulations starting from the model of a photovoltaic (PV) cell. I-V, P-V, and P-I characteristics are simulated for different solar irradiation, temperatures, series resistances, and parallel resistances. For a real photovoltaic module (ALTIUS Module AFP-235W) there are estimated series and parallel resistances for which the energetical performances of the module have optimal values for a solar radiation of 1000 W/m^2 and a temperature of the environment of 25°C. Temperature influence over the PV module performances is analyzed by using a thermal model of the ALTIUS Module AFP-235W using the finite element method. A temperature variation on the surface of the PV module is starting from a low value 40.15°C to a high value of 52.07°C. Current and power estimation are within the errors from 1.55% to about 4.3%. Experimental data are measured for the photovoltaic ALTIUS Module AFP-235W for an entire daylight.

1. Introduction

Solar energy is a renewable and no pollution energy with a significant annual riseup and this trend follows an ascending path. Locally produced renewable energy is more and more promoted as a key to the affordable and sustainable energy in remote area, in small communities, or for small consumers even into the large cities. Photovoltaic systems are realized form photovoltaic (PV) cells; one of the major advantages of photovoltaic cells is that they are highly modular and by proper scaling, they can be expected to provide adequate power for various loads [1]. These cells depend on photovoltaic effect for converting solar radiation into electricity and the generated photocurrent is proportional to the solar irradiation [2]. The output characteristics of a PV cell are nonlinear and fluctuate with solar radiation, cell temperature, series and parallel resistance, and other parameters of the mathematical model [3].

The modeling and simulation of the photovoltaic modules began long ago, but improvements of these models are analyzed and presented continually [2, 4–6]. The implementation of mathematical model of photovoltaic cell into specialized software MATLAB-Simulink is widely used. The computing models are realized by using the equations for the parameters as thermal voltage, photovoltaic current, diode saturation current, and ideality factor. The main characteristics can be obtained, such as the current-voltage (I-V) and power-voltage (P-V) characteristics [1, 4, 7–10]. The series and parallel resistances have an important influence over the PV cell parameters and these resistances are considered into the mathematical models, but in some cases [11–13] the series resistance is neglected into the model and in some cases [13–17] the parallel resistance is neglected. Thermal analysis of the photovoltaic panels is an important part of the studies in order to estimate the temperature distribution in a PV module and to determine the operating temperature of solar system accurately. Optical parameters for the reflectivity, transmissivity, and absorptivity for the relevant layers of the module are taken into account to determine the heat dissipation in the areas exposed directly to sunlight. Heat losses by convection and radiation are also included in simulations [18]. Finite element analysis is considered by

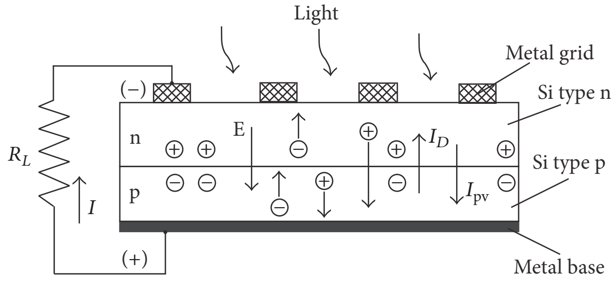

Figure 1: Physical structure of the photovoltaic cell.

many researchers [18–21]. Also empirical models are used for the photovoltaic devices [22].

Different studies consider cooling system in order to reduce the operating temperature of the PV panel and to increase the performance of it [19, 23, 24].

In this article a model of the photovoltaic module is developed and the influence of some parameters are analyzed as series and parallel resistances, temperature, and solar irradiation over the PV module output characteristics. Simulations of module characteristics are realized considering the real data of a PV module ALTIUS AFP 235 and a thermal analysis and thermal simulation is also realized. There are also some experimental data analyzed and registered for an ALTIUS 235 module which is in regular use. The authors outline the variation of main electrical characteristics of a real PV module depending on solar radiation and also the correlation of the suitable functionality of the PV module with the temperature.

2. Modeling the Photovoltaic Module

2.1. Ideal PV Cell. The photovoltaic (PV) cell is considered as a semiconductor diode which is exposed to the solar radiation (Figure 1). A part of this radiation is absorbed by the *pn* junction creating pairs of electron hole. These electrical charges are separated by the electric field E: the electrons migrate in the "*n*" area and the holes migrate in the "*p*" area. This separation is the photovoltaic effect and it generates an electric current. This situation can be modeled into a simplified model having a current source in parallel with an ideal diode, with a photovoltaic current I_{pv} and a diode current I_D. Practical aspects of the PV cell can be studied considering a single-diode PV model with a series resistance R_s and a parallel resistance R_p (Figure 2).

The main equations to describe the I-V characteristics of an ideal PV cell are [1, 4, 7]

$$I = I_{\text{pv}} - I_D, \quad (1)$$

$$I_D = I_0\left[\exp\left(\frac{qV}{akT} - 1\right)\right], \quad (2)$$

$$I = I_{\text{pv}} - I_0\left[\exp\left(\frac{qV}{akT}\right) - 1\right]. \quad (3)$$

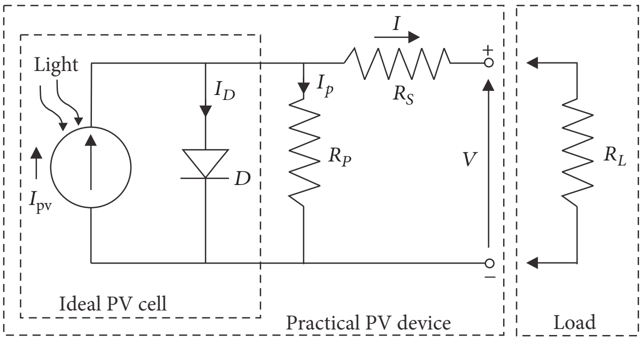

Figure 2: Equivalent model of a PV cell.

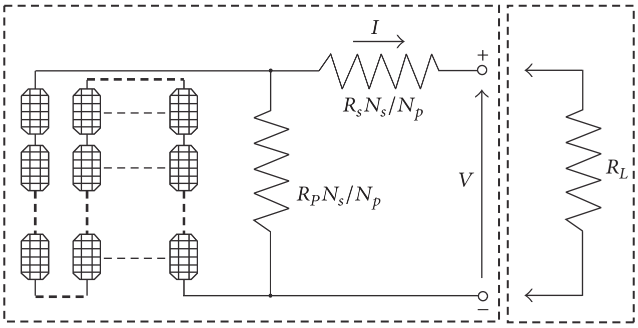

Figure 3: The PV module equivalent circuit model.

2.2. Modeling the PV Module. Many researches [1, 5, 9, 10] show that, for the analysis of the PV cells, there are some necessary supplementary parameters to be used into (3):

$$I = I_{\text{pv}} - I_0\left[\exp\left(\frac{V + R_sI}{aV_T}\right) - 1\right] - \frac{V + R_sI}{R_p}, \quad (4)$$

where

$$V_T = \frac{kT}{q}. \quad (5)$$

In order to assure the parameters required on the consumers, a photovoltaic system has to be made by a sufficient number of PV cells, connected in series or in parallel, usually called modules or arrays. Figure 3 presents the equivalent circuit model of a photovoltaic system.

For the structure module in Figure 3, (4) will be [5, 8]

$$I = I_{\text{pv}}N_p - I_0N_p\left[\exp\left(\frac{V + IR_s\left(N_s/N_p\right)}{aV_TN_s}\right) - 1\right] - \frac{V + IR_s\left(N_s/N_p\right)}{R_p\left(N_s/N_p\right)}. \quad (6)$$

Based on the same characteristic, the following items are to be considered as well: the open circuit voltage/temperature coefficient (K_V), the short circuit current/temperature coefficient (K_I), and the maximum experimental peak output power ($P_{\max,e}$) [5]. These aspects are related to the nominal condition

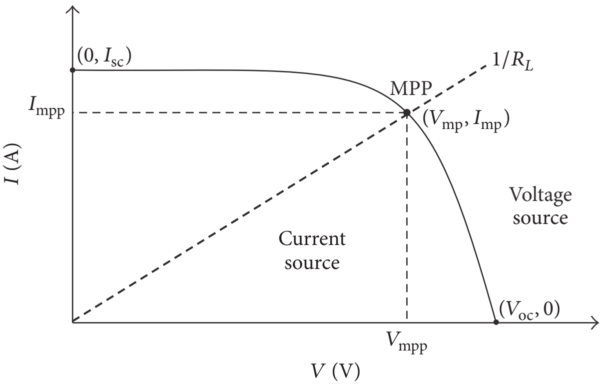

FIGURE 4: I-V characteristic of a practical photovoltaic device.

or to the Standard Test Conditions (STC). In these conditions the photovoltaic device has series resistances R_s with a strong impact when the system operates in the voltage source area and a parallel resistance R_p with a strong influence when the system operates in the current source area. In some cases [11–13] the R_s resistance is neglected into the model and in some cases [13–17] the R_p resistance is neglected.

For some points on the characteristic in Figure 4 (the short circuit $(0, I_{sc})$, open circuit $(V_{0c}, 0)$, and Maximum Power Point (V_{mpp}, I_{mpp})), the relations it can be written as follows[9]:

$$\begin{aligned} 0 &= I_{pv,n} - I_{0,n}\left[\exp\left(\frac{V_{0c,n}}{V_{T,n}}\right) - 1\right], \\ I_{mpp,n} &= I_{pv,n} - I_{0,n}\left[\exp\left(\frac{V_{mpp,n} + R_s I_{mpp,n}}{V_{T,n}}\right) - 1\right]. \end{aligned} \tag{7}$$

The current generated by the photovoltaic panel depends directly on the solar irradiation and is influenced by the temperature according to the next relation [26, 27]:

$$I_{pv} = \left(I_{pv,n} + K_I \Delta T\right)\frac{G}{G_n}, \tag{8}$$

where

$$\Delta T = T - T_n. \tag{9}$$

The nominal open voltage can be influenced by the temperature according to the relation [14]:

$$V_{0c} = V_{0c,n}\left(1 + K_V \Delta T\right) + V_T \ln\left(\frac{G}{G_n}\right). \tag{10}$$

The saturation current of the diode depends also on the temperature [5, 28, 29]:

$$I_0 = I_{0,n}\left(\frac{T_n}{T}\right)^3 \exp\left[\frac{qE_g}{ak}\left(\frac{1}{T_n} - \frac{1}{T}\right)\right], \tag{11}$$

where E_g is the band gap energy of the semiconductor (E_g = 1.12 eV for the polycrystalline Si at 25°C). The value of the saturated nominal current is given by [5]

$$I_{0,n} = \frac{I_{sc,n}}{\exp\left(V_{0c,n}/aV_{T,n}\right) - 1}. \tag{12}$$

Some researches [5, 30, 31] suggest an improving of the saturation current on the diode established by (10). The current $I_{pv,n}$ can be assumed to be approximately equal to I_{sc}, which is a very common assumption in PV modeling [5]. The assumption gives a good approximation because the series resistance is usually very small and the parallel resistance is large [5, 10]. In these conditions the saturation current on diode becomes

$$I_0 = \frac{I_{sc,n} + K_I \Delta T}{\exp\left(\left(V_{0c,n} + K_V \Delta T\right)/aN_c V_t\right) - 1}. \tag{13}$$

The performances of a PV cell depend also on the fill factor (FF), which is the ratio between the Maximum Power of a cell and the power of an ideal PV cell in the same operating conditions.

For a variable resistive load R_L connected at the cell output the power will be at maximum when the resistance R_L will have an optimal value R_{Lopt} equal to the ratio between the voltage V_{mpp} and the current I_{mpp}, Figure 4. Thus, the theoretical Maximum Power generated by the PV cell will be equal to the product between the V_{oc} and I_{sc}.

In these conditions, the fill factor (FF) is defined by

$$\mathrm{FF} = \frac{P_{\max,e}}{I_{sc} V_{oc}} = \frac{I_{mpp} V_{mpp}}{I_{sc} V_{oc}}. \tag{14}$$

The efficiency is calculated as the ratio between the power in MPP (for a specific temperature) and the power of the solar irradiation:

$$\eta = \frac{P_{mpp}}{A_{cell} G}. \tag{15}$$

3. The Effect of the Series and Parallel Resistances on the PV Cell Performances

The series and parallel resistances (R_s and R_p) have an important influence on the fill factor FF decreasing. Its value will decrease with R_s increasing and R_p decreasing. It is noteworthy that the series resistance R_s depends mainly on the internal resistances of the semiconductor devices, on the contact resistances, and on the electrical wires resistances and it has to be as low as possible. In the same time, the parallel resistance R_p depends on the metallic bridges between the edges of the junction, on the material defects (where losses' currents can appear, which can short-circuit the *pn* junction). Usually, its value is high, from thousands to tenth of thousands of ohms.

The relation between R_s and R_p can be estimated starting from the equality $P_{\max,m} = P_{\max,e}$, resulting in the relation for the resistance R_p [5, 10]:

$$P_{\mathrm{mac},m} = V_{\mathrm{mpp}} \left\{ I_{\mathrm{pv}} - I_0 \left[\exp\left(\frac{q}{kT} \frac{V_{\mathrm{mpp}} + R_s I_{\mathrm{mpp}}}{a N_s} \right) - 1 \right] - \frac{V_{\mathrm{mpp}} + R_s I_{\mathrm{mpp}}}{R_p} \right\} = P_{\mathrm{max},e},$$
$$R_p = \frac{V_{\mathrm{mpp}} + I_{\mathrm{mpp}} R_s}{\left\{ I_{\mathrm{pv}} V_{\mathrm{mpp}} - I_0 V_{\mathrm{mpp}} \exp\left[(q/kT) \left(\left(V_{\mathrm{mpp}} + I_{\mathrm{mpp}} R_s \right) / a N_s \right) \right] + I_0 V_{\mathrm{mpp}} - P_{\mathrm{max},e} \right\}}. \tag{16}$$

This equation is solved by successive iterations until it results in the best solution for the PV device. The solution has to concede with the maximum of the points V_{mpp} and I_{mpp}, on the I-V characteristic (Figure 4). In these conditions, the following with be the results [10]:

$$\mathrm{I}_{\mathrm{pv},n} = \frac{R_p + R_s}{R_p} I_{\mathrm{sc},n}. \tag{17}$$

The initial value for R_s is considered as zero, while the value for R_p is given by [7]

$$R_{p,\min} = \frac{V_{\mathrm{mpp}}}{I_{\mathrm{sc},n} - I_{\mathrm{mpp}}} - \frac{V_{0c,n} - V_{\mathrm{mpp}}}{I_{\mathrm{mpp}}}. \tag{18}$$

4. Numerical Modeling and Simulations of a Real Photovoltaic Module

Using the parameters of the ALTIUS AFP 235 Module (Table 1) and the adjusted parameters at nominal operating conditions (Table 2) simulations were realized in MATLAB-Simulink.

The results of the simulations are presented as I-V, P-V, and P-I characteristics in Figures 5–16 for different solar irradiation, temperatures, series resistances, and parallel resistances.

Figures 5, 6, and 7 present the I-V, P-V, and P-I characteristics for a constant temperature (25°C) and for different solar radiations (from $200\,\mathrm{W/m^2}$ to $1000\,\mathrm{W/m^2}$). From Figure 5, with the increase of the solar radiation the current will increase as a result and from Figure 6 the voltage will increase, which will increase the generated power. Figures 8, 9, and 10 present the I-V, P-V, and P-I characteristics for a constant radiation ($1000\,\mathrm{W/m^2}$) and for different temperatures of the environment (from −20°C to 60°C). It is to observed that, with the increasing of the temperature, the current will have a low increase while the voltage will decrease significantly. In this case the power delivered by the PV module will decrease significantly.

Figures 11, 12, and 13 present the I-V, P-V, and P-I characteristics for a constant value of the parallel resistance $R_p = 260\,\Omega$, for different values for the series resistance R_s ($R_s = 0.3\,\Omega$, $R_s = 0.9\,\Omega$, and $R_s = 1.5\,\Omega$), and for standard testing conditions STC ($1000\,\mathrm{W/m^2}$ and 25°C). It is to observed that, for a high value of the resistances R_s, the results will be a decrease in the current and the voltage and, accordingly, a decrease in the generated power. This influence is better to observe near the Maximum Power Point, where both the Maximum Power and the fill factor FF have low values. In this situation it is necessary to have a series resistance as low as possible, very close to zero value.

Figures 14, 15, and 16 present the I-V, P-V, and P-I characteristics for a constant series resistance $R_s = 0.3\,\Omega$, for different values for the parallel resistance R_p ($R_p = 260\,\Omega$, $R_p = 54\,\Omega$, and $R_p = 20\,\Omega$), and for standard testing conditions STC ($1000\,\mathrm{W/m^2}$ and 25°C). It is to observed that, for a low value of the parallel resistance, the results will be decreasing the value for the fill factor and power. For a better operation of the PV cell, it is necessary to have a parallel resistance as high as possible.

From all the above characteristics we can say that the energetical performances of the ALTIUS Module AFP-235W have optimal values when the series resistance is $R_s = 0.3\,\Omega$ and the parallel resistance is $R_p = 260\,\Omega$, for a solar radiation of $1000\,\mathrm{W/m^2}$ and a temperature of the environment of 25°C.

5. Temperature Influence over the PV Module Performances

The increase in the environment temperature and in the thermal radiation has a negative influence over the energetical performances of the PV system. To study these aspects, a thermal model of the ALTIUS Module AFP-235W using the finite element method was realized. The properties of the materials used on the module are presented in Table 3.

The photovoltaic panel is a capsuled system realized from many successive layers. Thus, it is necessary to have a high thermal conductivity in order to assure good cooling of the PV cells. Considering this construction in layers, the thermal transfer is realized between the layers by conduction, convection, and radiation. Thermal analysis by the finite element method supposes an establishment of the thermal equilibrium for every volume zone dV.

$$P_c = P_t - P_r + P_a. \tag{19}$$

The left term of the equation is the heating power from the current flow, P_c. It is in balance with the heat stored by temporal change of temperature P_t, the power removed from the element by thermal conduction P_r, and the thermal power dissipated to the surrounding area by the surface convection, P_a. For P_c, P_t, P_r, and P_a, the following equations can be written:

Table 1: Parameters of the Altius, AFP 235 solar module at 25°C, 1000 W/m^2 [25].

Name-specifications from data sheet	AFP 235
Maximum Power (Pmax,e)	239.99 Wp
Voltage at Maximum Power (Vmp)	29.6 V
Current at Maximum Power (Imp)	7.94 A
Open circuit voltage (Voc)	36.7 V
Short circuit current (Isc)	8.48 A
Maximum Power temperature coefficient	−0.47%/°C
Open circuit voltage temperature coefficient	−0.32%/°C
Short circuit current temperature coefficient	+0.04%/°C
Operating temperature	−40~+85°C
Nominal operating cell temperature (NOCT)	45 ± 2°C
Number of cells (Nc)	60

Table 2: Adjusted parameters of the Altius AFP 235 at nominal operating conditions.

Name-Specifications from data sheet	AFP 235
Maximum Power (Pmax,m)	239.99 Wp
Voltage at Maximum Power (Vmpp)	29.6 V
Current at Maximum Power (Impp)	7.94 A
Open circuit voltage (Voc)	36.7 V
Short circuit current (Isc)	8.48 A
Nominal saturation current ($I_{0,n}$)	3.65412e − 010 A
Photovoltaic current (I_{pv})	8.490576 A
Diode ideality factor (a)	1.3
Series resistance (Rs)	0.318 Ω
Parallel resistance (Rp)	259.398 Ω

$$\begin{aligned} P_c &= \iiint \rho j^2 dV, \\ P_t &= \iiint \gamma c \frac{\partial \theta}{\partial t} dV, \\ P_r &= \iiint \operatorname{div}(\lambda \cdot \operatorname{grad} \theta)\, dV, \\ P_a &= \iiint k_t \frac{l}{S} (\theta - \theta_a)\, dV. \end{aligned} \tag{20}$$

Thus,

$$\begin{aligned} \iiint \rho j^2 dV = {} & \iiint \gamma c \frac{\partial \theta}{\partial t} dV - \iiint \operatorname{div}(\lambda \cdot \operatorname{grad} \theta)\, dV \\ & + \iiint k_t \frac{l}{S} (\theta - \theta_a)\, dV. \end{aligned} \tag{21}$$

The material density, specific heat, and thermal conductivity do not have an important temperature variation; thus they can be regarded as constants. On the other hand, the electrical resistivity has a significant temperature variation and can be estimated through a parabolic variation or a linear one. The experimental tests concluded that the difference between these two types of variation is not so important. For the electrical resistivity a linear variation with the temperature has been considered [32]:

$$\rho = \rho_0 \left[1 + \alpha (\theta - \theta_a)\right] \tag{22}$$

with the notation:

$$\vartheta = \theta - \theta_a. \tag{23}$$

Figure 17 shows the result of the thermal simulation for the ALTIUS Module AFP-235W for a nominal load of 235 W considered with a uniform distribution over the surface of the photovoltaic panel.

A temperature variation on the surface of the PV module is observed starting from a low temperature of 40.15°C to a high value of 52.07°C on the top of the surface of the PV module. This is explained because of variable thermal convection coefficient. This coefficient includes the circulation of the air flow from the lower side of the panel to the top. It was considered only natural to cool of the PV module and for the temperature of the environment to be 25°C.

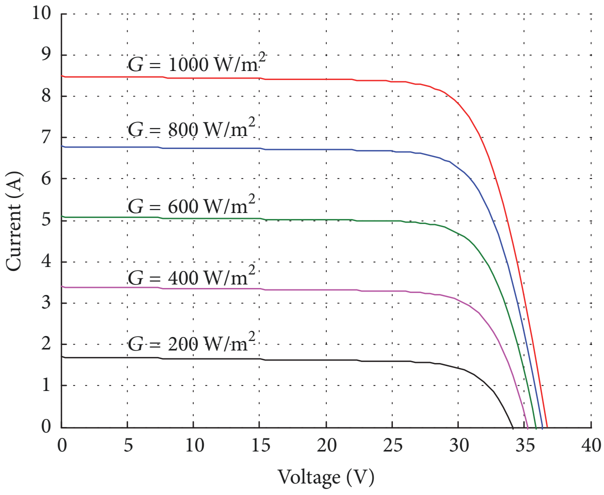

Figure 5: I-V curves for different solar irradiation.

6. Experimental Data for the PV Module

For the experimental analysis the photovoltaic panel ALTIUS Module AFP-235W was considered, oriented to the South and with an inclination of 45°. The experimental tests were realized on May 26, 2016 between 7.00 a.m. and 8 p.m. The solar irradiation was measured using a Solar Survey100/200R instrument, which is in compliance with the IEC-62446 international standard on PV systems. It measures the solar radiation to a maximum of 1500 W/m^2, with a resolution of 1 W/m^2. The temperature was measured with Extech 42545 IR thermometer (range: 50⋯1000°C, resolution: 0.1°C). A digital multimeter Fluke 115 was used to measure the voltage and current (resolution of 1 mV and 1 mA). Figure 18 shows the evolution of the temperature of the environment, the

Table 3: Properties of the materials used in AFP 235 module.

	Material	Thickness [mm]	Thermal conductivity, [W/mK]	Density [kg/m^3]	Specific heat [J/kgK]
1	Glass window	3.2	1.7	3000	780
2	EVA film	1	0.235	960	3135
3	PV cell	0.22	148	2330	710
4	White Polyester	1	0.25	1300	1350

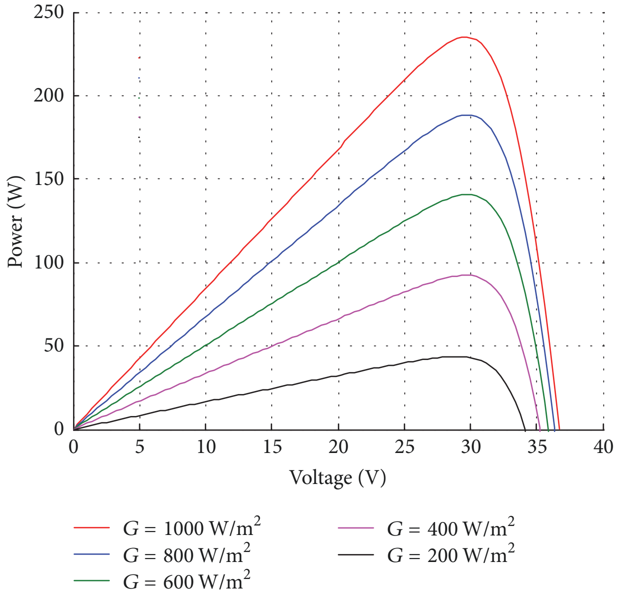

Figure 6: P-V curves for different solar irradiation.

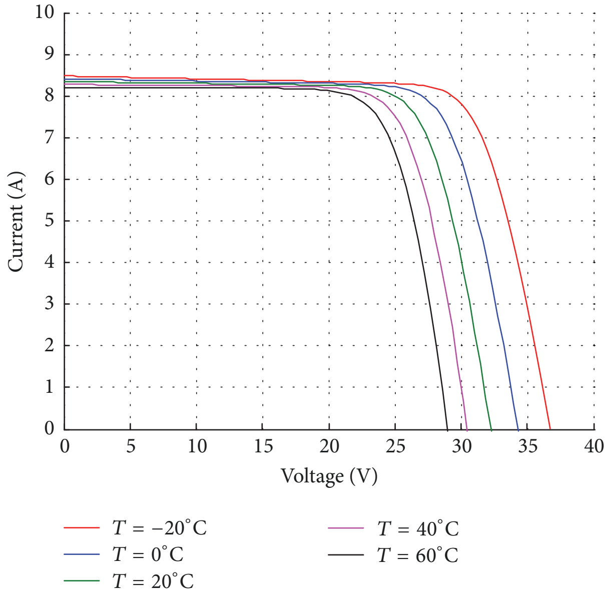

Figure 8: I-V curves for different cell temperatures.

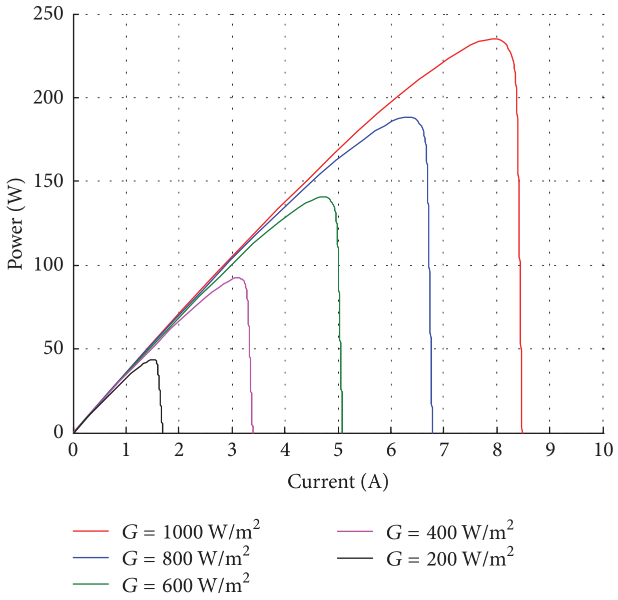

Figure 7: P-I curves for different solar irradiation.

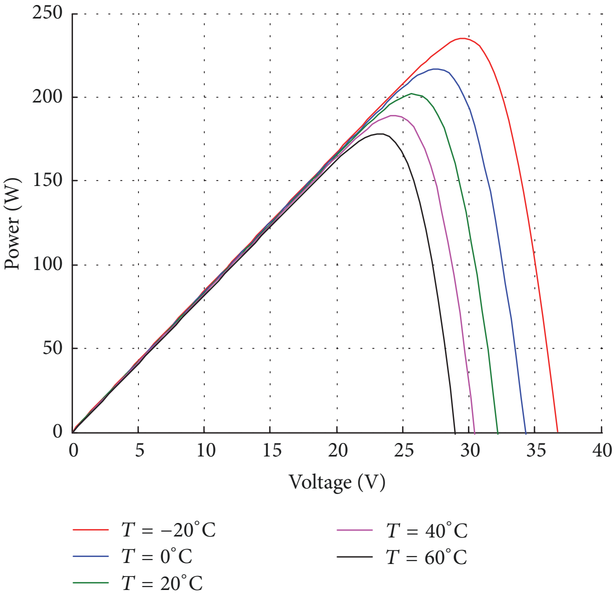

Figure 9: P-V curves for different cell temperatures.

temperature on the surface of the photovoltaic module, and the solar irradiation variation along the day. As the solar irradiation increases and is absorbed at the PV module surface, its temperature is increasing due to the photons absorption. At the maximum temperature of the environment of 28.3°C and a solar irradiation of 672 W/m^2, the temperature of the module surface reaches the value of 41.1°C.

In Figures 19, 20, and 21 the simulated and experimental I-V, P-V, and, respectively, P-I characteristics for the module PFV ALTIUS 235W for a medium temperature of 25°C and a

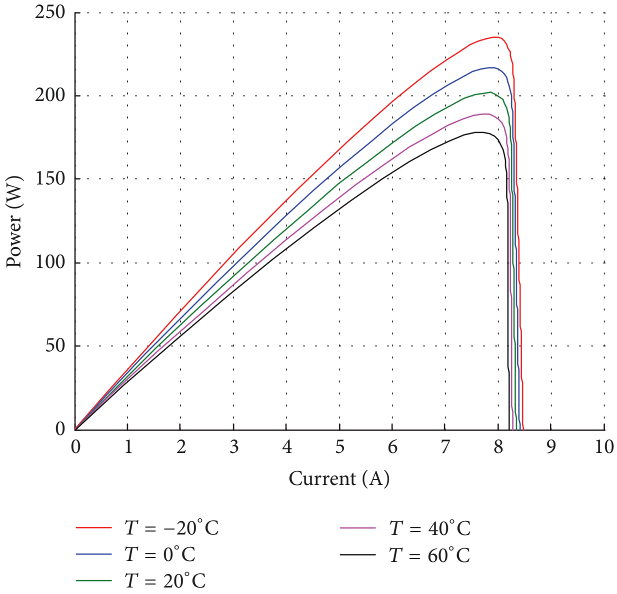

FIGURE 10: *P-I* curves for different cell temperatures.

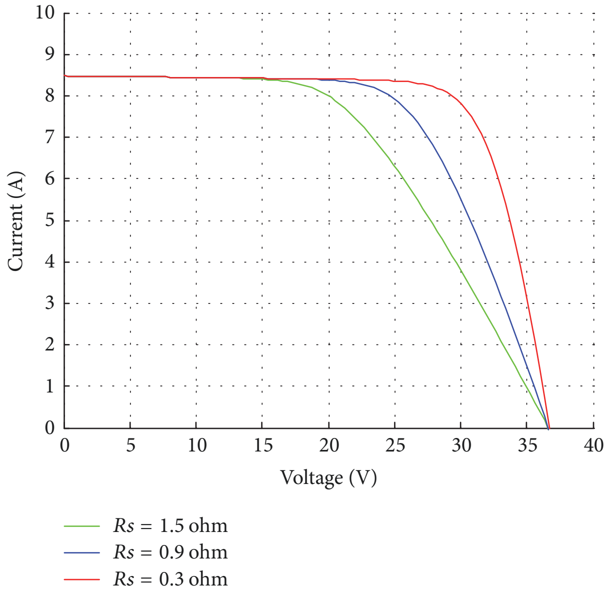

FIGURE 11: *I-V* curves for different R_s.

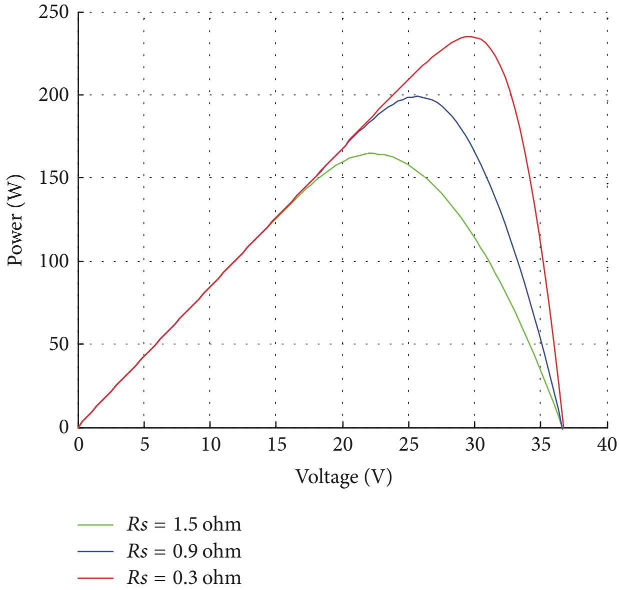

FIGURE 12: *P-V* curves for different R_s.

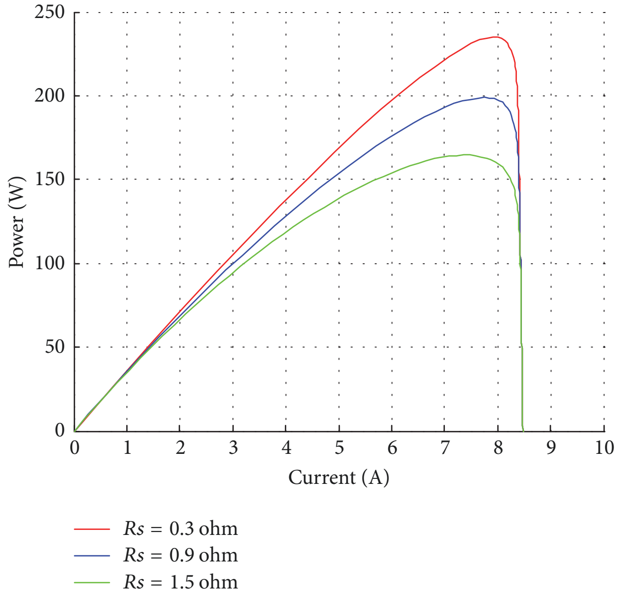

FIGURE 13: *P-I* curves for different R_s.

solar irradiation of 800 W/m^2 are plotted. The value of the nominal short circuit current is of $I_{\mathrm{sc,exp}} = 8.35$ A for the experimental data and of $I_{\mathrm{sc,sim}} = 8.48$ A for the simulation, with an error of 1.55%. The nominal open circuit voltage is of $V_{0\mathrm{c,exp}} = 33.91$ V for the experimental characteristic and $V_{\mathrm{oc,sim}} = 36.33$ V for the simulated one, with an error of −2,6%. In the Maximum Power Point the experimental values for the voltage and current are $V_{\mathrm{mpp,exp}} = 27.79$ V, $I_{\mathrm{mpp,exp}} = 6.628$ A, and a power of $P_{\mathrm{mpp,exp}} = 184.92$ W, while the simulated resulted values are $V_{\mathrm{mpp,sim}} = 25.55$ V, $I_{\mathrm{mpp,sim}} = 7.55$ A, and a power of $P_{\mathrm{mpp,sim}} = 192.9$ W. The error for the power estimation is about 4.3%. In these characteristics there are some differences between the simulated and the experimental data. For example on the point ($I_{\mathrm{sc},n}$), there is a difference of 0.13 A, on the point ($V_{0\mathrm{c},n}$), there is a difference of 2.42 V, and on the MPP point, there is a difference of 2.24 V and 0.982 A (7.98 W). These differences are due to the variation of the real temperature of the environment, of the solar irradiation, and consequently to the surface panel heating. Also the dust deposited on the panel surface and the wind has an important influence over the experimental data and thus on the difference between the simulated data and the experimental ones.

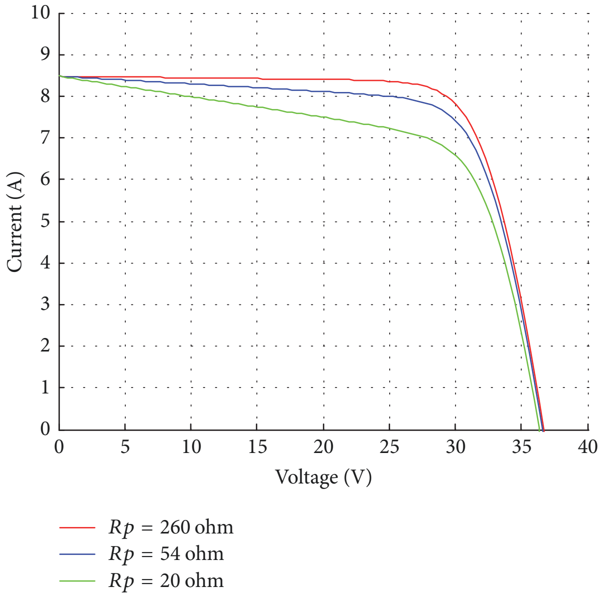

Figure 14: I-V curves for different R_p.

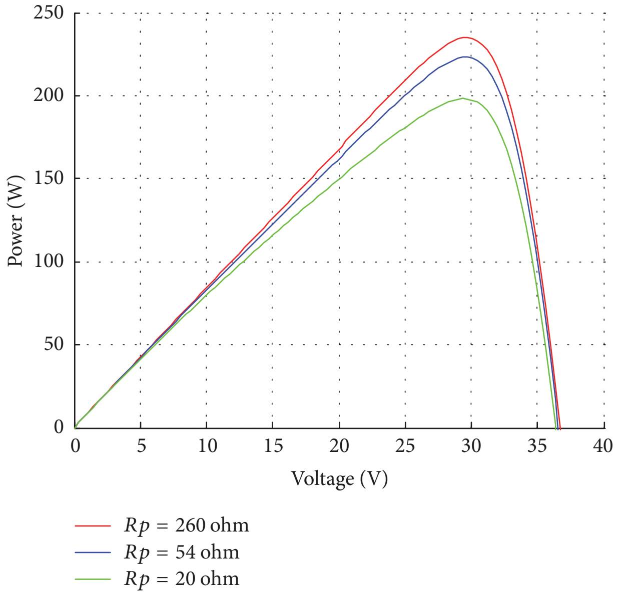

Figure 15: P-V curves for different R_p.

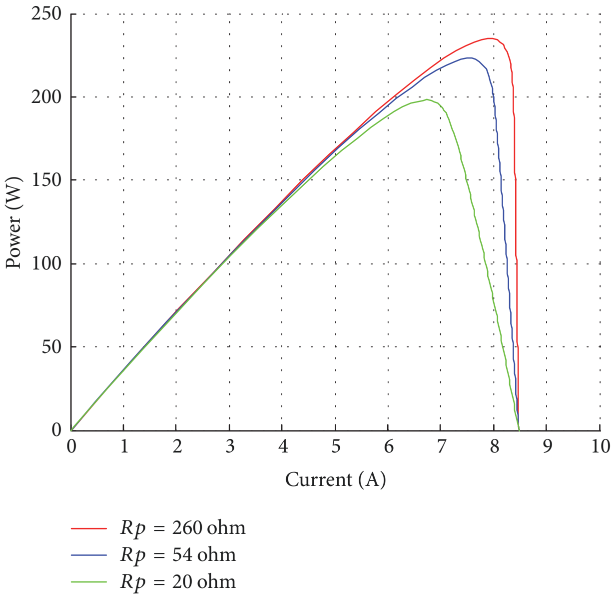

Figure 16: P-I curves for different R_p.

7. Conclusions

In this article a model of the photovoltaic module is developed and the influences of some parameters are analyzed as series and parallel resistances, temperature, and solar irradiation over the PV module output characteristics (I-V, P-V and P-I characteristics). For a real photovoltaic module (ALTIUS Module AFP-235W) there are estimated series and parallel resistances for which the energetical performances of the module have optimal values for a solar radiation of 1000 W/m^2 and a temperature of the environment of 25°C. Temperature influence over the PV module performances is analyzed by using a thermal model of the ALTIUS Module AFP-235W using the finite element method. A temperature variation on the surface of the PV module is estimated as a difference of about 12°C between the bottom and the top surface of the PV module. Experimental data are measured for the photovoltaic ALTIUS Module AFP-235W for an entire daylight. Differences between the simulated and recorded data are due to the variation of the real temperature of the environment, of the solar irradiation, and consequently to the surface panel heating. The dust deposited on the panel surface and the wind has an important influence over the

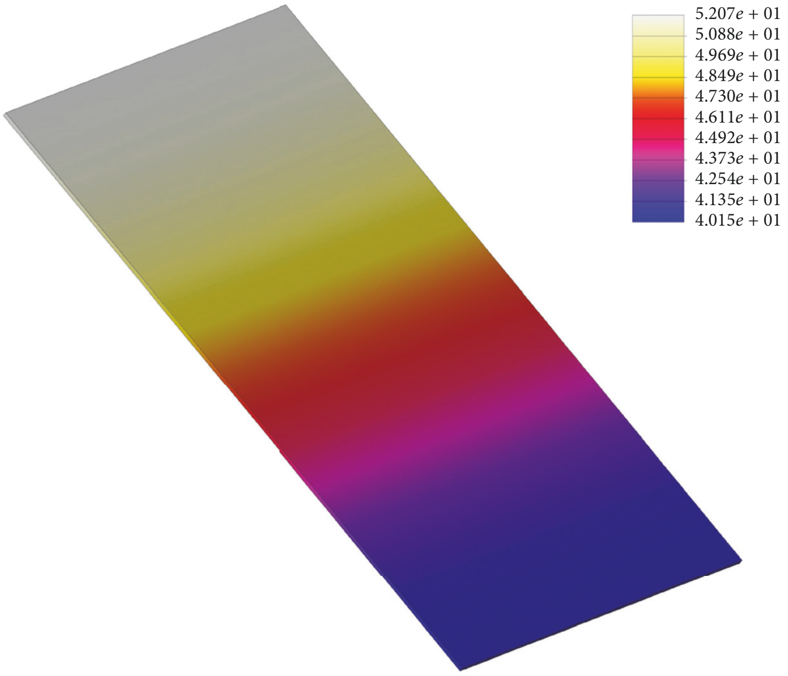

FIGURE 17: The temperature distribution for the PV module ALTIUS 235W.

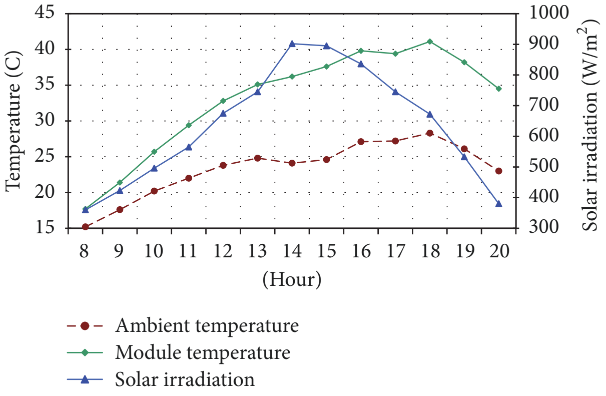

FIGURE 18: The T-t-G experimental characteristics for PFV ALTIUS 235W.

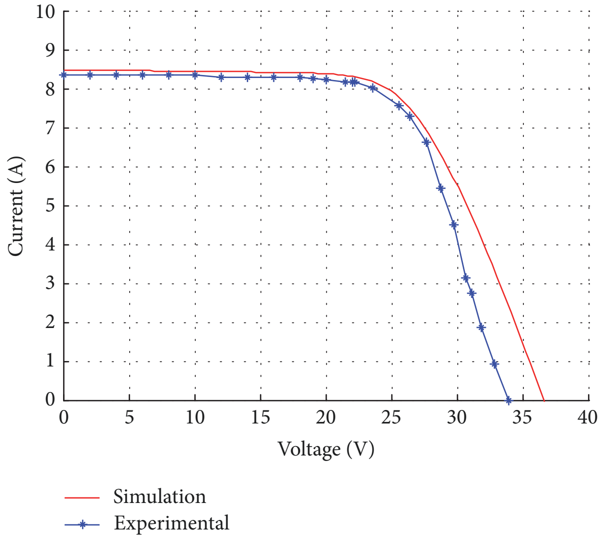

FIGURE 19: The I-V characteristics of PFV ALTIUS 235W.

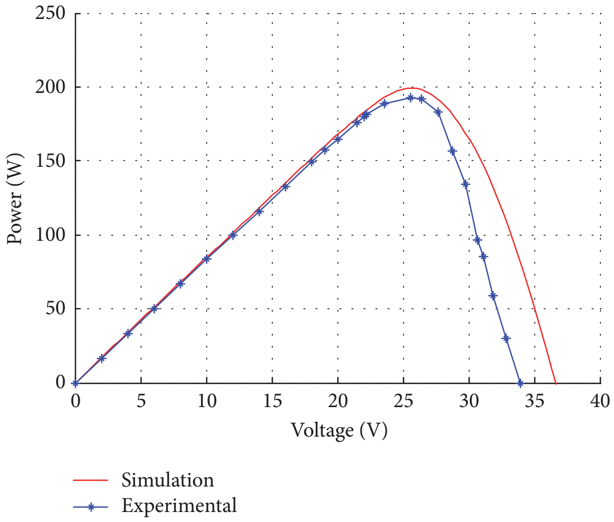

FIGURE 20: The *P-V* characteristics of PFV ALTIUS 235W.

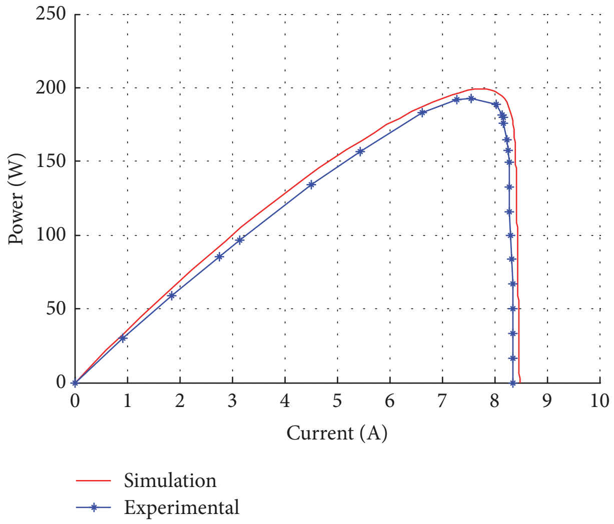

FIGURE 21: The *P-I* characteristics of PFV ALTIUS 235W.

experimental data and thus on the difference between the simulated data and the experimental ones.

Nomenclature

A_{cell}: The surface of the cell
a: The ideality factor of the diode, $1 \le a \le 1.5$
c: Specific heat
G: The incident irradiation
G_n: The nominal irradiation (usually $1000\ \text{W/m}^2$)
I_0: The reverse saturation current of the diode
$I_{0,n}$: The nominal saturation current
I_D: The diode current
I_{mpp}: The current at the MPP point
I_{pv}: The photovoltaic current of the PV cell
$I_{\text{pv},n}$: The photovoltaic current at nominal irradiation and temperature
$I_{\text{sc},n}$: The nominal short circuit current
j: Current density
K_V: The open circuit voltage temperature coefficient of the module
K_I: The short circuit current temperature coefficient of the module
k: The Boltzmann constant
k_t: Total transfer coefficient
l: Perimeter length of the external surface
MPP: Maximum Power Point
N_p: The number of the cells connected in parallel
N_s: The number of the cells connected in series
P_a: The thermal power dissipated to the environment area by the surface convection
P_c: The heating power from the current flow
$P_{\max,e}$: The maximum experimental power
$P_{\max,m}$: The maximum calculated peak output power
P_r: The power removed from the element by thermal conduction
P_t: The heat stored by temporal change of temperature
q: The electron charge
R_p: The equivalent parallel resistance of the module
R_s: The equivalent series resistance of the module
S: Surface convection
T: The ambient temperature
T_m: The nominal temperature (usually 25°C)
V: The open circuit voltage
$V_{0c,n}$: The nominal open circuit voltage of the module
V_T: The thermal voltage of the module
V_{mpp}: The voltage at the MPP
α: Coefficient of electrical resistivity variation with temperature
γ: Material density
λ: Thermal conductivity
ρ: Electrical resistivity
ρ_0: Electrical resistivity at the θ_a temperature
θ: Temperature
θ_0: The initial temperature of the photovoltaic module
θ_a: The temperature of the environment
$\vartheta = \theta - \theta_a$: As notation.

Conflicts of Interest

The authors declare that they have no conflicts of interest.

References

[1] R. Kumar and R. Muralidharan, "Mathematical modeling, simulation and validation of photovoltaic cells," *International Journal of Research in Engineering and Technology*, vol. 3, no. 10, pp. 170–174, 2014.

[2] T. Ahmad, S. Sobhan, and M. F. Nayan, "Comparative analysis between single diode and double diode model of PV cell: concentrate different parameters effect on its efficiency," *Journal of Power and Energy Engineering*, vol. 04, no. 03, pp. 31–46, 2016.

[3] H.-L. Tsai, C.-S. Tu, and Y.-J. Su, "Development of generalized photovoltaic model using MATLAB/Simulink," in *Proceedings of the World Congress on Engineering and Computer Science*, pp. 1–6, San Francisco, Calif, USA, 2008.

[4] B. Habbati, Y. Ramdani, and F. Moulay, "A detailed modeling of photovoltaic module using MATLAB," *NRIAG Journal of Astronomy and Geophysics*, vol. 3, pp. 53–61, 2014.

[5] M. G. Villalva, J. R. Gazoli, and E. R. Filho, "Modeling and circuit-based simulation of photovoltaic arrays," *Brazilian Journal of Power Electronics*, vol. 14, no. 1, pp. 35–45, 2009.

[6] Y. T. Tan, D. S. Kirschen, and N. Jenkins, "A model of PV generation suitable for stability analysis," *IEEE Transactions on Energy Conversion*, vol. 19, no. 4, pp. 748–755, 2004.

[7] A. Dev and B. Jeyaprabha, "Modeling and simulation of photovoltaic module in MATLAB," in *Proceedings of the International Conference on Applied Mathematics and Theoretical Computer Science*, pp. 268–273, 2013.

[8] A. M. Haque, S. Sharma, and D. Nagal, "Simulation of photovoltaic array using MATLAB/Simulink: analysis, comparison & results," *International Journal of Advanced Computer Technology*, vol. 3, no. 2, pp. 12–21, 2016.

[9] J. Park, H. Kim, Y. Cho, and C. Shin, "Simple modeling and simulation of photovoltaic panels using Matlab/Simulink," *Advanced Science and Technology Letters*, vol. 73, pp. 147–155, 2014.

[10] S. Sumathi, A. L. Kumar, and P. Surekha, *Solar PV and Wind Energy Conversion Systems. An Introduction to Theory, Modeling with MATLAB/Simulink, and the Role of Soft Computing Techniques*, Green Energy and Technology, Springer, New York, NY, USA, 2015.

[11] N. D. Benavides and P. L. Chapman, "Modeling the effect of voltage ripple on the power output of photovoltaic modules," *IEEE Transactions on Industrial Electronics*, vol. 55, no. 7, pp. 2638–2643, 2008.

[12] A. Kajihara and T. Harakawa, "Model of photovoltaic cell circuits under partial shading," in *Proceedings of the IEEE International Conference on Industrial Technology (ICIT '05)*, pp. 866–870, Hong Kong, China, December 2005.

[13] A. N. Celik and N. Acikgoz, "Modelling and experimental verification of the operating current of mono-crystalline photovoltaic modules using four- and five-parameter models," *Applied Energy*, vol. 84, no. 1, pp. 1–15, 2007.

[14] L. Cristaldi, M. Faifer, M. Rossi, and S. Toscani, "An improved model-based maximum power point tracker for photovoltaic panels," *IEEE Transactions on Instrumentation and Measurement*, vol. 63, no. 1, pp. 63–71, 2014.

[15] M. Veerachary, "PSIM circuit-oriented simulator model for the nonlinear photovoltaic sources," *IEEE Transactions on Aerospace and Electronic Systems*, vol. 42, no. 2, pp. 735–740, 2006.

[16] I. H. Altas and A. M. Sharaf, "A photovoltaic array simulation model for matlab-simulink GUI environment," in *Proceedings of the International Conference on Clean Electrical Power (ICCEP '07)*, pp. 341–345, Capri, Italy, May 2007.

[17] E. Matagne, R. Chenni, and R. El Bachtm, "A photovoltaic cell model based on nominal data only," in *Proceedings of the International Conference on Power Engineering, Energy and Electrical Drives (POWERENG '07)*, pp. 562–565, Setubal, Portugal, April 2007.

[18] Y. Lee and A. A. O. Tay, "Finite element thermal analysis of a solar photovoltaic module," *Energy Procedia*, vol. 15, pp. 413–420, 2012.

[19] W. Z. Leow, Y. M. Irwan, M. Irwanto, M. Isa, A. R. Amelia, and I. Safwati, "Temperature distribution of three-dimensional photovoltaic panel by using finite element simulation," *International Journal on Advanced Science, Engineering and Information Technology*, vol. 6, no. 5, pp. 607–612, 2016.

[20] N. Boulfaf and J. Chaoufi, "Identification of thermal parameters of a solar photovoltaic panel in three-dimensional using finite element approach," *International Journal of Renewable Energy Research*, vol. 7, no. 2, pp. 578–584, 2017.

[21] F. Montero-Chacón, S. Zaghi, R. Rossi et al., "Multiscale thermo-mechanical analysis of multi-layered coatings in solar thermal applications," *Finite Elements in Analysis and Design*, vol. 127, pp. 31–43, 2017.

[22] A. Massi Pavan, S. Vergura, A. Mellit, and V. Lughi, "Explicit empirical model for photovoltaic devices. Experimental validation," *Solar Energy*, vol. 155, pp. 647–653, 2017.

[23] F. Sarhaddi, S. Farahat, H. Ajam, A. Behzadmehr, and M. Mahdavi Adeli, "An improved thermal and electrical model for a solar photovoltaic thermal (PV/T) air collector," *Applied Energy*, vol. 87, no. 7, pp. 2328–2339, 2010.

[24] J. Yazdanpanahi, F. Sarhaddi, and M. Mahdavi Adeli, "Experimental investigation of exergy efficiency of a solar photovoltaic thermal (PVT) water collector based on exergy losses," *Solar Energy*, vol. 118, pp. 197–208, 2015.

[25] Altius module high performance solar modules, AFP 60-250 Series/235-250W.

[26] D. Sera, R. Teodorescu, and P. Rodriguez, "PV panel model based on datasheet values," in *Proceedings of the IEEE International Symposium on Industrial Electronics (ISIE '07)*, pp. 2392–2396, Vigo, Spain, June 2007.

[27] A. Driesse, S. Harrison, and P. Jain, "Evaluating the effectiveness of maximum power point tracking methods in photovoltaic power systems using array performance models," in *Proceedings of the PESC 07 - IEEE 38th Annual Power Electronics Specialists Conference*, pp. 145–151, Orlando, Fla, USA, June 2007.

[28] R. A. Messenger and J. Ventre, *Photovoltaic Systems Engineering*, CRC Press, Boca Raton, Fla, USA, 2004.

[29] J. Crispim, M. Carreira, and C. Rui, "Validation of photovoltaic electrical models against manufacturers data and experimental results," in *Proceedings of the International Conference on Power Engineering, Energy and Electrical Drives, POWERENG 2007*, pp. 556–561, Setubal, Portugal, April 2007.

[30] N. M. Abd Alrahim Shannan, N. Z. Yahaya, and B. Singh, "Single-diode model and two-diode model of PV modules: a comparison," in *Proceedings of the 2013 IEEE International Conference on Control System, Computing and Engineering, ICCSCE 2013*, pp. 210–214, Mindeb, Malaysia, December 2013.

[31] V. Sangsawang and S. Chaitusaney, “Modeling of photovoltaic module from commercial specification in datasheet,” in *Proceedings of the 9th International Conference on Electrical Engineering/Electronics, Computer, Telecommunications and Information Technology, ECTI-CON 2012*, Phetchaburi, Thailand, May 2012.

[32] A. T. Plesca, “Thermal analysis of the current path from circuit breakers using finite element method,” *International Journal of Electrical, Computer, Energetic, Electronic and Communication Engineering*, vol. 6, no. 12, pp. 1479–1487, 2012.

THERMAL MODELING OF A LINEAR INDUCTION MOTOR USED TO DRIVE A POWER SUPPLY SYSTEM FOR AN ELECTRIC LOCOMOTIVE

by

Costica NITUCA[a]***, Gabriel CHIRIAC***[a*]***, Dumitru CUCIUREANU***[b]***,***
Catalin DUMITRESCU[a]***, Guoqiang ZHANG***[c]***, Dong HAN***[c]***, and Adrian PLESCA***[a]

[a]Faculty of Electrical Engineering, Gheorghe Asachi Technical University of Iasi, Iasi, Romania
[b]Q SRL, Iasi, Romania
[c]Institute of Electrical Engineering, Chinese Academy of Sciences, Beijing, China

Original scientific paper
https://doi.org/10.2298/TSCI180420190N

In this article a thermal modeling is developed for a double sided linear induction motor which is used to drive a power supply system for an electric locomotive. Two cases were considered for the linear motor, with full plate armature and with sectioned plate armature. The thermal model has been obtained with Pro/Engineering software package and the mesh of the 3-D thermal model has been done using tetrahedron solid elements types. Experimental validation of the model has been realized too. Errors between the simulations and the experimental data (between 1% and 4%) show that the proposed model can be used for accurate precision of the heat distribution on the linear motor.

Key words: linear induction motor, thermal regime, modeling, simulations, experimental validation

Introduction

Linear motors can be used as efficient tool to achieve the high speed and precision for linear motion applications or for different systems where they can replace the rotary electric machines, hydraulic or pneumatic equipments with linear movement. Linear motors are used in automotive suspension [1], wave-energy conversion [2], electrical transport, elevators in high buildings [3, 4] or sliding door applications [5]. Ultra-precision applications are also a domain utilization for the linear motors [6]. Interaction between electromagnetic and temperature field in a solid ferromagnetic plate is considered in [7] by moving linear high frequency induction heater.

Another possible application of the linear induction motor is to drive the pantograph collecting system on the electric vehicles, like electric locomotives and tramways [8] where the linear motor assures the contact force between the catenary and the pantograph's skate. Thus, a better contact improves the current collection process and reduces the wear of the pantograph and of the contact line and reduces the detachments of the pantograph skate from the wire [9]. In this case the motor operates in an oscillating regime which can generate heat problems and it can affect the thermal deformation of the machine structure. The thermal deformation characteristics can be identified through measuring the thermal error caused from thermal deformation of the linear scale and the machine structure [10]. The thermal regime depends on the supply

---

[*] Corresponding author, e-mail: gchiriac@tuiasi.ro

system characteristics, on the driven kinematics, as well as on the linear motor structure and on its cooling system.

The need for an analysis of the thermal processes can arise when designing a linear motor [11] but also for the supplying system and for the protection of the system [12]. The possibility of reducing the non-linearities of the model for calculating the thermal characteristics of a linear asynchronous machine is considered. The temperature field is calculated in the time domain taking into account the change in the thermal and electromagnetic properties of the material at each time step [13].

Finite element method can be used to analyze the heat transfer into the linear motors [14]. The thermal transfer aspects are criteria in choosing a right linear motor for a specific application considering the heat transfer by conduction, radiation and convection, the heating sources and the duty cycle of the motor [15]. Is considered the thermal characteristics of a linear induction machine under intensive track operation. Thermal characteristics are calculated using the method of detailed equivalent heat circuit. A brief analysis of the possibility of operation in different operating modes is given [16].

It should be noted that for a double-sided linear motor with yoke and multi-segmented array, the coating on the coil cannot withstand the temperature more than 120 °C [17].

The surface area joining the linear motor coil to the application carriage is large so it will be inaccurate to assume a constant temperature over the entire surface. The temperature of the surface is different for different location and time [18]. A 3-D finite difference method is adopted to model the motor coil to calculate the amount of the heat transferred to the carriage. The theoretical results are verified with experiments. It is demonstrated that the proposed model is capable to predict accurately the temperature variation at the interface between the motor coil and carriage, and therefore the heat flux can be obtained for the full range of the motor operating power [19].

Starting from the previous considerations this paper presents thermal analysis (modeling and experimental) of a linear induction motor. The test bench uses a linear induction motor to drive an asymmetrical pantograph with the aim to supply an electric locomotive. The contact force of the pantograph is assured by the linear motor and the system has to operate for a long time, even hours, (the electric locomotives have a long operating time) and thus it becomes very important to study the thermal regime of the motor. The objectives of this work are:

- to develop a thermal model for the linear induction motor,
- two cases are considered for the thermal model and simulations; with full plate armature and with sectioned plate armature,
- simulations are realized using the Pro/Engineering software package,
- experimental tests are also realized for the both cases in order to validate the thermal model, and
- comparison of the simulated and experimental data are considered to estimate if the proposed model can be used for accurate predictions of the temperature distribution into the motor.

The linear induction motor

The linear induction motor is used on a test bench which simulates the power supply for an electric locomotive, fig. 1. The linear induction motor – 1 is used to drive an asymmetrical pantograph – 3 necessary for the power collecting from a contact wire – 4. The contact wire is realized as a rotating copper disc. The pantograph has to act with a contact force, F_c, on the contact line. The contact force is given by a resort (the main force F_R) and by the linear induction motor (for a supplementary force F_{LIM}). Thus, the motor offers the possibility to control the contact force according to the power collecting necessity. The motor operates in oscillating regime and because of this special regime the thermal aspects become important.

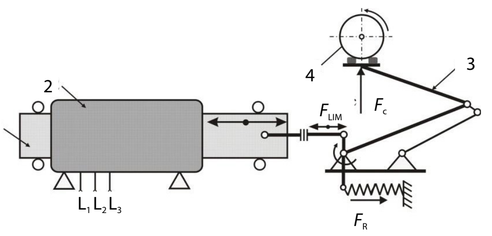

Figure 1. Test bench; *1 – linear induction motor, 2 – inductor, 3 – asymmetrical pantograph, 4 – copper rotating disk*

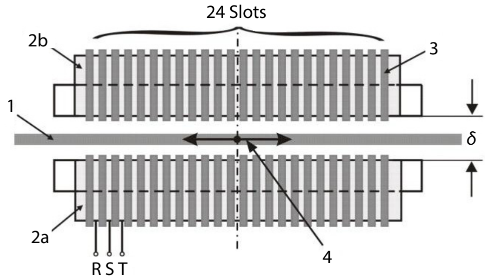

Figure 2. Bilateral linear induction motor; *1 – plate mobile armature (2a), (2b) inductors of the double sided linear motor, 3 – coils, 4 – oscillating movement of the plate mobile armature*

The linear motor is a three-phase asynchronous machine with a plate mobile armature – 1 from copper, fig. 2. The motor has a bilateral structure, having two inductors, 2a and 2b, (a double sided linear motor) with the ring windings in 24 slots, yielding the coils – 3. The mobile plate armature is vertically placed and it has an oscillating movement – 4 on a distance of about 60-90 mm and an air gap $\delta = 4$ mm. It is important to notice that some special effects of the linear motors (the edge effects, the transversal effects) are neglected, in order to simplify the thermal model.

The main restrictive effect for the motor power is the heat transfer and thus, the thermal behavior must be taken into account. For the small oscillating movements (less than 60-90 mm), the armature plate will be usually in the same relative position with respect to the inductors, which will give a higher heating and consequently an important influence over the machine's parameters and operating. The motor is not a homogeneous body but it is a combination of different materials (cooper, steel, iron, *etc.*), and the heating analysis could be complex.

The heating differential equation for the linear motor

The linear motors are different to study from the thermal point of view in comparison with the classical rotary motors due to their specific construction and the electromagnetic aspects. Rotary induction motors are largely used and there is a high interest in their analysis, including the thermal aspects [20, 21].

Overheating can cause undesirable motor failures with high cost due to the interruption and damages on equipments. Inside the motor the stator insulation may degrade because of the overheating and, even if the temperature does not exceed the motor insulation class limit, it will decrease the lifetime of the insulation. Venkatamaran *et al.* [22] states that an operating temperature increase of 10 °C in excess of the thermal limit cuts the life of stator insulation by half. The plate armature can be deformed due to the overheating and this deformation could lead to undesirable contacts between the plate and the inductors.

An analysis can be made, for a first estimation, in analogy with the rotary machines starting from the thermal equation:

$$Q\mathrm{d}t = A\theta\mathrm{d}t + C\mathrm{d}\theta \tag{1}$$

The heat, Q, released into the motor in a time, dt, is equal to the heat released by the machine for a difference of temperature, θ, between the machine and the, $A\theta$dt, plus the heat absorbed by the machine ($C\mathrm{d}\theta$) to increase its temperature by θ degrees. This equation can be rewritten:

$$\mathrm{d}t = \frac{C\mathrm{d}\theta}{Q - A\theta} \tag{2}$$

where C is the thermal capacity of the machine, A – the heat transfer capacity of the machine.

The integration of the eq. (2) will give the variation relationship of the machine heating:

$$\theta = \frac{Q}{A}\left[1 - \exp\left(\frac{-t}{\frac{C}{A}}\right)\right] + \theta_0 \exp\left(\frac{-t}{\frac{C}{A}}\right) \tag{3}$$

where θ_0 is the initial temperature of the machine. The ratio C/A is a constant for a given machine and represents the time constant of the machine heating or the temperature delay (thermal inertia) of the machine:

$$T_\theta = \frac{C}{A} \tag{4}$$

For the actual linear motor this constant was estimated [23, 24] for two different plate armatures, a full plate armature and a sectioned plate armature. Thus it was calculated the maximum temperature into the motor and compared with the measurements, resulting the values of 92 °C and respective 96 °C. These differences are due to the different plate armatures. The sectioned plate armature has a low surface area to eliminate the heat, resulting in higher temperatures on the motor.

A thermal study could also start from the power balance equation for each volume element $\mathrm{d}V$:

$$P_C = P_T - P_R + P_A \tag{5}$$

The left term of the eq. (5) is the heating power from the current flow, P_C.

On the right-hand side of the eq. (5) there are three powers: P_T – as the heat stored by temporal change of temperature, P_R – as the power removed from the element by thermal conduction, and P_A – as the thermal power dissipated to the environment area by the surface area. The above equation can be expressed as follow, considering the four powers:

$$\iiint \rho j^2 \mathrm{d}V = \iiint \gamma c \frac{\partial\theta}{\partial t}\mathrm{d}V - \iiint \mathrm{div}\left(\lambda \mathrm{grad}\theta\right)\mathrm{d}V + \iiint k\frac{l}{S}\left(\theta - \theta_a\right)\mathrm{d}V \tag{6}$$

The material density, specific heat and thermal conductivity do not have an important temperature variation and, into a simplified model, they can be considered as constants. The electrical resistivity has an important temperature variation and it can be estimated through a linear variation:

$$\rho = \rho_0\left[1 + \alpha\right]\left(\theta - \theta_0\right) \tag{7}$$

It results a non-linear and non-homogeneous equation which can be resolved by numerical methods:

$$\iiint \rho_0\left(1 + \alpha\vartheta\right)\frac{i^2}{S^2}\mathrm{d}V = \iiint \gamma c \frac{\partial\vartheta}{\partial t}\mathrm{d}V - \iiint \mathrm{div}\left(\lambda \mathrm{grad}\vartheta\right)\mathrm{d}V + \iiint k\frac{l}{S}\vartheta \mathrm{d}V \tag{8}$$

Using the finite element method it can be estimated the thermal variation within the linear induction motor by 3-D simulation.

Thermal modeling of the double sided linear induction motor

To study the thermal aspects of the considered linear induction motor it was developed a thermal model and simulations were also realized. It was developed a geometrical model of the linear induction motor with the plate armature of copper and the two inductors symmetrically placed over the plate armature. The setting parameters used for the thermal simulations are presented in tab 1.

Table 1. Setting parameters used for the thermal simulation

	Mobile plate armature (Cu)	Yokes (Fe)	Insulation
Thermal conductivity [Wm^{-1}K^{-1}]	385	420.27	1.25
Specific heat [Jkg^{-1}K^{-1}]	385	52.028	137
Material density [kgm^{-3}]	8900	7190	1400

The room temperature was considered as 21°C. The simulations were realized for two cases: first for a linear induction motor with full plate armature, and second for a linear induction motor with sectioned plate armature. The thermal model has been obtained using the software package Pro/Engineering and all the thermal simulations have been performed with the Pro/Mechanica software package. The heat load has been applied uniformly in all the volume of every copper winding. The convection conditions have been used as boundary conditions. Also, a bulk temperature of 21 ºC has been considered.

The mesh of this 3-D thermal model has been done using tetrahedron solids element types with the following allowable angle limits (degrees): maximum edge 175, minimum edge 5, maximum face 175, minimum face 5. The maximum aspect ratio was 30 and the maximum edge turn (degrees) 95. Also, the geometry tolerance had the following values: minimum edge length 0.0001, minimum surface dimension 0.0001, minimum cusp angle 0.86, merge tolerance 0.0001. The single pass adaptive convergence method to solve the thermal steady-state simulation has been used.

Figure 3. presents the result simulation of thermal distribution into the linear induction motor. The maximum temperature is in the middle of the two inductors and it is about 92.4 °C, very close to the experimental measurements. The temperatures are decreasing from about 90 °C in the middle on the copper windings, to about 60 °C into the lateral windings. On the armature plate the distribution of the temperatures is from about 85 °C in the middle to about 30 °C on the edges.

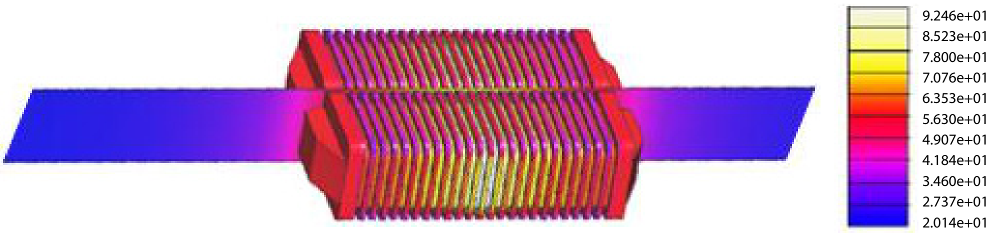

Figure 3. Distribution of the temperature over the linear induction motor

The thermal load was not distributed uniformly in all the volume of every copper winding. On the lateral areas the temperature is lower because the windings are in contact with the lateral pieces of aluminum, which have a coefficient of convection of 19.75 W/mK. For the inductor the coefficient is 14.2 W/mK and for the isolation it was considered 12.5 W/mK.

A thermal model of the linear induction motor with sectioned plate armature was also made in order to estimate the heating areas into the motor, fig. 4. The plate armature is vertical cutting-up sectioned and it was tested in order to reduce the eddy currents into the plate armature, which are not useful for the force developed by the linear motor. It is to mention that the plate armature is considered as acting with a constant force. The thermal distribution over the linear motor is presented in fig. 4, with an ambient temperature of 20 °C. The temperature distribution shows a maximum value in the middle of the inductors, with about 96 °C, close to the experimental maximum data of about 90 °C.

At the edges of the inductors the temperatures decrease at about 56 °C, where the heat can be release easily to the ambient medium. Into the plate armature, the temperature varies from about 96 °C inside the inductors space, to less than 30 °C outside the inductors.

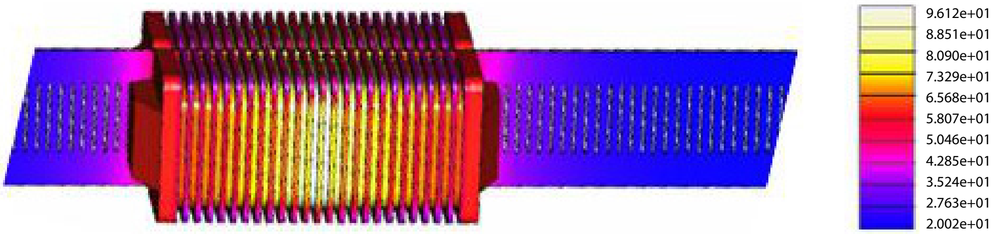

Figure 4. Distribution of the temperature over the linear induction motor with a sectioned plate armature

Experimental validation of the thermal model of the linear induction motor

The estimation of the temperature increase of the windings and of the other parts of the motor is made with a locked armature. The inductor is supplied at rated voltage and rated frequency from a three-phase symmetrical supply system (by a three-phase autotransformer). The measurements are on the inductor denoted (2b) because it heats up more intensely then the inductor (2a) (about 2-3%) due to the constructive imperfection of the motor. The estimation of the temperature increase of the windings and of the other parts of the motor is made with a locked armature and for a force of 70 N. There is no cooling system considered. The temperatures have been measured using an infrared camera type FLIR E40.

The temperature measurement points on the linear motor are presented in fig. 5. For the coils the temperature is measured for the slots θ_1, θ_3, θ_6, θ_{10}, θ_{12}, θ_{13}, θ_{15}, θ_{19}, θ_{22}, and θ_{24} (ten points of measurements). All of these will give a large view over the variation of the temperature in the motor.

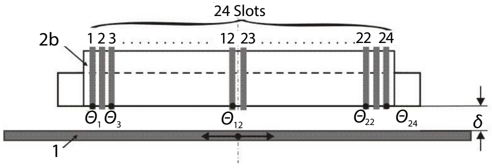

Figure 5. Measured points of the temperature on the inductor

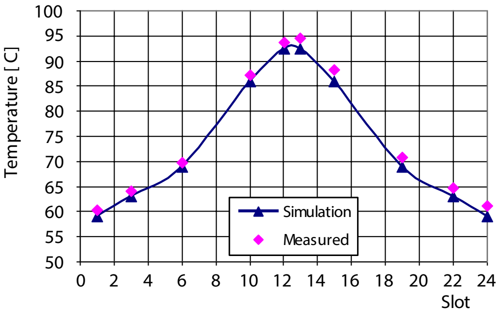

Figure 6. Simulated and measured temperatures distribution over the inductor

Figure 6 shows the simulated and measured temperatures for the motor with full plate armature. It is to observe from the experimental data, tab. 2 and fig. 6, that the maximum temperature is measured in the middle of the inductor area, for the slot 13, a little higher than for the slot 12 because of the constructive imperfections of the motor. These temperatures don't exceed the maximum temperature allowance, of 120 °C.

Table 2. Simulated temperatures, measured temperatures, and errors for the motor with the full plate armature

Slot No.	Simulated temperatures [°C]	Measured temperatures [°C]	Error [%]
1	59	60.3	2.16
3	63	64.1	1.72
6	69	69.8	1.15
10	86	87.2	1.38
12	92.4	93.7	1.39
13	92.4	94.6	2.33
15	86	88.2	2.49
19	69	70.9	2.68
22	63	64.7	2.63
24	59	61.1	3.44

Figure 7. shows the simulated and measured temperatures for the motor with sectioned plate armature. The maximum measured temperatures are also on the middle of the inductors, and the values are higher, to about 100°C. In both cases the measured temperatures are higher than the simulated ones, (tabs. 2 and 3).

This could be explaining by neglecting the special effects of the linear motor in order to simplify the thermal model and also by the constructive imperfection of the motor. The errors presented into the tabs. 2 and 3 are still into the acceptable values.

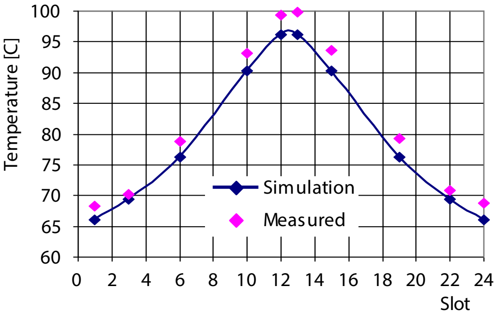

Figure 7. Simulated and measured temperatures, distribution over the inductor with the sectioned plate armature

Table 3. Simulated temperatures, measured temperatures, and errors for the motor with sectioned plate armature

Slot No.	Simulated temperatures [°C]	Measured temperatures [°C]	Error [%]
1	66.1	68.3	3.22
3	69.4	70.2	1.14
6	76.3	78.8	3.17
10	90.2	93.2	3.22
12	96.1	99.4	3.32
13	96.1	99.8	3.71
15	90.2	93.6	3.63
19	76.3	79.3	3.78
22	69.4	70.9	2.12
24	66.1	68.8	3.92

Conclusions

In this article it is studied a thermal model for a linear induction motor used to drive a pantograph from a power supply system of an electric locomotive. The drive system is subject of a patent with the number RO 128199 B1/2018.

- A thermal model of the motor was developed for two cases: with full plate armature and with sectioned plate armature in order to have a thermal image of the linear induction motor and a prediction of thermal distribution.
- The thermal model has been realized with Pro/Engineering software package.
- Experimental tests were also realized for the both cases, the errors between the simulations and experimental data being between about 1% and 4%, which shows that the proposed model can be used for accurate predictions of the temperature and heat distribution of the motor.
- The maximum temperature allowance (of 120 °C), is not exceeded and the motor can operate for a long time corresponding to the electric locomotive operating conditions.

Nomenclature

A	– heat transfer capacity of the machine, [JK^{-1}s^{-1}]
C	– thermal capacity of the machine, [JK^{-1}]
c	– specific heat, [Jkg^{-1}K^{-1}]
i	– electric current, [A]
j	– current density, [Acm^{-2}]
k	– total transfer coefficient
l	– perimeter of the external surface, [m]
P_A	– thermal power dissipated to the environment area by the surface convection, [W]
P_C	– heating power from the current flow, [W]
P_R	– power removed from the element by thermal conduction, [W]
P_T	– heat stored by temporal change of temperature, [W]
Q	– heat released into the motor in a time dt, [J]
S	– surface area, [m^2]
T_θ	– time constant of the machine heating, [s]

Greek symbols

α	– coefficient of electrical resistivity variation with temperature
γ	– material density, [kgm^{-3}]
λ	– thermal conductivity, [Wm^{-1}K^{-1}]
ρ	– electrical resistivity, [Ωm]
ρ_0	– electrical resistivity at the θ_0 temperature, [Ωm]
θ	– temperature, [°C]
θ_0	– initial temperature of the machine [°C]
θ_a	– environment temperature, [°C]
ϑ	– as a notation, $(= \theta - \theta_a)$, [°C]

References

[1] Hyniova, K., *et al*., Experiments on Energy Management in Active Suspension of Vehicles, *Int. J. of Systems Applications*, *Engineering* & *Development*, *6* (2012), 2, pp. 196-203

[2] Danson, M. J., Cronje, W. A., Design of a Double-Sided Tubular Permanent-Magnet Linear Synchronous Generator for Wave-Energy Conversion, *Int. J. for Computation and Mathematics in Electrical and Electronic* Engineering, *27* (2008), 1, pp. 154-169

[3] Lim, H. S., *et al*., Design and Control of a Linear Propulsion System for an Elevator Using Linear Switched Reluctance Motor Drives, *IEEE Trans. Ind. Electron*., *55* (2008), 2, pp. 534-542

[4] Onat, A., *et al*., Design and Implementation of a Linear Motor for Multi-Car Elevators, *IEEE/ASME Transactions*, *15* (2010), 5, pp. 685-693

[5] JimEnez, J., *et al*., Coupled Electromagnetic and Thermal Design of Miniaturized Permanent Magnet Linear Motors for Sliding Door Applications, *Int. Rev. Electr. Eng*., *8* (2013), 5, pp. 1416-1426

[6] Li, L. Y., *et al*., Analysis and Optimization of Air-Core Permanent Magnet Linear Synchronous Motors with Overlapping Concentrated Windings for Ultra-Precision Applications, *Proceedings*, 15th International Conference on Electrical Machines and Systems (ICEMS), Sapporo, Japan, 2012, pp. 1-6

[7] Milošević-Mitić, V., *et al*.,. Dynamic Temperature Field in the Ferromagnetic Plate Induced by Moving High Frequency Inductor, *Thermal Science*, *18* (2014), Suppl., pp. S49-S58

[8] Nituca, C., *et al*., Pantograph Drived with a Linear Induction Motor Controlled with Adaptive Fuzzy Control, *Proceedings*, 4th International Conference on Electromechanical and Power Systems SIELMEN 2003, Chisinau, Rep. Moldova, 2003, Vol. III, pp. 55-58

[9] Nituca, C., *et al*., Constructive and Experimental Aspects Regarding the Electric Power Collecting for very high speed train, 6th Int. Conf. on Electromechanical and Power Systems SIELMEN 2007, *Analele Univ. din Craiova*, *31* (2007), II, pp. 290-293

[10] Kim, J. J., *et al*., Thermal Behavior of a Machine Tool equipped with linear motors, *Int. J. of Machine Tools and Manufacture*, *44* (2004), 7-8, pp. 749-758

[11] Sarapulov, F. N., Goman, V. V., Development of Mathematical Models of Thermal Processes in Linear Asynchronous Motors, *Russian Electrical Engineering*, *80* (2009), 8, pp. 431-435, Allerton Press, Inc., 2009. Original Russian Text, Published in Elektrotekhnika, Sarapulov, F. N., Goman, V. V., 8 (2009), 8, pp. 17-21

[12] Plesca, A., Thermal Analysis of Fuses and Busbar Connections at Different Type of Load Variations, *Int. Rev. on Modelling and Simulations* (*IREMOS*), *3* (2010), 5, Part B, pp.1077-1086

[13] Tarchutkin, N. V., *et al*., Modeling of Thermal Operating Modes of a Linear Electrical Machine in a Strong Coupled Task, Young Researchers in Electrical and Electronic Engineering (EIConRus), *Proceedings*, 2018 IEEE Conference of Russian, Moscow, (2018), pp. 819-821

[14] De-Shau, H., *et al*., Three-Phase Linear Motor Heat Transfer Analysis Using the Finite-Element Method, *Journal Heat Transfer Engineering*, *31* (2010), 7, pp. 617-624

[15] Chevailler, S., Comparative Study and Selection Criteria of Linear Motors, Ph. D. Thesis, Ecole Polytechnique Federale de Lausanne, Lausanne, Switzerland, 2006

[16] Sarapulov, F., *et al*. Dynamic Study of Thermal Characteristics of Linear Induction Motors, Electrical Machines, Drives and Power Systems (ELMA), *Proceedings*, 15th Int. Conf. on Electrical Machines, Drives and Power Systems, Sofia, 2017, pp. 414-418

[17] Lee, M. G., *et al*., Design of High Precision Linear Stage with Double-Sided Multi-Segmented Trapezoidal Magnet Array and Its Compensations for Force Ripples, *Mechatronics*, *16* (2006), 6, pp. 331-340

[18] Chow, J. H., *et al*., Investigation of Thermal Effect in Permanent Magnet Linear Motor Stage, *Proceedings*, 11th Int. Conf. on Control, Automation, Robotics and Vision, ICARCV 2010, Singapore, 2010, pp. 258-262

[19] Chow, J. H., *et al*., A Finite-Difference Thermal Model of a Three-Phase Coreless Linear Motor as a Heat Source, *Applied Thermal Engineering*, *87* (2015), Aug., pp. 605-614

[20] Ying, X. , Wang, Y., 3-D Temperature Field Analysis of the Induction Motors with Broken Bar Fault, *Applied Thermal Engineering*, *66* (2014), 1-2, pp. 25-34

[21] Nair, D. G., Arkkio, A., Inverse Thermal Modelling to Determine Power Losses in Induction Motor, *IEEE Transactions on Magnetics*, *53* (2017), 6, 8103204

[22] Venkataraman, B., *et al*., Fundamentals of a Motor Thermal Model and its Applications in Motor Protection, *Proceedings*, 58th Annual Conf. for Protective Relay Engineers, Jacksonville, Fla., USA, 2005, pp. 127-144

[23] Nituca, C., Thermal Analysis for a Double Sided Linear Induction Motor, *European Scientific Journal*, *9* (2013), 9, pp. 38-50

[24] Chiriac, G., Thermal Analysis for a Bilateral Linear Induction Motor with Sectioned Plate Armature, *European Scientific Journal*, *9* (2013), 9, pp. 45-56

Paper submitted: April 20, 2018
Paper revised: May 28, 2018
Paper accepted: June 22, 2018

applied sciences

MDPI

Article

Electric Bus Indoor Heat Balance in Cold Weather

Gabriel Chiriac [1], Dumitru Dorin Lucache [1], Costică Nițucă [1], Alin Dragomir [2,]* and Seeram Ramakrishna [3]

[1] Department of Energy Utilisation, Electrical Drives and Industrial Automation, Faculty of Electrical Engineering, "Gheorghe Asachi" Technical University of Iasi, Bd. Dimitrie Mangeron, 21-23, 700050 Iasi, Romania; gchiriac@tuiasi.ro (G.C.); dorin.lucache@tuiasi.ro (D.D.L.); costica.nituca@tuiasi.ro (C.N.)

[2] Department of Power Engineering, Faculty of Electrical Engineering, "Gheorghe Asachi" Technical University of Iasi, Bd. Dimitrie Mangeron, 21-23, 700050 Iasi, Romania

[3] Department of Mechanical Engineering, College of Design and Engineering, National University of Singapore, 21 Lower Kent Ridge Road, Singapore 119077, Singapore; seeram@nus.edu.sg

* Correspondence: alin.dragomir@tuiasi.ro

Abstract: The use of electric buses is increasing all over the world; this is due to the aim of limiting pollution in heavily urbanized areas. Using electric buses is one element of the desire to drop local pollution to zero emissions. The necessary electricity can be generated through centralized production, and in the case of electric buses, the pollution level is directly proportional to the amount of electricity produced. Their limited onboard power needs optimization, both in terms of traction and in auxiliary energy consumption. Heating in electric buses consumes the most energy from the auxiliaries, which can reduce the range of the vehicle up to a half, or more in the coldest days of the winter months. In this context, a precise estimation of heat loss and of the energy necessary for heating electric buses is crucial. Using the heat transfer theory, the heat balance method, and the U-value estimation, this article estimates the heat loss for a typical 12 m electric bus for a harsh winter day. Thermal simulations were made in order to estimate the heat flux through the structure of the bus (windows, walls, roof, and floor). Heat loss components were calculated in order to determine the most affected zones of the bus. The calculated data for the energy necessary to heat the bus were compared with the heating system data from an electric bus. By optimizing the necessary auxiliary energy consumption, the emissions at the source of electricity production will be significantly reduced.

Keywords: electric buses heating; heat loss; heat balance method; U-value; thermal modeling

Citation: Chiriac, G.; Lucache, D.D.; Nițucă, C.; Dragomir, A.; Ramakrishna, S. Electric Bus Indoor Heat Balance in Cold Weather. *Appl. Sci.* **2021**, *11*, 11761. https://doi.org/10.3390/app112411761

Academic Editor: Luis Hernández-Callejo

Received: 5 November 2021
Accepted: 8 December 2021
Published: 10 December 2021

1. Introduction

With the accelerated evolution of the development and utilization of electric vehicles, and with many constraints related to energy consumption and environmental pollution, there is more and more research being published related to electric vehicles, giving attention to various goals, such as: reducing energy consumption, improving efficiency for the electric motors, optimizing the auxiliary systems, improving the energy storage capacity, and developing charging system capabilities for the electric vehicles.

Along with these aspects, the thermal comfort of the passengers and drivers, even in extreme conditions, are being studied worldwide, from small electric cars to large electric vehicles, such as electric buses.

Electric buses have many benefits compared with their thermal engine counterparts: they have no emissions and do not pollute the air, they are low noise vehicles and have fewer vibrations, offering superior comfort for the passengers and, importantly, they can use locally produced (and renewable) electric energy.

To make the transition from the conventional engine buses to the electrical ones, authorities and public transport operators have to invest not only in the establishment and development of electric bus fleets but also in new infrastructure. Some countries are planning to ban vehicles with thermal engines, while in some cities there are areas considered to be low or zero emission zones. Some cities are part of the C40 Fossil Fuel Free Street Declaration, which promotes the use of only zero emission buses by 2025, asserting that most of the participating cities will use emission-free vehicles by 2030 [1].

More than 1 million buses are used in Europe and around 690,000 buses are in use in the European Union, with the average age of the buses being about 12 years. Thermal engine buses account for more than 94% of the EU fleet, and less than 2% are battery electric or hybrid electric buses [2].

Some limitations are still obstructing the expanding use of electric buses, as follows:

- The limited range and power, as compared with conventional thermal buses.
- The necessity of new infrastructures, such as the power grid and systems for battery charging.
- The availability of personnel qualified in technologies different from conventional vehicles, for the maintenance of the electric buses.

There are various types of electric buses, which vary depending on whether electrical energy is generated or stored onboard. Hybrid electric, fuel cell electric, and full battery electric buses are currently being used around the world [3].

Hybrid electric buses use both an internal combustion engine and an electric motor to power the vehicle. Because they have partially a similar technology as traditional engine buses, they are a convenient transition to electric vehicles; however, they raise the same issues as classical vehicles (air pollution and dependence on conventional fuel).

Fuel cells are based on a chemical reaction between stored hydrogen and ambient oxygen to generate electricity. They assure long range and low emissions but are expensive and require a special infrastructure to store the hydrogen and to refuel the vehicles.

Full battery electric buses store all the necessary energy in an onboard rechargeable battery pack. They have no emissions and are energy efficient but have limited distance range and require a charging infrastructure [3].

Moreover, there are various charging systems, such as overnight charging (large size batteries are charged statically from the grid at the depot, mainly during the night, for up to 5–8 h); opportunity charging (medium size batteries are recharged at passenger stopping points or at the bus terminals); or a combination of depot charging and opportunity charging.

Irrespective of the types of electric bus and charging system, the energy from the power source is used for the traction needs and for the auxiliary systems on the vehicle (ventilation, heating, cooling, interior and exterior lights, passenger information devices, ticket vending machines, and others).

The energy required by the auxiliaries could reach up to 35% of the total energy consumption of the electric vehicle, and, depending on the environment conditions—especially the external temperature—the non-traction needs could consume up to 50% of the total energy on vehicles [4], or even up to 70% in very cold days in winter, when the heating system is used at full power [4,5]. Thus, the reduction in energy used for non-traction needs is a main challenge in order to reduce the total energy demand on the electric buses. It is particularly important for battery vehicles, because the batteries—as the energy source—have a limited capacity and limited range [4].

From all the auxiliaries, the heating and cooling consume the most energy—up to 35% [6]. Moreover, the temperature inside the vehicles depends on the cabin volume: at the same driving conditions, a large vehicle has a different temperature than a small class one. The class of the vehicle, reflected in the quality of the equipment and materials, will also influence the warming and cooling of the vehicle [7].

Conventional vehicles use internal combustion engines, which produce enough waste heat to heat up the vehicle, through the engine cooling circuit via a heat exchanger. Nevertheless, modern thermal engines are more efficient and produce less waste heat; therefore, supplementary electric heaters are necessary to heat the cabin in cold conditions [8].

Electric vehicles use electric motors which generate low amount of waste heat [8]. Even the heat released from the main battery pack is not enough to heat the interior of an electric bus, being needed for other heat sources. Therefore, the energy for the heating system is supplied by the power source, the battery pack, which is mainly used for driving and has limited capacity.

The heating has a significant influence over the range of the electric vehicle, reducing the range of the electric vehicle by half, or even more with an external air temperature of 0 °C [5].

In order to decrease the energy consumption for the HVAC systems on electric buses, several solutions have been proposed, as follows [8–11]: using recovery heat from the traction batteries; an integrated air conditioning and heating system; improved control systems for the heating system; door air curtains/air screened doors to reduce the heat exchange between the inside and outside of the bus [12]; heat pumps; thermal pre-conditioning; complex additional heating equipment. Infrared radiation heating in the vehicle cabin has also been studied for electric vehicles [13,14]. Solid media high-temperature thermal energy storage systems are also being researched for battery electric vehicles [15].

However, many of the above solutions are based on well-known methods, combined with improved strategies for control and optimization.

Therefore, research aiming to improve the heating are in demand for electric vehicles, in order to consume less energy while maintaining passengers' thermal comfort. Thus, new HVAC systems structures and advanced control will bring the best benefits, rather than using advanced cabin materials or increasing thermal isolation [8].

Urban road transportation usually uses technologies adapted from the car industry. In public transportation, where the doors open frequently, allowing passengers to exit and enter the vehicle, it is difficult to ensure a high comfort level. The most common solution for the heating system involves the use of engine cooling water, along with electrical resistance heating [12].

A combined heating configuration composed of zonal air flow and heated surfaces—driver seat, steering wheel, and floor mat—can reduce the heating energy by up to about 28%, while maintaining an equivalent thermal sensation. By simulation, [16] found that the combination of zonal air and surface heating can lead to a 7–19% improvement of the bus range.

Cabin preheating could also increase an electric vehicle range from 4% to 10% for 20 min of pre-conditioning [8]. There are basically two ways of reducing the power consumption for heating the electric vehicles, as follows: (1) reduction in heating loads and (2) improvement of the thermal system efficiency [8].

The heated load for an electric vehicle includes ventilation load and ambient load. The ventilation load is necessary for two reasons, as follows: the first is to assure the air quality inside the cabin (to keep a low concentration of CO_2) and the second is to prevent fogging on the windshield and on the other windows [9]. Using recirculated air is a method of reducing the ventilation load, along with using a low thermal conductivity glass for the windshield and windows.

The ambient load is a product of the temperature difference between the cabin air and the external environment, because the heat flows through the vehicle body structure. Some studies on using thermal isolation materials for vehicles showed up to 18% less heating load. On the other hand, thermal isolation does not always solve the issues, because it can lead to a strong greenhouse effect during the warm days in summer [9].

Zonal heating and inner surface heating (heated seats) are also methods of reducing the heating loads requirements.

In this article, the main goal was to calculate the heat loss for a typical 12 m electric bus, considering the conditions of a harsh winter day in Romania. Heat loss components were calculated in order to determine the most affected zones of the bus. The analyzed vehicle was actually a trolley bus (supplied from the contact lines), which has been adapted to also operate independently on traction batteries during its route. Due to the limited onboard battery, the distance to be covered as an autonomous vehicle is quite limited, especially in cold weather in winter, when the heating system is in use and the necessary power for the heating system is very high (up to 30 kW). The goal of our work was to calculate the heat loads inside this specific electric vehicle, with the aim to find the possibilities for optimizing the energy consumption for this type of vehicle.

Thermal simulations were carried out in order to estimate the heat flux through the structure of the bus (windows, walls, roof, floor, and doors). The calculated data for the necessary energy to heat the bus were compared with the heating system data from a real electric bus.

2. Heat Balance for an Electric Bus

Optimal energy consumption and interior thermal comfort for the passengers can be calculated and modeled by using heat transfer theory, the heat balance method, and the U-value (thermal transmittance) [17]. Based on the heat transfer theory, there are three mechanisms for transferring heat: conduction, convection, and radiation. Heat transfer into the electric bus is a complicated process, due to the complexity of the vehicle (windows, walls of various layers, floor, roof, and doors) and because all three of the heat transfer mechanisms are present.

2.1. Heat Conduction

Conduction appears inside a solid material or between two solid materials and follows Fourier's law for one-dimension, with a temperature gradient inside the material being required for heat transfer. Thus, considering the one dimension as x direction, a solid material, for which k is the thermal conductivity, and for a local thermal gradient of $\frac{dT}{dx}$, the conduction heat flux (q_{cond}) through the material can be calculated with the following equation:

$$q_{cond} = -k\frac{dT}{dx}, \tag{1}$$

The heat transfer by conduction in electric buses presents in areas such as the windows, the walls, the roof, the floor, the doors, and any other object inside the vehicle (the seats, for example).

2.2. Heat Convection

Convection is an important method of heat transfer for fluids, both inside the fluid and for fluids in contact with solids, and it can be natural or forced convection. Considering the temperature of the fluid T_{fluid} and the temperature of the body T_{body}, the heat flux resulting from convection can be calculated as shown in Equation (2), where the constant, h, is the heat transfer coefficient, as follows:

$$q_{conv} = h\left(T_{fluid} - T_{body}\right), \tag{2}$$

Convection in electric buses takes place at the contact between the surfaces of the walls and the fluids such as air (inside the bus) and the air or rainwater (outside the bus). While in the interior the convection has a low variation, on the outside it is amplified with the increase of the bus speed.

2.3. Heat by Radiation

Radiation is the only energy transfer mechanism that does not need a material support and depends on the source's temperature and the source's surface properties. For cold bodies, the heat transfer is negligible compared with convection and conduction. Based on the Stefan–Boltzmann law for a black body, this energy emission can be calculated as follows:

$$q_{rad}(T) = \epsilon \cdot \sigma \cdot T^4, \tag{3}$$

where ε is the emissivity of the body, σ is the Stefan–Boltzmann constant, and T is the temperature of the body [K].

The main radiation heat load for a bus is caused by the Sun, and, depending on the weather conditions and the seasons, it can have an important contribution to the heat load balance (during a sunny day at midday) or it may have low impact in heating a bus (during a cloudy and cold winter day).

2.4. Heat Balance Method for Vehicles

The heat balance method is a common method for calculating heating and cooling loads in a given space or zone [17]. Based on this theory, all heating loads can be written in a comprehensive equation. Four distinct processes can be assumed for the heat balance into an electric bus, as follows:

1. Outdoor surface heat balance.
2. Indoor surface heat balance.
3. Wall conduction.
4. Inside zone air heat balance.

For an optimal design of the heating system inside the bus, it is crucial to accurately determine the heating loads, because underestimating them may lead to thermal comfort problems, while an overdesign may increase the manufacturing and operating costs for the vehicle [18].

Various heat loads must be considered, but there are eight main heat components to estimate in the modeling and calculation of a vehicle cabin's thermal balance [8,18–20], as follows (Figure 1):

1. Metabolic heat load generated by the passengers—$\dot{Q}_{met}$.
2. Solar heat loads (caused by the Sun's radiation) with three components—$\dot{Q}_{sun}$, as follows:
    - Direct radiation from the Sun;
    - Diffused radiation due to the dispersion in the atmosphere;
    - Reflected radiation from the ground and other surrounding surfaces.
3. Heat load due to the electric motors—$\dot{Q}_{mot}$.
4. Heat load generated by the traction battery—$\dot{Q}_{bat}$.
5. Heat load due to the fresh air supplied by ventilation, which is necessary for passengers' needs—$\dot{Q}_{ven}$.
6. Heat flow changed with the ambient load, due to the temperature gradient between the bus structure (windows, walls, floor, roof, and doors) and the exterior environment—$\dot{Q}_{amb}$.
7. Heat flow changed with the ambient load, due to the doors opening during stops in stations—$\dot{Q}_{door}$.
8. Heat load generated by the heating system from the vehicle in order to assure the thermal comfort for passengers—$\dot{Q}_{hsyst}$.

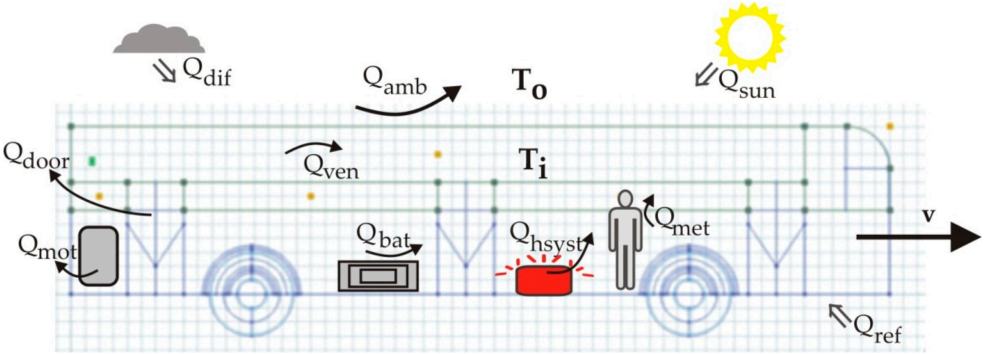

Figure 1. Schematic representation of heat loads: a model for a typical electric bus.

Thus, considering the above heat components, the heat load model for an electric bus is given by Equation (4):

$$\dot{Q}_{total} = \dot{Q}_{met} + \dot{Q}_{sun} + \dot{Q}_{mot} + \dot{Q}_{bat} + \dot{Q}_{ven} + \dot{Q}_{amb} + \dot{Q}_{doors} + \dot{Q}_{hsyst}. \tag{4}$$

3. Heat Load Estimation for an Electric Bus

The necessary power for heating the cabin of the electric buses is estimated in some studies, including [4,6,21,22]. According to [6], the energy consumption for heating a bus can reach up to 35% of the main battery's energy. In [4], data is presented for 12 m electric buses, with the necessary heating power varying from 5 kW up to 25 kW in absolute value, depending on the weather conditions and the time of the day.

In case of resistance heating, the energy demand can, in a worst-case scenario, double or even almost triple the vehicle's energy consumption. From measurements on a 12 m electric bus, it was estimated that the average electric power necessary to keep the cabin's temperature at 17 °C on a cold winter day with a −10 °C environment temperature was about 24 kW [21].

Another calculation estimates a heat loss of about 17.4 kW for a 12 m length bus, depending on the materials of the vehicle and considering only the thermal conduction through the structure of the bus and the heat loss through the open doors [22].

In this article, for the heat loss estimation, a typical low floor electric bus, with the following characteristics, is considered [23]: 12 m length, 100 passengers capacity, 150 kW electric motor, 3 doors, maximum speed 60km/h. The heating system of the bus has an installed power of 33 kW and is composed from 4 heaters of 6 kW each, used to heat the passengers' cabin, and a 9 kW heater for the driver's area. The vehicle is operating mainly as a trolley bus (supplied form the contact lines), and it is adapted to operate also independently on traction batteries during its route.

The estimation of the heating loads assumes difficult case conditions of a cold day in winter with a −10 °C temperature of the outside environment. Heat loads are calculated for continuous working conditions and the heat load required at first start of the bus was neglected at this stage.

The aim was to estimate the rate of heat to be added inside the vehicle by the heating system in order to maintain the desired conditions for thermal comfort, with a temperature of 20 °C being considered for the interior of the vehicle. Additionally, the heat loss by its component is to be determined in order to estimate the area consuming the most energy.

3.1. Metabolic Heat Load Generated by the Passengers, $\dot{Q}_{met}$

Because passengers of a bus sit and stand, the heat load can be estimated separately, as in [18], with the metabolic heat production rates of 60 W/m^2 and 70 W/m^2, respectively, and with 120 W/m^2 for the driver of the bus. These values are related to the surface area of a person, of about 1.80 m^2 [18]. Other authors [24] consider, for the sitting passenger, 55 W/m^2 and 85 W/m^2 for the driver.

Taking into consideration that, during the cold days in winter, the heat released by the human body into the surroundings is limited because the people are dressed in thicker clothes—these thermal values are to be considered for their lower values. Thus, for the calculation, a medium value of 60 W/m^2 is accepted, which, for a person, results in 60×1.8 m^2 = 108 W.

Buses are rarely at their full capacity, the average occupancy of a city bus being less than 40%, or even about 30% [25]; therefore, for the heat load generated by 40 passengers, a 4.32 kW value is estimated.

3.2. Solar Heat Loads—$\dot{Q}_{sun}$

3.2.1. Direct Radiation from the Sun

Heat gain, due to direct radiation, depends on the direct normal irradiance—the incident angle of the radiation—on the area and the transmissivity of the surface. The heat gain due to the direct radiation can be estimated as follows [18]:

$$\dot{Q}_{sunDir} = A \cdot \tau \cdot I_{Dir} \cdot cos(\theta) \quad [\mathrm{W}], \tag{5}$$

where A is the surface area [m^2], τ is the transmissivity of the material, I_{Dir} is the direct normal solar radiation [W/m^2], and θ is the incident angle of the solar radiation.

3.2.2. Diffused Radiation Due to the Dispersion in the Atmosphere

This is a heat gain due to the dispersion of the solar radiation on the atmosphere and has specific calculation formula [18], as follows:

$$\dot{Q}_{sunDif} = A \cdot \tau \cdot I_{Dif} \quad [\mathrm{W}], \tag{6}$$

where A is the surface area [m^2], τ is the transmissivity of the material, and I_{Dif} is the diffused solar radiation [W/m^2].

3.2.3. Reflected Radiation Due to the Ground

In this case, the heat gain is due to the radiation reflected by the ground. Taking into account the winter weather, when the roads are cold, this heat gain is to be considered as negligible for our calculation.

3.2.4. Solar Heat Gain Estimation for Romania

Romania is situated in the Central to East European continent area, between 43°37′ and 48°15′ latitude North, and 20°45′ and 29°41′ longitude East, having a temperate continental weather, with about 6 months of cold weather (from October to March). January and December are the coldest months of the year, with average temperatures of about −6 °C at midday, with lower temperatures (down to −10 °C) during mornings and evenings, and with minimum temperatures of down to −24 °C (based on the official data from the National Meteorological Administration from Romania [26]). During this 6-month period, the solar irradiation to be considered is usually between 9.00 and 15.00 h of the day (direct radiation load decreases due to the decrease in the sun elevation angle for the simulation period, which happens after midday [24]), having clear sky for about 40% of the day [27].

The solar heat gain for a bus varies permanently because it depends on a multitude of factors: time of day, clear or covered sky, the angle of incidence of solar radiation, the variable position of the vehicle, the possibility of shading it depending on the route (especially in the urban areas, with boulevards sheltered by high buildings), varying surfaces, and the transparency of the windows, etc. Therefore, the estimation of heat gain from solar radiation can only be carried out roughly, considering several simplifying hypotheses.

Existent data about the solar irradiation in Bucharest, the Romanian capital, during December and January are summarized in Table 1—global irradiation includes measurements for both direct and diffused solar radiation.

Table 1. Global irradiation includes measurements for both direct and diffused solar radiation.

	Hourly Average of Sun's Brightness, around 12 O'Clock	**Hour**	**9**	**12**	**15**	**Daily Irradiation Average, [W/m^2]**
				Global Solar Irradiation, [W/m^2]		
December	0.36	Clear sky	89	145	85	106.3
		Overcast sky	25	68	24	39.0
January	0.39	Clear sky	130	280	132	180.7
		Overcast sky	65	145	68	92.7

If HA_{12} is the "Hourly average of Sun's brightness, around 12 o'clock", and I_{glC} and I_{glO} are the global solar irradiation for the clear sky, respectively, for the overcast sky, then the maximum solar irradiation of the bus happens at noon and can be calculated with the following relation:

$$I_{Max} = HA_{12} \cdot I_{glC} + (1 - HA_{12}) \cdot I_{glO} \quad [\mathrm{W/m^2}], \tag{7}$$

With the data in Table 1, the above relation shows I_{Max} = 197.7 W/m^2. However, the solar irradiation of the bus during these two winter months manifests for maximum of 6 h per day and not all is transformed into the heat. Factors that reduce solar heat inputs, such as the transmissivity of windows, exterior shading, and reflective surfaces, etc., must be taken into account.

The 12 m bus has a transparent window area of 29 m^2, and for a double pane window the transmissivity is τ = 0.75 [18]. Keeping the same hourly average of Sun's brightness and applying Relation (7) for the daily average of solar irradiations, the average heat gain is given in Table 2 for both of the winter months considered.

Table 2. Average heat gain for both direct and diffused solar radiation.

	HA_{12}	Average Solar Irradiation, [W/m^2]	Bus Windows Area, [m^2]	τ	Average Heat Gain [kW]	Daily Average Heat Input, [W/m^2]
December	0.36	63.24	29	0.75	1.38	8.25
January	0.39	126.99			2.76	16.57

The presented calculation is a rough estimation of the heat gain and daily heat input. Contributions of the shading factor or reflected radiation, due to the ground, are neglected. Results showed that the most demanding month for the heating installation is December.

3.3. Heat Flow Due to the Fresh Air Supplied by Ventilation, Which Is Necessary for Passengers' Needs—$\dot{Q}_{ven}$

Ventilation and ambient loads are functions of the temperature difference between the cabin and the ambient load. The air flow rate for the buses depends on the operating of the air conditioning system, with values between the 0.05 m^3/s and 0.3 m^3/s [28]. For the city buses with frequently stops, the fresh air supplied by ventilation is dominated by the air flow through the open doors, and the ventilation can be used for the lower value, which is 0.05 m^3/s [28]. Heat transfer due to the ventilation can be estimated with Formula (8) and depends on the temperature difference (ΔT), the specific heat, the air density (ρ_{air}) and the air flow rate ($\dot{V}$) [29], as follows:

$$\dot{Q}_{ven} = \dot{V} \cdot \rho_{air} \cdot c \cdot \Delta T \quad [\mathrm{W}], \tag{8}$$

For an air flow rate of 0.05 m^3/s, an air density of 1.27 kg/m^3, a specific heat of 1009 J/kg*K, and a gradient of temperature of 30 °C, the heat transfer due to the ventilation is $\dot{Q}_{ven}$ = 1.922 kW.

3.4. Heat Flow Changes with the Ambient Load Due to the Temperature Gradient between the Bus Structure and the Exterior Environment (Ambient Heat Load)—$\dot{Q}_{amb}$

Heat transfer takes place from warm bodies (areas) to colder bodies (areas). So, in the winter cold days, the heat transfer takes place from the heated bus cab to the cold outside environment Thus, a large amount of heat is loss into the atmosphere through the windows, walls, roof, floor, and doors. This heat loss depends on the area of the surfaces, on the heat transfer coefficient (for each material or an overall estimated coefficient), and on the inside and outside temperatures. The heat transfer is estimated considering the conduction through solid materials, the convection between the interior air in the bus and the inner surfaces, and the convection between the exterior air and the outer surfaces of the bus (Figure 2).

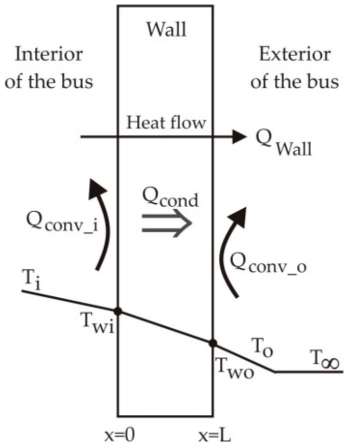

Figure 2. Heat loss through a wall of an electric bus.

For a wall composed by a single layer, the heat transfer is calculated with the following equation:

$$\dot{Q} = A \cdot U \cdot (T_i - T_o) \quad [\mathrm{W}], \tag{9}$$

where A is the cross-sectional area [m^2], U is the heat transfer coefficient [W/m^2 K], T_i is the inside temperature [°C], and T_o is the outside temperature [°C],

The heat transfer coefficient is calculated as a combination of conductive and convective heat transfer, which is given by [18]:

$$\frac{1}{U} = \frac{1}{h_i} + \frac{L}{k} + \frac{1}{h_o}, \tag{10}$$

where h_i is convective heat transfer coefficient between the interior air and the inner surfaces of the wall [W/m^2 K], h_o is the convective heat transfer coefficient between the exterior air and the outer surfaces of the wall [W/m^2 K], L is the thickness of the wall [m], and k is the conductive heat transfer coefficient of the wall [W/mK].

For the vehicles, the convection coefficients of the outer surfaces depend on the vehicle speed, and for the inner space, the coefficient depends on the air speed inside, relative to the inner surfaces [18], as follows:

$$h = 9 + 3.5v^{0.66} \quad [\mathrm{W/m^2\,K}], \tag{11}$$

with v as the relative air speed to the surface [m/s].

In order to estimate the heat loss as accurately as possible, for the walls composed by multiple layers, the thermal contact resistance between the layers of the bus structure will be considered also. Thus, knowing the heat loss on its components will be possible to estimate the possibilities to improve the bus structure to reduce the heat loss.

With limited information on the roughness profile, the density, and the radii of the contact spots, the estimation of the thermal contact resistance brings uncertainty into the calculation. Considering [30–32], the thermal contact resistance of the interface between two layers is given by the ratio between the difference of temperatures along the interface and the heat, $\dot{Q}$ [W], as follows:

$$R_c = \frac{\Delta T_{interface}}{Q} \quad [\mathrm{K/W}], \tag{12}$$

where $\Delta T_{interface}$ is the difference of temperature along the layers' interfaces.

Based on heat flux, $q = \dot{Q}/A$ [W/m^2], related to the surface area, the resistance can be considered as follows:

$$r_c = \frac{\Delta T_{interface}}{q \cdot A} \quad [\mathrm{K/m^2W}], \tag{13}$$

Thus, for a multiple layered wall (with thicknesses (L_j) and conductive heat transfer coefficient (k_j)), the overall heat transfer coefficient must be calculated, including the thermal contact resistances between the layers, as follows:

$$\frac{1}{U} = \frac{1}{h_i} + \sum \frac{L_j}{k_j} + \frac{1}{h_o} + \sum r_{cj}, \quad [\mathrm{K/m^2W}], \tag{14}$$

where L_j, and k_j are the thickness and conductive heat transfer of the layer j, and r_{cj} is the thermal resistance for the layer interfaces.

3.4.1. Heat Loss through the Windows of the Bus—$\dot{Q}_w$

The heat lost through the windows is estimated as heat loss due to conduction through the windows and due to the convection to the interior and exterior air. There are various types of windows used for the buses, differing by glass thickness, the quality of the glass (clearness), or by the types of the windows (one layer or two layers with inside air isolation). For this calculation, it was assumed that the windows have a single layer of 6 mm glass thickness and the area of the windows of the bus is 29.0 m^2.

Using Formulas (8)–(10) and a vehicle speed of 40 km/h (11.1 m/s) (as the maximum speed for the city movement of the bus), the heat loss calculated for the all window area of the bus is $\dot{Q}_w$ = 5612 W, for U value = 6.45 W/m^2 K.

For the air inside the vehicle, the speed is assumed to be zero, so h_i = 9 [W/m^2 K], and k = 1.05 [W/mK] is the conductivity of the glass.

In order to estimate the real temperature on the surfaces of the windows, a simulation using Comsol Multiphysics software has been performed. The simulations were made for the steady-state regime by modeling the geometry of the bus structure and considering the actual values for the parameters of the materials.

Figure 3 shows the thermal simulation through a window of the bus considering an inside temperature of 20 °C (left side of the image) and an exterior temperature of −10 °C (on the right side of the image). The exterior temperature was chosen assuming a difficult case scenario for the month of December in Romania. As can be seen, the temperature on the external side of the glass is of 13.4 °C.

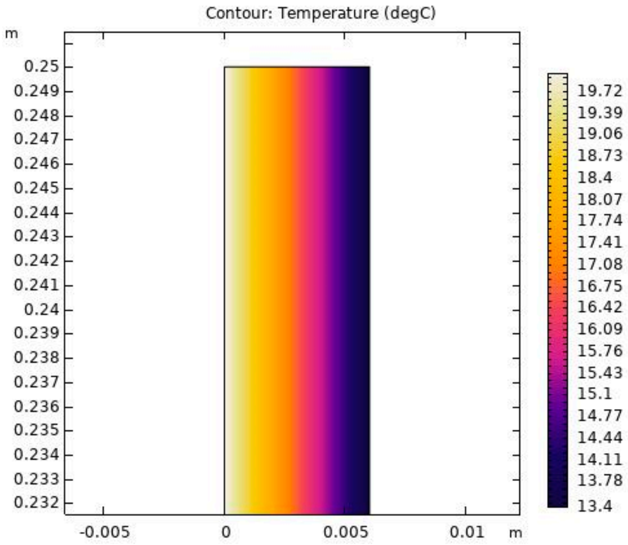

Figure 3. Heat flux variation through the windows of the bus.

3.4.2. Heat Loss through the Walls of the Bus—$\dot{Q}_{wall}$

The walls of the bus are made from three materials, that is (from inside to outside): laminated wood (MDF), polyurethane foam, and a sheet of steel. Their thickness and thermal conductivities are presented in Table 3.

Table 3. Thickness and thermal conductivities for the materials of the wall of the bus.

Material	Thickness [m]	Thermal Conductivity [W/mK]
Iron	0.0008	76.2
Polyurethane foam	0.01	0.04
Laminated wood	0.004	0.107

As for the simulation, in Figure 4a, the model of the three layers of the wall is presented, with a temperature of about −8.1 °C on the exterior wall of the bus, with main thermal loss from the steel and the foam in the wall. The interior side of the vehicle is on the left side of the image (Figure 4a). Vehicle speed is incorporated into the model as the velocity of the fluid (the exterior air).

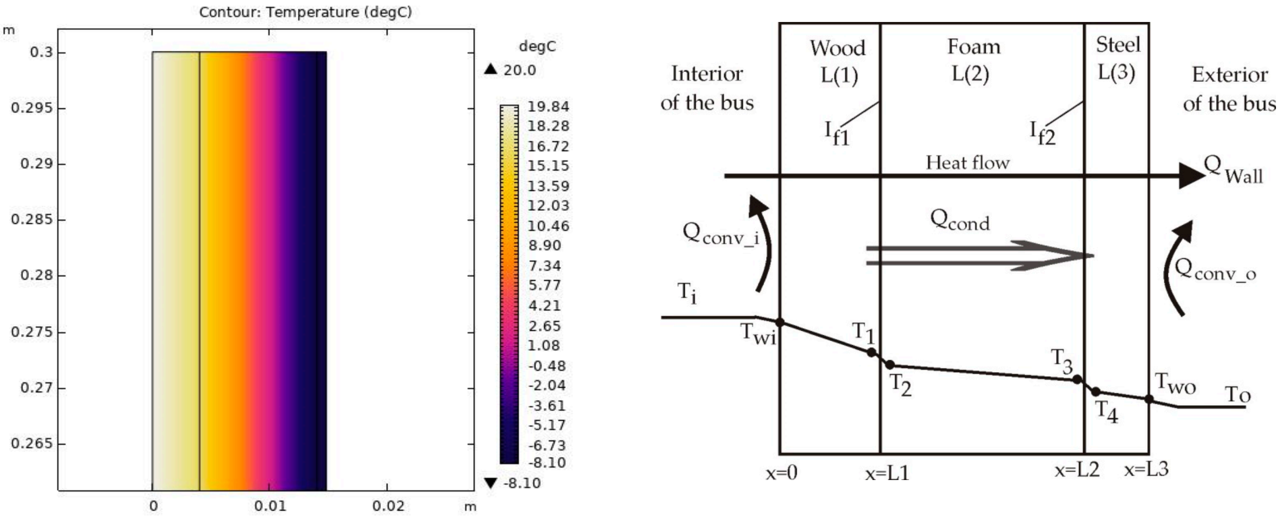

(**a**) (**b**)

Figure 4. (**a**) Heat transfer through the wall. (**b**) Schema of the three layers of the wall of the bus.

For the triple layered wall of the bus (Figure 4b), the overall heat transfer coefficient is calculated as follows:

$$\frac{1}{U_{wall}} = \frac{1}{h_i} + \left(\frac{L_1}{k_2} + \frac{L_1}{k_2} + \frac{L_1}{k_3}\right) + \frac{1}{h_o} + r_{cwall}, \quad [\mathrm{K/m^2W}], \tag{15}$$

The thermal contact resistance for the wall is the sum of the thermal resistance for the two interfaces I_{f1} and I_{f2} (Figure 4b). For the first interface thermal resistance estimation (between the layer of wood, L(1), and foam, L(2)), we assumed that the heat transferred through the surface area of the wall is constant, and we can write the following:

$$\frac{\dot{Q}}{A} = \frac{\Delta T}{\frac{L1}{k1}}, \tag{16}$$

where $\Delta T = T_i - T_1$ [°C] is the difference of temperature along the layer, L(1).

For the interface zone (between the layers L(1) and L(2)):

$$\frac{\dot{Q}}{A} = \frac{\Delta T_{interface}}{r_{c12}}, \tag{17}$$

$\Delta T_{interface} = T_1 - T_2$ [°C], with T_1 and T_2 indicating the temperatures on the interface of the layers L(1) and L(2), between wood and foam layers respectively (Figure 4b).

The interface temperature T_1 and T_2 are estimated from the Comsol simulations (Figure 4a), resulting T_1 = 16.27 °C and T_2 = 16.12 °C.

With these values, and using the Equations (16) and (17), the first interface shows r_{c12} = 0.002 [K/m^2 W]. Similarly, but considering T_3 = −8 °C and T_4 = −8.14 °C, the second interface is calculated, between the second and the third layer, as follows: $r_{c12} = 8{\cdot}10^{-6}$ [K/m^2 W], for the wall of the bus, is r_{cwall} =0.00208 [K/m^2 W].

For the speed of 40 km/h, with 20 °C inside and −10 °C outside temperatures, and for an area of the wall of the bus of A_{wall} = 27 m^2, the U value is determined as U_{wall} = 2.283 W/m^2 K and the heat loss through the wall is $\dot{Q}_{wall}$ = 1849 W.

3.4.3. Heat Loss through the Roof—$\dot{Q}_{roof}$—And the Floor of the Bus—$\dot{Q}_{floor}$

The roof of the bus is composed of a layer of iron sheet, a layer of polyurethane foam (as isolation), and a volume area filled with various equipment (air conditioning, pipes, power supply equipment, and power conductors from the power collecting system). These equipment elements are made mostly from metals and cover about 50% of the roof area. Due to this complex structure of the roof, in order to estimate the U value for the roof, including this complex area (composed of metals materials and air), we consider this area as composed of two parallel layers of metals and air.

The simulation of the heat transfer through the roof is presented in Figure 5a, which shows the differences in temperatures between the metal area of the third layer (on the left) and the air area (on the right of the third layer).

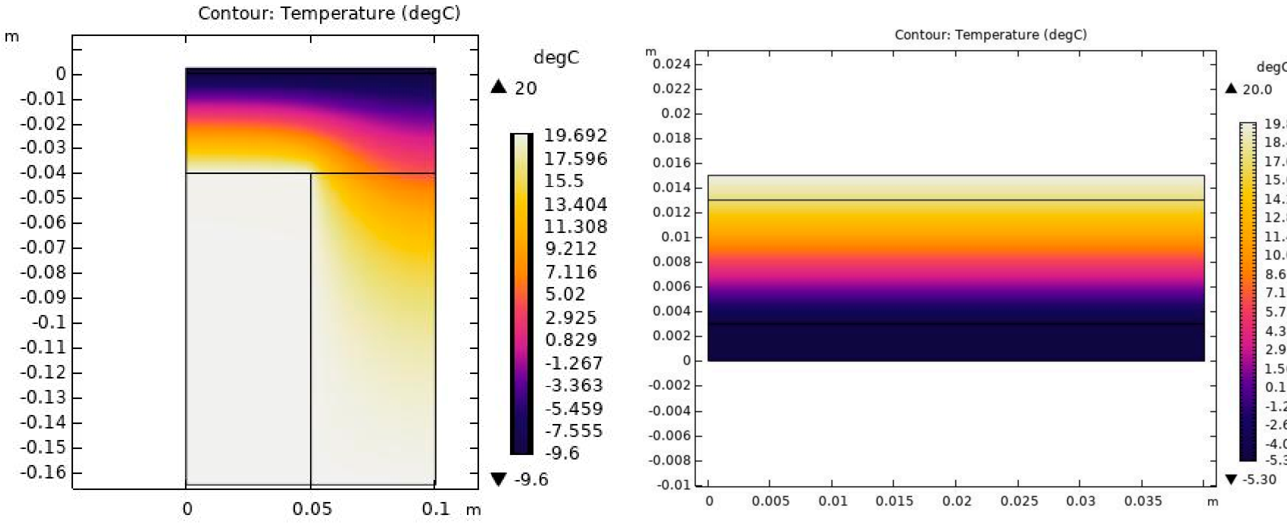

(**a**) (**b**)

Figure 5. (**a**) Heat transfer through the roof of the bus. (**b**) Heat transfer through the floor of the bus.

For the speed of 40 km/h a U value for the roof of 1.87 W/m^2 K, the heat loss is $\dot{Q}_{roof}$ = 1632 W. This calculation include also the thermal resistance of the roof layers (r_{croof} = 0.008 [m^2 K/W]).

The floor is composed of three layers: an iron sheet, a laminated wood layer, and a PVC layer for the intensive transport of people (Table 4). The U value (at 40 km/h) for the floor (including thermal resistance r_{cfloor} = 0.0152 [m^2 K/W]) is 2.747 W/m^2 K and the heat loss is 2425 W.

Table 4. The thicknesses and thermal conductivities for the materials of the floor of the bus.

Material	Thickness [m]	Thermal Conductivity [W/mK]
Iron	0.002	76.2
Laminated wood	0.02	0.107
Polyvinyl/PVC	0.003	0.19

The total heat loss through the windows, walls, roof, and floor of the bus, for a speed of 40 km/h, is determined as $\dot{Q}_{amb}$ = 11,518 W.

The total ambient heat loss (heat loss through the windows, walls, roof, and floor of the bus) is presented in Table 5 for the various speeds of the vehicle (0, 20, 40, and 60 km/h). These values show a significant variation of heat loss between the moment when the bus stops and when it is in motion. It is worth mentioning that the influence of the thermal resistances is less than 3%. Moreover, the differences of heat loss between various speeds are not too high: they are about 3–5%.

Table 5. U values and heat loss through the bus structure into the ambient.

v [km/h]	U Value [W/m^2 K]				$\dot{Q}$Structure [W]				$\dot{Q}amb$ [W]
	Uw	Uwall	Uroof	Ufloor	$\dot{Q}w$	$\dot{Q}wall$	$\dot{Q}roof$	$\dot{Q}floor$	
0	4.4	1.957	1.67	2.272	3832	1585	1458	2004	8879
20	5.988	2.218	1.828	2.66	5209	1797	1595	2346	10,947
40	6.45	2.283	1.87	2.747	5612	1849	1632	2425	11,518
60	6.757	2.32	1.89	2.8	5878	1879	1653	2470	11,880

3.5. Heat Loss Due to the Doors Opening

Estimating the heat loss through the open doors of the bus when it is stopped in stations is quite difficult, due to the air flow complexity between the inside of the bus and the exterior air of the environment, which depends on the random process of the weather conditions and wind speed and direction. The air is assumed to be an ideal gas and is compressible.

When a pressure is applied to the interior air, the volume of the air is modified with a volume equal to the amount of the outside air, which is pressurized into the vehicle cabin, and therefore an air exchange is caused in the process. Some of the income air from outside is mixed with the inside air and is removed through the opening of the doors, due to the airflow direction change and due to the gradient of the temperature and the pressure, this is proportional to the surface area of the opening [33].

The worst-case scenario is when the wind blows directly into the open door, as presented into the cross-section of the bus structure, showing an opened door (Figure 6).

The heat loss through an open door of the bus is estimated with the following formula:

$$\dot{Q}_{door} = \dot{V} \cdot \rho_{air} \cdot c \cdot \Delta T \text{ [W]}, \tag{18}$$

where $\dot{V}$ is the flow rate of the air [m^3/s], ρ_{air} is the air density 1.27 kg/m^3, and c is specific heat of the air 1009 J/kg·K.

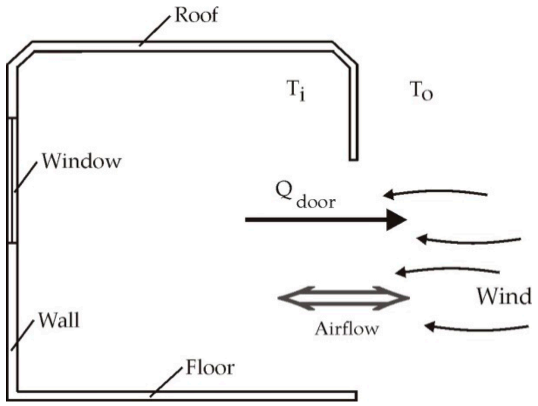

Figure 6. Schema cross-section through the bus structure for an open door.

According to [33], for a single opening enclosure (one open door), for a wind velocity of 10 m/s (a medium wind speed value during a cold day in winter), a flow rate of $\dot{V} = 0.4$ m^3/s for a surface area of 1.44 m^2 is found. Thus, using Formula (17), heat losses result of $\dot{Q}_{door} = 15{,}377$ W for a single open door and, respectively, of $\dot{Q}_{3door} = 46{,}131$ W for all the three open doors of the bus,

Obviously, usually the doors do not stay open too frequently. The average stop time for a city bus is about 30 s [21], with an average running time between stops of 4 min, resulting the doors being open for 1/9 h. As consequence, the hourly heat loss from the open doors is 5.125 kW. Depending on the route, the number of stops, and the number of passengers getting on and off the vehicle, this heat loss may have various values.

3.6. Heat Load Due to the Electric Motors and Heat Load Generated by the Traction Battery

The actual electric vehicles use high efficiency electric motors which generate low amount of waste heat [8]. Even the heat released from the main battery pack is not enough to heat the interior of an electric bus, and for the present calculation of the heat inside the bus these heat losses are considered as negligible.

3.7. Heating System Load to Assure the Thermal Comfort for Passengers

Summarizing the heat loads on the bus, a heat gain of 5.72 kW (the sum of $\dot{Q}_{met}$ and $\dot{Q}_{sun}$) and a loss of energy of 18.5 kW (the sum of $\dot{Q}_{ven}$, $\dot{Q}_{amb}$, and $\dot{Q}_{doors}$) is found. As consequence, the necessary load for the heating system of the 12-m long bus is about 12.79 kW. For higher speeds (max. 60 km/h speed of the bus) and for even harsher winter conditions, this value grows up to 14 kW. This load has to be compensated by the heating system, regardless of the technology used to heat the bus [31].

The analysed existent bus is equipped with 4 heaters of 6 kW in the passengers' cabin and 1 heater of 9 kW in the driver's area. This results in 33 kW of power installed for the electric bus heating system, which, compared with our model, is an oversized heating system [34,35]. The oversizing is only useful for more quickly obtaining the ambient comfort parameters in the bus.

4. Discussion

Research on heating in vehicles is of major importance, especially in cold weather zones, but it is not wide spread over all types of vehicles. Most studies are in the area of automobiles, with few on buses, due to the fact that analyzing and simulating a bus (which is significantly larger and has an intricate structure) is a more complex and time-consuming process.

This article aimed to respond to some of the thermal problems related to electric buses. Estimation of the necessary heat to assure thermal comfort during cold winter days is quite important due to the limited power of these types of electric vehicles. Additionally, along with the limits in energy stored onboard and the vehicles complexity, their particular operating regime results in a complex study due to the various numbers of passengers, doors frequently opening, and the necessity to operate throughout the day.

This study estimates the eight main heat load components on electric buses. Two of them were assumed to be negligible for our thermal model. Firstly, the heat load due to the electric traction motor, and secondly that due to the traction battery pack, as the actual elements are highly efficient.

Therefore, six heat loads were considered for our model: metabolic heat load, Sun heat load, ventilation heat load, ambient heat load, heat flow through the open doors, and the heat load generated by the heating system in the bus. These heat loads were calculated for a 12 m electric bus with the following characteristics: 100 passengers, 150 kW electric traction motor, 3 doors, and 33 kW installed power for the heating system. The calculation was estimated for a harsh winter cold day of December in Romania, with a median temperature of −10 °C. The thermal comfort of the passengers was calculated for a 20 °C temperature inside the bus, resulting a gradient of temperature of 30 °C.

The value of the metabolic heat load depends on the passenger numbers in the vehicle, and the Sun heat load depends strongly on the weather conditions. These heat loads are as a contribution (a heat gain) to the inside bus heating (considered as positive in the thermal model of the vehicle), and, for a harsh day in winter, these represent about 22% and less than 15%, respectively, of the necessary heat of the bus. The heat load from ventilation is an energy-consuming heat load (with energy supplied from the onboard storage system) and it represents less than 10% of the necessary heat for the bus. Being a mandatory system in the vehicle, its contribution to the vehicle heating can be considered to be a heat gain. Thus, these three heat loads assure an input of heat of about 23% of the necessary heat inside the bus.

Heat loss on the bus is composed of the ambient heat loss through the bus structure and the heat loss through the open doors at the stops, with an average value of energy demand of 12–14 kWh. Of these, through the bus structure the heat loss is the most significant, with its four components—the windows, the walls, the floor, and the roof—representing about 78% of the total heat loss. The main heat loss is through the windows (about 26%), while the other three heat loss components have almost the same contribution (about 8.1–8.3% each).

Heat loss through the open doors depends on the route of the bus, the number of stops, and the number of passengers getting on and off the vehicle, with an estimation of 22% of the total heat loss.

The heat load balance led to the conclusion that the heating system must supply a minimum heat load of 18.5 kW. This value is useful for more successfully designing the heating system and managing its operation. The thermal model used in this study allows optimization of the process, by using various less frequently studied heating solutions in order reduce the energy consumption for the heating, and implicitly reduce the CO_2 footprint, while preserving the thermal comfort of the passengers and driver.

Author Contributions: Conceptualization, G.C.; methodology, G.C. and D.D.L.; software, G.C.; validation, G.C., D.D.L. and C.N.; formal analysis, D.D.L. and A.D.; writing—original draft preparation, G.C.; writing—review and editing, A.D.; visualization, A.D. and S.R.; supervision, D.D.L. and S.R.; funding acquisition, G.C. and C.N. All authors have read and agreed to the published version of the manuscript.

Funding: This research and the APC were funded by "Gheorghe Asachi" Technical University of Iasi, Romania, grant number GI/P 9_Idei/2021.

Institutional Review Board Statement: Not applicable.

Informed Consent Statement: Not applicable.

Conflicts of Interest: The authors declare no conflict of interest. The funders had no role in the design of the study; in the collection, analyses, or interpretation of data; in the writing of the manuscript, or in the decision to publish the results.

References

1. Transport & Environment. Electric Buses Arrive on Time. Campaigning for Cleaner Transport in Europe. 2018. Available online: https://www.transportenvironment.org/discover/electric-buses-arrive-time/ (accessed on 8 October 2021).
2. ACEA—European Automobile Manufacturers' Association. Report—Vehicles in Use, Europe 2021. 2021. Available online: https://www.acea.auto/publication/report-vehicles-in-use-europe-january-2021/ (accessed on 8 October 2021).
3. MRC_Electric_Bus_Report__28082017—Electric Bus Technology Transport Research Report. 2017. Available online: https://www.coursehero.com/file/48912037/MRC-Electric-Bus-Report-28082017pdf (accessed on 8 October 2021).
4. Bartłomiejczyk, M.; Kołacz, R. The reduction of auxiliaries power demand: The challenge for electromobility in public transportation. *J. Clean. Prod.* **2020**, *252*, 119776. [CrossRef]
5. Oi, H.; Tabata, K.; Naka, Y.; Tochihara, Y. Effects of Regional Heating by Heated Seat in Vehicles on Thermal Sensation at 15 °C. *J. Hum.-Environ. Syst.* **2012**, *14*, 31–39. [CrossRef]
6. Evtimov, I.; Ivanov, R.; Sapundjiev, M. Energy consumption of auxiliary systems of electric cars. *MATEC Web Conf.* **2017**, *133*, 06002. [CrossRef]
7. Simion, M.; Socaciu, L.; Unguresan, P. Factors which influence the thermal comfort inside of vehicles. *Energy Procedia* **2016**, *85*, 472–480. [CrossRef]
8. Lajunen, A.; Yang, Y.; Emadi, A. Review of Cabin Thermal Management for Electrified Passenger Vehicles. *IEEE Trans. Veh. Technol.* **2020**, *69*, 6025–6040. [CrossRef]
9. Zhang, Z.; Wang, D.; Zhang, C.; Chen, J. Electric vehicle range extension strategies based on improved AC system in cold climate–A review. *Int. J. Refrig.* **2018**, *88*, 141–150. [CrossRef]
10. Kang, B.H.; Lee, H.J. A review of recent research on automotive HVAC systems for EVs. *Int. J. Air-Cond. Refrig.* **2017**, *25*, 1730003. [CrossRef]
11. Marshall, G.J.; Mahony, C.P.; Rhodes, M.J.; Daniewicz, S.R.; Tsolas, N.; Thompson, S.M. Thermal management of vehicle cabins, external surfaces, and onboard electronics: An overview. *Engineering* **2019**, *5*, 954–969. [CrossRef]
12. de Lieto Vollaro, R. Indoor climate analysis for urban mobility buses: A CFD model for the evaluation of thermal comfort. *Int. J. Environ. Prot. Policy* **2013**, *1*, 1–8. [CrossRef]
13. Bauml, T.; Dvorak, D.; Frohner, A.; Simic, D. Simulation and measurement of an energy efficient infrared radiation heating of a full electric vehicle. In Proceedings of the 2014 IEEE Vehicle Power and Propulsion Conference (VPPC), Coimbra, Portugal, 27–30 October 2014; pp. 1–6.
14. Collins, D.; Rednic, R.; Thake, C.D. Infrared heating as an adjunct to achieve vehicle occupant thermal comfort. *Extrem. Physiol. Med.* **2015**, *4* (Suppl. S1), A82. [CrossRef]
15. Dreißigacker, V. Solid Media Thermal Energy Storage System for Heating Electric Vehicles: Advanced Concept for Highest Thermal Storage Densities. *Appl. Sci.* **2020**, *10*, 8027. [CrossRef]
16. Jeffers, M.A.; Chaney, L.; Rugh, J.P. Climate control load reduction strategies for electric drive vehicles in cold weather. *SAE Int. J. Passeng. Cars-Mech. Syst.* **2016**, *9*, 75–82. [CrossRef]
17. Sahraei, H. Interior Climate U-Value Calculation and Optimization for Electric Buses at Volvo Buses. Master's Thesis, Department of Mechanics and Maritime Sciences, Chalmers University of Technology Gothenburg, Gothenburg, Sweden, 2020. Available online: https://odr.chalmers.se/bitstream/20.500.12380/300921/1/2020-39%20Hamidreza%20Sahraei.pdf (accessed on 9 December 2021).
18. Tanyeri, N.; Başlamişli, Ç. Prediction of the annual heat load of an articulated electric urban bus. *Isı Bilimi Tek. Derg.* **2020**, *40*, 27–36.
19. Torregrosa-Jaime, B.; Bjurling, F.; Corberan, J.M.; Di Sciullo, F.; Paya, J. Transient thermal model of a vehicle's cabin validated under variable ambient conditions. *Appl. Therm. Eng.* **2015**, *75*, 45–53. [CrossRef]
20. Pedersen, C.O.; Fisher, D.E.; Liesen, R.J. Development of a Heat Balance Procedure for Calculating Cooling Loads. *ASHRAE Trans.* **1997**, *103 Pt 2*, 459–468.
21. Göhlich, D.; Fay, T.-A.; Jefferies, D.; Lauth, E.; Kunith, A.; Zhang, X. Design of urban electric bus systems. *Des. Sci.* **2018**, *4*, e15. [CrossRef]
22. Chiriac, G.; Lucache, D.D.; Nituca, C.; Gabor, G. Aspects regarding the heating of electric buses. In Proceedings of the 13th International Conference on Electromechanical and Energy Systems (SIELMEN), Iasi, Romania, 7–8 October 2021.
23. Nițucă, C.; Chiriac, G.; Gabor, G.; Nucă, I.; Cazac, V.; Burduniuc, M. Geometry Design and Analysis of an Electric Bus for the Interior Thermal Modelling. *J. Energy Technol.* **2021**, in press.
24. Fayazbakhsh, M.A.; Bahrami, M. *Comprehensive Modeling of Vehicle Air Conditioning Loads Using Heat Balance Method*; Technical Paper 2013-01-1507; SAE International: Warrendale, PA, USA, 2013.
25. Yildirim, K.-E.; Finkenrath, M.; Gökoglu, M.; Seidel, F. Monitoring the Fresh-Air Flow Rate for Energy-Efficient Bus Ventilation. In *Energy and Thermal Management, Air Conditioning, Waste Heat Recovery*; Junior, C., Jänsch, D., Dingel, O., Eds.; Springer International Publishing: Cham, Switzerland, 2017; pp. 147–156.

26. National Meteorological Administration of Romania. Available online: https://www.meteoromania.ro/clim/caracterizare-lunara/index.html (accessed on 29 October 2021).
27. Balan, M. Energii Regenerabile. Ed UT PRES. 2007. Available online: http://www.termo.utcluj.ro/regenerabile (accessed on 9 December 2021). (In Romanian).
28. Pirouz, B.; Mazzeo, D.; Palermo, S.A.; Naghib, S.N.; Turco, M.; Piro, P. CFD Investigation of Vehicle's Ventilation Systems and Analysis of ACH in Typical Airplanes, Cars, and Buses. *Sustainability* **2021**, *13*, 6799. [CrossRef]
29. Gis, M.; Wiśniowski, P.; Bednarski, M. Efficiency of electric vehicle interior heating systems at low ambient temperatures. *Open Eng.* **2021**, *11*, 499–507. [CrossRef]
30. Bejan, A.; Kraus, A.D. (Eds.) *Heat Transfer Handbook*; John Wiley & Sons: Hoboken, NJ, USA, 2003; Volume 3.
31. Fang, W.-Z.; Gou, J.-J.; Chen, L.; Tao, W.-Q. A multi-block lattice Boltzmann method for the thermal contact resistance at the interface of two solids. *Appl. Therm. Eng.* **2018**, *138*, 122–132. [CrossRef]
32. Wang, A.; Zhao, J. Review of prediction for thermal contact resistance. *Sci. China Technol. Sci.* **2010**, *53*, 1798–1808. [CrossRef]
33. Haghighat, F.; Rao, J.; Fazio, P. The influence of turbulent wind on air change rates—A modelling approach. *Build. Environ.* **1991**, *26*, 95–109. [CrossRef]
34. Vaswani Reyes, R.H. Optimization of the Heating System of a Bus Cabin: A Numerical Approach through OpenFOAM. Master's Thesis, Politecnico di Torino, Torino, Italy, 2020. Available online: https://webthesis.biblio.polito.it/15401/ (accessed on 8 December 2021).
35. Henning, M.; Smyth, A.; Thomas, A. *An Analysis of the Association between Changes in Ambient Temperature, Fuel Economy, and Vehicle Range for Battery Electric and Fuel Cell Electric Buses*. Technical Report; Urban Publications. 0 1 2 3 1630. 2019. Available online: https://engagedscholarship.csuohio.edu/urban_facpub/1630 (accessed on 9 December 2021).

SIMULATED THERMAL RESPONSE OF A BATTERY PACK USED BY ELECTRIC TWO-WHEELERS

by

Costica NITUCA*[*], *Alin DRAGOMIR,
Georgel GABOR, and Gabriel CHIRIAC

"Gheorghe Asachi" Technical University of Iasi,
Faculty of Electrical Engineering, Iasi, Romania

Original scientific paper
https://doi.org/10.2298/TSCI250724194N

This article presents a theoretical investigation into the thermal behavior of a pack of 18650 lithium-ion commercial batteries used for the propulsion of two-wheeled electric vehicles. In the first part, we highlight the theoretical aspects that describe the energy balance of a cylindrical lithium-ion battery based on the law of conservation of energy. The research aims to emphasize the effect of temperature on the technical performance of batteries. Next, using the COMSOL Multiphysics 6.2 software package, "heat transfer in solids and fluids", the thermal behavior was modeled for a single cylindrical battery cell, type 18650 lithium-ion, 3.7 V, 2200 mAh, respectively a battery pack with the same type of cells, 18650 lithium-ion. The battery pack was made in the structure of 3 cells in series and 7 cells in parallel (3S7P). The distribution of the temperature generated inside the battery cell, respectively in the structure of the 3S7P battery pack, was taken into account, at a charge/discharge rate considered extreme of 5.5C. In order to ensure a quality mesh in the process of simulating the geometry of the 3S7P battery pack, a mesh convergence study was also considered through progressively finer runs until the temperature of the battery pack did not change significantly with the subsequent refinement of the mesh. Simulations of thermal behavior were conducted while accounting for thermal conductivity, density, heat capacity, and heat source in the batteries. The battery pack was thermally loaded to measure temperatures inside the protective case, starting from an initial ambient temperature. The results obtained demonstrate several characteristics that can enhance the technical performance of battery packs used in electric two-wheeled vehicles.

Keywords: *simulation, cylindrical lithium-ion batteries,*
thermal stress, energy transfer

Introduction

Climate change, the depletion of fossil fuel reserves, but also the increase in pollution are a vital problem at a global level [1]. The European Union’s policies on GHG emissions aim for climate neutrality by 2050, and their reduction should reach at least 55% by 2030 compared to 1990 levels [2]. Achieving climate change mitigation goals would require changes in societal behaviors, but also in technologies that would phase out the use of polluting energy resources. In this regard, finding new sources of green energy, but especially technologies for storing this energy, is a global concern both among researchers and manufacturers of equipment and technical devices specific to the automotive industry. In this direction, numerous energy storage

---

[*] Corresponding author, e-mail: costica.nituca@academic.tuiasi.ro

technologies (mechanical, electrochemical, thermal or chemical) [3] are known, with different energy capacities and charge/discharge times [3, 4], but also with a certain impact on the environment [5-8], thus resulting in several types of storage devices: flywheels, compressed air, hydro-pumping, batteries (lead-acid, lithium-ion), flow battery, double-layer capacitor, superconducting magnets, hydrogen and molten salts [9, 3].

Among the energy storage technologies that are gaining popularity, have relatively low costs, high autonomy, and also technological advances in implementation, the most promising seem to be electrochemical storage technologies. In this category of technologies, we find batteries with lead acid, nickel, sodium-sulfur, lithium batteries, and flow batteries [10]. Energy stored in batteries finds its availability in commercial, residential, agricultural, and industrial spaces. According to the report [11], batteries will be key to achieving the energy targets agreed by nearly 200 countries at the COP28 climate change conference in Dubai (the 28th United Nations Climate Change Conference), in particular tripling renewable energy capacity by 2030, doubling the pace of energy efficiency improvement and transitioning away from fossil fuels [12]. Due to the potential of energy storage systems, researchers' efforts are focused on identifying typologies, technical characteristics, limitations, comparisons, evaluations, challenges, but also applications aimed at using the best energy storage technologies [3].

One sector that seems to be using the potential of electric batteries is electric vehicles. As a solution dependence on fossil fuels, the concept of *sustainable transport* is identified [13]. This can be achieved, as the use of electric vehicles in the transport sector would significantly reduce greenhouse gas emissions, contribute to an improvement in air quality [14], but would also eliminate some of the noise pollution produced by vehicles with internal combustion engines [15-17], in a word, they would be environmentally friendly. Moreover, compared to the fossil fuel-based propulsion energy source, in the case of electric vehicles (light, medium or heavy), electric batteries can be recycled, leading to an alleviation of environmental concerns [6].

If we consider the use of batteries for electric vehicles, then different requirements are imposed, which are given by the specific energy, power density, rated voltage, self-discharge speed, charging time, life cycle, operational safety, working temperature, cost price*, etc.* With a higher energy density (620 kWh/m^3), lithium-ion batteries are by far the high-capacity technologies for an improved implementation of energy storage in the built environment, even if the price is high [3]. However, batteries still present a number of obstacles to their introduction on the widest possible scale. These can be identified in the underdeveloped technology of electric batteries [17], the limited autonomy, the charging time, but also the expensive initial costs [18]. Extensive research is being conducted to tackle the challenges facing battery technology head-on. This research is driving the development of advanced technologies such as fast charging, optimization strategies [8, 19] intelligent charging systems [20, 21], and significant improvements in energy efficiency. Additionally, it addresses the practical limitations of wireless charging, modern algorithms for battery condition assessment, safety measures for high-energy batteries, and their environmental impact [7, 8]. Moreover, we have made substantial progress in voltage balancing of battery cells within battery management systems, employing various methods to ensure effective balancing during both the charging and proper discharge processes of battery packs [22, 23]. These efforts aim to improve the usability, reliability and general acceptance of different types of electric vehicles [24].

In this study, aspects regarding the thermal behavior of the commercial lithium-ion cylindrical battery type 18650, are treated [25]. The battery pack subjected to simulation contains 21 cylindrical cells, 18650, in 3S7P connection. The electrical connections between the cells of the battery pack were made with connectors made of zinc metal sheet, with a thickness of

0.5 mm. The length of the electrical connector for both series and parallel connections is 123 mm. The width of the series connector is 8 mm, and that of the parallel connector is 27 mm. The parallel connector element has six square cutouts with sides of 11 mm along its length. Also, the battery pack is inserted into a rectangular protective housing made of thermoplastic polymer (acrylonitrile butadiene styrene).

In the first part, an analysis of the role, importance, and specific problems of batteries used in the automotive is presented, with a presentation of an analytical model on heat transfer for cylindrical lithium-ion batteries. The thermal response of the battery pack is presented, emphasizing the action of temperature on their performance. In the final part, a thermal modelling and simulation of the cylindrical lithium-ion battery using the COMSOL Multiphysics software package is presented, aiming at the results obtained to be interpreted in order to identify some points of optimization from a technical point of view of the battery packs used in the propulsion of 2-wheeled electric vehicles.

Analytical model for heat transfer

The thermal behavior of batteries is generally governed by three fundamental equations: the heat generation equation, the energy equilibrium equation, and the boundary condition equation [26, 27]. Based on these equations, there are a multitude of models that have proposed to study the thermal battery cells characteristics [27]. The concentrated capacitance model was taken into account in the analytical solution method for heat transfer in the battery cell [28]. The equation describing the energy balance of a cylindrical cell for a lithium-ion battery can be developed considering the law of conservation of energy. Under these conditions, the relationship of energy balance can be written [28-30]:

$$\rho C_p \frac{\mathrm{d}T}{\mathrm{d}t} = \frac{1}{r}\frac{\partial}{\partial r}\left(k_r r \frac{\partial T}{\partial r}\right) + \frac{1}{r^2}\frac{\partial}{\partial \varphi}\left(k_a \frac{\partial T}{\partial \varphi}\right) + \frac{\partial}{\partial z}\left(k_z \frac{\partial T}{\partial z}\right) + \dot{Q} \tag{1}$$

where it is observed that the term on the left side represents the energy stored in the cell, while the term on the right side shows the 3-D conduction of heat, the expression of the rate of volumetric heat generation. Taking into account the constructive structure of a cylindrical cell in a lithium-ion battery, each cell of a battery module can be considered as a homogeneous body with effective thermophysical properties [28, 31]. In view of these considerations, the actual value of the density and thermal capacity of a single cell can be written [28]:

$$\rho C_p = \frac{\sum_i \rho_i C_{p,i} V_i}{\sum_i V_i} \tag{2}$$

As the active material of the lithium-ion battery consists of one or more battery cells whose layers are spirally wound in a cylinder, the thermal conductivities are hypothesized to be thermally anisotropic, exhibiting a higher thermal conductivity along the battery sheets, in the direction of the length of the cylinder, compared to the normal direction of the sheets, *i.e.* the radial one [32]. Under these conditions, the thermal conductivity in the radial direction [28], [31-33]:

$$k_r = \frac{\sum_i L_i}{\sum_i \frac{L_i}{k_{T,i}}} \tag{3}$$

and the thermal conductivity in the direction of the length of the cylinder is given by the relationship:

$$k_a = \frac{\sum_i L_i k_{T,i}}{\sum_i L_i} \tag{4}$$

Similarly, the density and specific heat capacity of the active material can be determined [33]:

$$\rho = \frac{\sum_i L_i \rho_i}{\sum_i L_i} \tag{5}$$

$$C_p = \frac{\sum_i L_i C_{p,i}}{\sum_i L_i} \tag{6}$$

Thermal modelling of concentrated capacitance is an approach to transient conduction that assumes that the temperature of a solid is spatially uniform and is only a function of time, t. This implies that there are negligible temperature gradients in a solid and that the thermal conductivity, k, is infinite. In reality, this aspect is completely different, in the sense that it can only be approximated if the thermal resistance to conduction inside the solid is significantly lower than the thermal resistance to convection between the solid and the environment [27, 28]:

$$\frac{L_c}{k} \ll \frac{1}{h} \tag{7}$$

In the given case, the characteristic length, h, is the ratio of the volume to the surface area of the solid. In addition, eq. (7) formulates the dimensionless number Biot as in [26-28]:

$$\mathrm{Bi} = \frac{hL_c}{k} \ll 1 \tag{8}$$

The ratio of heat transfer resistance within and to the surface of the battery cell is represented as Biot number, and it must be significantly less than 1 to be applied in a concentrated capacitance model. This is because when it is less than 0.1, the transient heat pattern error is less than 5%. When taking into account the parametric values of the current scenario, the number is also less than 0.1 [28]. If the Biot number is higher than 1, it means that there would be temperature gradients inside the body [26]. Under these conditions, there is the alternative of applying the concentrated capacity model for the heat transfer of the lithium-ion battery cell by simplifying the equation of the global energy balance:

$$\rho C_p \frac{\mathrm{d}T}{\mathrm{d}t} = hA\left(T - T_{\mathrm{amb}}\right) + \dot{Q} \tag{9}$$

The thermal balance for the recovery of the energy stored in battery packs used in the propulsion of 2-wheeled electric vehicles is a key to verifying their technical performance. From this mathematical analysis it is possible to identify the direction of optimization of the use of electricity stored in batteries.

In eq. (9), $\dot{Q}$ [W] signifies the battery volumetric heat production rate. There are several heat sources in a battery, mainly irreversible and reversible processes, that occur during its charging/discharging process. Irreversible heat is primarily due to ohmic resistance from the flow of electrons and ions and polarization resistance from activation and concentration changes, while reversible heat comes from electrochemical reactions and entropy changes at the cathode and electrode of the battery.

The total heat produced by the battery can be written as [30, 34]:

$$Q = Q_{\text{irr}} + Q_{\text{rev}} = I\left(V - U_{\text{ouc}}\right) + IT\frac{\partial U_{\text{ouc}}}{\partial T} \tag{10}$$

where Q is the heat of reaction, Q_{rev} – the reversible heat and Q_{irr} – the irreversible heat, I – the discharge current, V – the battery potential, T – the battery temperature, U_{ouc} – the open circuit potential, and $\partial U_{\text{ouc}}/\partial T$ – the entropic heat coefficient.

Modelling and thermal simulation of cylindrical lithium-ion battery pack

The causes that determine the heating of electric batteries in the charging or discharging process are given by changes in enthalpy, resistive heating inside the cell, respectively electrochemical polarization. The change in enthalpy combined with the electrochemical reactions that occur inside the battery is the main cause of the increase in battery temperature [28, 30]. Following the analysis of the thermal balance equation, ohmic heat is identified as representing the energy loss caused by transport resistance in solid and electrolytic phases, while electrochemical polarization can be regarded as the deviation between the open circuit potential of the cell and the operating potential [28].

The dependence of battery performance on temperature

The lithium-ion batteries work optimally within the designed parameters only over a well-established temperature range. Thus, [35] it mentions that the temperature range is usually intended to be between 25 °C and 35 °C, as temperatures that are too high or too low can reduce the efficiency of the battery. In [36] it is specified that the reliable operating temperatures of lithium-ion batteries are in the range of –20 °C to 55 °C during discharge and 0 °C to –45 °C during charging. Typically, lithium-ion batteries work optimally in the temperature range of 20 °C to 45 °C [37].

Results of the of the cylindrical lithium-ion battery pack thermal simulation

For this study, the commercial cylindrical lithium-ion battery, type 18650, minimum capacity 1950 mAh, maximum capacity 2200 mAh, nominal voltage 3.7 V, maximum charging voltage 4.2 V, dimensions 18 mm × 65 mm, manufactured outside the EU. The 3S7P battery pack is assembled by the authors as part of this research.

Table 1 presents the parameters of the 18560 cylindrical lithium-ion battery used for thermal simulation [30, 38].

The specific sizes and values of the cylindrical lithium-ion battery used for modelling and simulating the thermal response, were used as input quantities for the COMSOL Multiphysics software environment, [38, 39].

The goal pursued by modelling and simulating the thermal response was to identify the way in which the temperature distribution is obtained, and to identify new solutions to obtain the heat dissipation. In order to simulate the distribution of the temperature generated inside a battery during the charging/discharging process, in a first step, the thermal behavior for a single battery was modeled. In this regard, ohmic heat, reaction heat, and polarization heat were considered.

Table 1. Parameters of 18560 cylindrical Li-ion battery used for thermal simulation [30, 38]

Parameter description	Value	Unit
Thickness of battery canister, d_{can}	0.25	[mm]
Battery radius, r_B	9	[mm]
Battery height, h_B	65	[mm]
Mandrel radius, r_m	2	[mm]
Length of negative electrode, l_{nE}	55	[μm]
Length of separator, l_s	30	[μm]
Length of positive electrode, l_{pE}	55	[μm]
Negative current collector thickness, d_{nCC}	7	[um]
Positive current collector thickness, d_{pCC}	10	[um]
Positive electrode thermal conductivity, kT_p	1.58	[$\text{Wm}^{-1}\text{K}^{-1}$]
Negative electrode thermal conductivity, kT_n	1.04	[$\text{Wm}^{-1}\text{K}^{-1}$]
Positive current collector thermal conductivity, kT_{pCC}	170	[$\text{Wm}^{-1}\text{K}^{-1}$]
Negative current collector thermal conductivity, kT_{nCC}	398	[$\text{Wm}^{-1}\text{K}^{-1}$]
Separator thermal conductivity, kT_s	0.344	[$\text{Wm}^{-1}\text{K}^{-1}$]
Positive electrode density, Rho_p	2328.5	[kg/m3]
Negative electrode density, Rho_n	1347.33	[kg/m3]
Positive current collector density, Rho_{pCC}	2770	[kgm^{-3}]
Negative current collector density, Rho_{nCC}	8933	[kgm^{-3}]
Separator density, Rho_s	1008.98	[kgm^{-3}]
Positive electrode heat capacity, C_{pp}	1269.21	[$\text{Jkg}^{-1}\text{K}^{-1}$]
Negative electrode heat capacity, C_{pn}	1437.4	[$\text{Jkg}^{-1}\text{K}^{-1}$]
Positive current collector heat capacity, Cp_{pCC}	875	[$\text{Jkg}^{-1}\text{K}^{-1}$]
Negative current collector heat capacity, Cp_{nCC}	385	[$\text{Jkg}^{-1}\text{K}^{-1}$]
Separator heat capacity, Cp_s	1978.16	[$\text{Jkg}^{-1}\text{K}^{-1}$]
Cycle time, t_c	600	[second]
Inlet temperature, T_{in}	298.15	[K]
Cell capacity, QB	1.258	[Ah]
Ohmic overpotential at 1C, $\zeta 1C$	4.5	[mV]
Dimensionless charge exchange current, J_0	0.85	
Diffusion time constant, τ	1000	[second]
Initial state-of-charge, $SOCi$	0.2	
Applied current, I_{app}	2.5	[A]
The rate of discharge/charge, Cr	1	
Time of discharge, t_{d}	3600/Cr	[second]

The simulation model consisted of a 1-D model (which models the chemistry of the battery cell) and a 3-D model (modelling the temperature in the battery), which were coupled in the simulation process. The cell model was created using the Lumped Battery interface [37], for which the battery capacity and its initial state of charge were used. To identify the place of heat generation inside the cell, the 1-D model was used, and the 3-D model was used to model the temperature profile of the battery cell [38].

The simulations performed in the paper [38], present the thermal behavior of the 18650 cylindrical battery at a charge/discharge current with a rate of 7.5C, where at t = 1220 seconds, the temperature differences present the values: $\Delta T_{\max}$ = 23.775 K, ΔT_{mean} = 22.917 K, $\Delta T_{\min}$ = 22.039 K.

For our research, we are interested in the thermal behavior of both the 18650 cylindrical battery and the 3S7P package, but at a charge/discharge current with a rate of 5.5C. This reasoning takes into account the fact that, in general, light two-wheeled vehicles have a less severe operating regime, as they are used in cities on routes without large slopes. In this context, we will choose the peak temperature value that occurs at t = 1220 seconds, according to the research in [38], respectively an intermediate, random variant of t = 478.8 seconds.

In order to have a comparative image of the temperature evolution inside the cylindrical lithium-ion battery, at different times of the charging process, t_1 = 478.8 seconds and t_2 = 1220 seconds, respectively, are considered. Figure 1(a) shows the simulation of the temperature at t_1 = 478.8 seconds, where it is observed that the maximum temperature in the center of the battery, which is in the active material, has a value of 312 K, while on the outside of it, the temperature reaches the minimum of 311 K. In fig. 1(b), at t_2= 1220 seconds, the simulation of the temperature inside the battery is presented, where it is observed that the maximum temperature value in the center of the battery is 322 K (while the minimum temperature is 320 K).

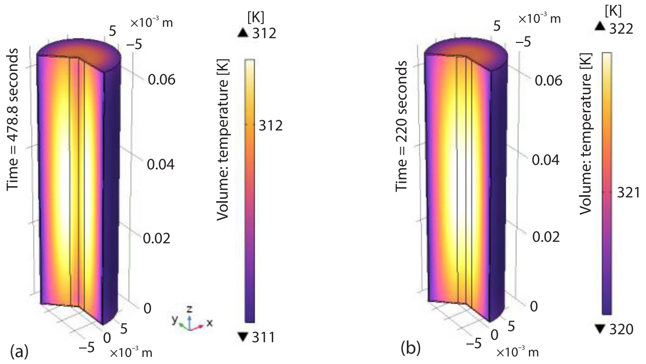

**Figure 1. Temperature distribution in the battery at;
(a) t_1 = 478.8 seconds and (b) t_2 = 1220 seconds**

In the next step, a battery array consisting of 3 cells linked in series with 7 cells linked in parallel (3S7P) is considered, thus forming a battery pack that will be subjected to this study. For the simulation of the thermal behavior of the battery pack 3S7P, the thermal conductivity, density, heat capacity and heat source in the battery are configured keeping the same values as in the case of thermal modelling of a cylindrical lithium-ion battery in the 2-D/3-D model, from the previous step [38, 39].

The 3S7P battery array features a straight stack/pack with series and parallel electrical links made of metal strips at the top and bottom, respectively, according to the 3S7P configuration. These metal bonds are included in the heat transfer model. The initial temperature of the battery is considered to be 298.15 K.

Figure 2(a) shows the geometric structure of the battery pack to be modeled, and fig. 2(b), a tetrahedral lattice representation resulting from the addition and construction of a tetrahedral node specific to cylindrical lithium-ion batteries. Among the characteristic of this tetrahedral networks we can mention: mesh vertices – 12629 (value); tetrahedral – 29092 (value); prisms – 10620 (value), triangles – 17808 (value).

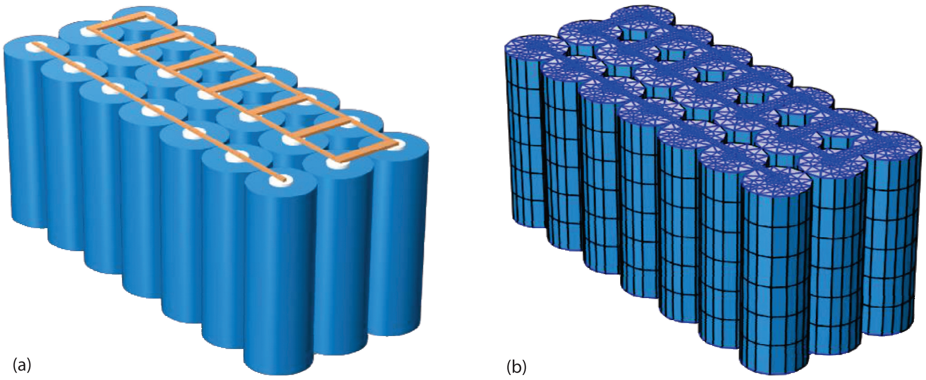

Figure 2. Geometric structure of the 3S7P battery pack; (a) geometry display and (b) geometry mesh

Figure 3 shows the simulation results regarding the thermal distribution of the 3S7P battery pack, at t = 523.62 seconds (0.14545 hours). The period taken for analysis is limited by the fact that the proposed system is designed to load and unload all the time. Or, either to discharge almost completely, after that, a charge. The thermal simulation does not aim to achieve a permanent regime of the temperature of the battery pack. It proposes to analyze its thermal behavior when a critical point is reached. Depending on the charge/discharge rate, C, of the electricity stored in them, the temperature rises more slowly or increases very quickly, depending on this parameter. The higher the charge/discharge cycle, C, the higher the electricity consumption in the batteries; therefore, it discharges faster over time, and the temperature of the pack increases a lot.

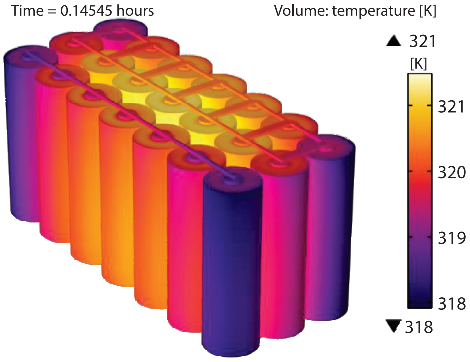

Figure 3. Thermal distribution in the 3S7P battery pack

In the case of the proposed simulation, a charge/discharge rate of 5.5C was considered, where it is observed that in its center, the maximum temperature is 321 K, and towards the outer parts of the battery pack, the minimum temperature is 318 K (the temperature difference between the inner and outer parts of the battery pack is 4 K). At a first approximation, we can consider that the cells in the middle of the battery pack become vulnerable to their thermal packaging. These are the elements that require thermal optimization in operation, which can be achieved through forced cooling or natural air cooling, but which would imply an increase in the dimensions of the battery pack. Or a larger battery pack positioning space, which is provided with slits to direct air currents in the case of natural cooling, or forced air cooling devices such as fans.

Figure 4 shows the graph of the maximum and average temperatures of the battery pack at t = 523.62 seconds (0.14545 hours) and charge/discharge cycle 5.5C, where it is observed that the initial temperature is 298.15 K (25 °C), the maximum temperature is 321.48 K (48.33 °C), and the average temperature is 320.39 K (47.24 °C).

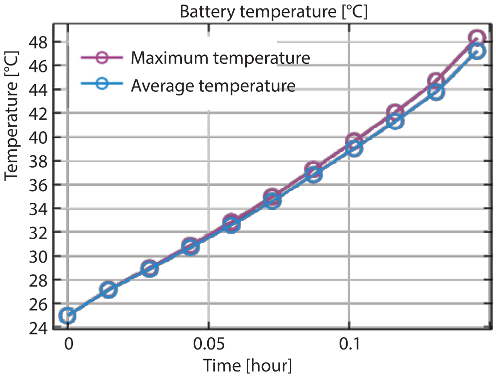

Figure 4. Battery pack temperature chart at charge/discharge cycles with the value of 5.5C

For use, the battery pack can be placed in a plastic container (housing) with the dimensions: 150 mm long, 65 mm wide, 95 mm high, and 1.5 mm thick. A space of 1 mm has been provided between the cells of the battery matrix, respectively cells and the casing to allow the internal circulation of air currents. The inside of the container is filled with air, and the battery cells are cooled by convection, but also by thermal radiation the outside of the case.

Figure 5 shows the thermal distribution simulation of the 3S7P battery pack, at t = 523.62 seconds (0.14545 hours), at a rate of 5.5C, which was inserted into the protective housing. It can be seen that under the same conditions as the simulation in fig. 3, the maximum temperature increases by 1 K, reaching 321 K.

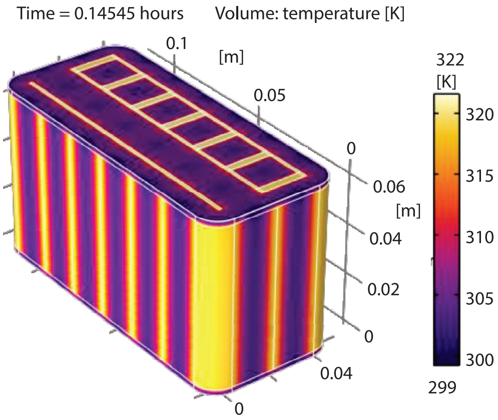

Figure 5. Thermal distribution of the 3S7P battery pack inserted into the protective case

Since the heat released by the cells of the battery pack is initially concentrated in the central part of the pack, it is found that, with time, this heat is taken up by the other cells in the battery array. Moreover, the cells that are close to the casing radiate heat to the casing material. The dark spaces (blue on fig. 5) represent the air spaces between the cells, respectively, the cells, and the protective case. The temperature of these has a minimum value of 299 K. The simulated model obtained highlights the temperature distribution over the entire pack of batteries that make up the block used to drive electric two-wheeled vehicles. The thermal analysis highlights the fact that stacking the batteries in compact blocks co-ordinates the temperature that has risen in the center of the created block. This temperature distribution indicates that the operating temperature of the batteries can be lowered if solutions to lower the temperature are identified in the middle of the created block.

Due to the standard dimensions imposed by the use of battery packs specific to two-wheeled electric vehicles, it is not possible to intervene in increasing the volume inside the case. In this context, the placement of the batteries in the case raises the operating temperature, which leads to limiting their performance. From the simulated models, solutions were identified to reduce the operating temperature through external forced cooling actions, which involved additional energy consumption. From the simulations performed, it can be seen that, compared to the cells located towards the end of the package (3S7P), the cells positioned in its center are the most vulnerable to excess heat during the loading/discharging process. Thus, in the center of the package results a temperature of 321 K results, while on its corners, the temperature reaches 318 K. When the battery pack is inserted into the protective case, all batteries become vulnerable, including those in the corners of the case. Already after a time of 0.14545 hours, their temperature reaches 322 K. However, it is noted that there is also a minimum temperature of 299 K, which represents the temperature in the air space between the cells and cells and the protective case.

Conclusions

For the battery cells to operate at the prescribed temperatures, it is necessary to identify the optimal operating temperatures of the battery pack (cells), to reduced excess temperatures, to prevent thermal evaporation, but also to ensure optimal charge/discharge cycles by balancing the charging voltage/current on each cell. It is also important to identify vulnerable cells, which, as observed from simulations, are found in the center of the battery pack, and to ensure a concentrated cooling process. Moreover, placing the batteries in closed protective housings causes the entire battery pack to overheat, as heat evacuation becomes very difficult. The simulations also result in a local heating of the protective case given by the batteries placed on its edge. This research aims to translate into an optimized physical model of battery pack used for the propulsion of electric 2-wheeled vehicles, which has a lower operating temperature than currently known models. Future research aims to validate the simulated models by developing an experimental stand that highlights the temperature distribution.

The COMSOL Multiphysics software offers capabilities for simulating and analyzing thermal processes, particularly in modelling thermoelectric effects. This includes assessing permissible currents and the thermal stresses induced by nominal currents. In battery packs, thermal stresses arise from the electrocaloric effect caused by the current flow. Consequently, it is recommended to monitor these stresses through simulation and to compare the numerical results with the maximum allowable temperature to validate them. A thorough understanding of the battery pack's design components and installation conditions allows for validated simulation results, facilitating the identification of practical solutions to optimize thermal losses.

Acknowledgment

This work was supported by a grant of the Ministry of Education and Research, CCCDI – UEFISCDI, project number PN-IV-PCB-RO-MD-2024-0264, within PNCDI IV.

Nomenclature

A – heat exchange area
Bi – the dimensionless number Biot
C – battery charge/discharge rate
C_p – specific heat capacity, [Jkg^{-}1K^{-1}]
h – heat transfer coefficient, [Wm^{-2}K^{-1}]
k – thermal material conductivity [Wm^{-1}K^{-1}]
$k_{T,i}$ – the thermal conductivities of the materials of which the battery layers are made, [Wm^{-1}K^{-1}]
k_a – thermal conductivity in the longitudinal direction, [Wm^{-1}K^{-1}]
k_r – thermal conductivity in the radial direction, [Wm^{-1}K^{-1}]
k_r, k_a, k_z – thermal conductivities of the battery cell in the x-, y- and z-directions, respectively, [Wm^{-1}K^{-1}]
L_c – characteristic length, [m]
L_i – the thicknesses of the different layers of the cell, [m]
$\dot{Q}$ – volumetric heat generation rate for the battery cell, [W]
r – battery cell radius, [m]
T – absolute temperature, [K]
T_amb– absolute temperature under ambient conditions, [K]
t – time, [s]
V_i – the volume of each component in the battery structure, [m^3]

Greek symbol

ρ – the density of the active material of the cell, [kgm^{-3}]

References

[1] Gwalwanshi, M., *et al*., A Review on Butanol Properties, Production and its Application in Internal Combustion Engines, *Materials Today: Proceedings*, *62* (2022), Part 12, pp. 6573-6577

[2] ***, Regulation (EU) 2021/1119 of the European Parliament and of the Council of 30 June 2021 Establishing the Framework for Achieving Climate Neutrality, 2021

[3] Elalfy, D. A., *et al*., Comprehensive Review of Energy Storage Systems Technologies, Objectives, Challenges, and Future Trends, *Energy Strategy Reviews*, *54* (2024), 101482

[4] Gur, T. M., Review of Electrical Energy Storage Technologies, Materials and Systems: Challenges and Prospects for Large-Scale Grid Storage, *Energy and Environmental Science*, *11* (2018), 10, pp. 2696-2767

[5] Sternberg, A., Bardow, A., Power-to-What – Environmental Assessment of Energy Storage Systems, *Energy and Environmental Science*, *8* (2015), 2, pp. 389-400

[6] Qiao, Q., *et al*., Electric Vehicle Recycling in China: Economic and Environmental Benefits, Resources, *Conservation and Recycling*, *140* (2019), Jan., pp. 45-53

[7] Waseem, M, *et al*., An Electric Vehicle Battery and Management Techniques: Comprehensive Review of Important Obstacles, New Advancements, and Recommendations, *Energy Storage and Saving*, *4* (2024), 1, pp. 83-108

[8] Madaram, V. G, *et al*., Advancement of Electric Vehicle Technologies, Classification of Charging Methodologies, and Optimization Strategies for Sustainable Development, *Heliyon*, *10* (2024), 20

[9] Babu, T. S., *et al*., A Comprehensive Review of Hybrid Energy Storage Systems: Converter Topologies, Control Strategies and Future Prospects, *IEEE Access*, *8* (2020), Aug., pp. 148702-148721

[10] Kampouris, K. P., *et al*., Energy Storage Systems Review and Case Study in the Residential Sector, *Proceedings*, IOP Conference Series: Earth and Environmental Science, IOP Publishing, Thessaloniki, Greece, 2020, Vol. 410, 1, 012033

[11] ***, International Energy Agency (IEA), Batteries and Secure Energy Transitions, World Energy Outlook Special Report, https://www.iea.org/reports/batteries-and-secure-energy-transitions, 2024

[12] ***, International Energy Agency IEA, CO_2 emissions from fuel combustion: Overview, global CO_2 emissions by sector, https://www.iea.org/reports/global-energy-review-2020/global-energy-and-co2-emissions-in-2020, 2020

[13] Song, M., *et al*., Charging Station Location Problem for Maximizing the Space-Time-Electricity Accessibility: A Lagrangian Relaxation-Based Decomposition Scheme, *Expert Systems with Applications*, *22* (2023), 119801

[14] Veza, I., *et al*., Electric Vehicle (EV) and Driving Towards Sustainability: Comparison Between EV, HEV, PHEV, and ICE Vehicles to Achieve Net Zero Emissions by 2050 from EV, *Alexandria Engineering Journal*, *82* (2023), Oct., pp. 459-467

[15] Granacher, J., *et al*., Overcoming Decision Paralysis. A Digital Twin for Decision Making in Energy System Design, *Applied Energy*, *306* (2022), 117954

[16] Ibrahim, M., *et al*., Overview on Digital Twin for Autonomous Electrical Vehicles Propulsion Drive System, *Sustainability*, *14* (2022), 601

[17] Alanazi, F., Electric Vehicles: Benefits, Challenges, and Potential Solutions for Widespread Adaptation, *Applied Sciences*, *13* (2023), 6016

[18] Capuder, T., *et al*., Review of Challenges and Assessment of Electric Vehicles Integration Policy Goals: Integrated Risk Analysis Approach, *International Journal of Electrical Power & Energy Systems*, *119* (2020), 105894

[19] Till, G., *et al*., Fast Charging Infrastructure for Electric Vehicles: Today's Situation and Future Needs, Transportation Research Part D: *Transport and Environment, 62* (2018), July, pp. 314-329

[20] Will, C., Schuller, A., Understanding user Acceptance Factors of Electric Vehicle Smart Charging, *Ransportation Research Part C: Emerging Technologies*, *71* (2016), Oct., pp. 198-214

[21] Zhong, Z., *et al*., Rethinking Electric Vehicle Smart Charging and Greenhouse Gas Emissions: Renewable Energy Growth, Fuel Switching, and Efficiency Improvement, *Applied Energy*, *361* (2024), 122904

[22] Lelie, M., *et al*., Battery Management System Hardware Concepts: An Overview, *Applied Sciences*, *8* (2018), 534

[23] Khan, N., *et al*., A Critical Review of Battery Cell Balancing Techniques, Optimal Design, Converter Topologies, and Performance Evaluation for Optimizing Storage System in Electric Vehicles, *Energy Reports*, *11* (2024), June, pp. 4999-5032

[24] Jiang, B. H., *et al*., A Review of Modern Electric Vehicle Innovations for Energy Transition, *Energies*, *17* (2024), 2906

[25] ***, Data Sheet 18650 Battery, Honcell, Rechargeable Lithium-ion Cylindrical Battery Bare Cell, Shenzhen Honcel Energy Co., China

[26] Shabani, B., Biju, M., Theoretical Modelling Methods for Thermal Management of Batteries, *Energies*, *8* (2015), Sept., pp. 10153-10177

[27] Arumugam, A., *et al.*, Lumped Capacitance Thermal Modelling Approaches for Different Cylindrical Batteries, *Int. Journal of Energy Production and Management*, 8 (2023), 4, pp. 201-210

[28] Samarasinghe, H. D. T. G., *et al*., Thermal and Heat Transfer Modelling of Lithium – Ion Battery Module during the Discharge Cycle, *Comsol Conference Paper, London*, *1* (2020), 2, pp. 1-6

[29] Chen, H., *et al*., A Simplified Mathematical Model for Heating-Induced Thermal Runaway of Lithium-Ion Batteries, *Journal of the Electrochemical Society*, *168* (2021), 010502

[30] Same, J. S., *et a*l., Effect of Thermal Parameters on Behaviour of a Lithium-Ion Battery: Simulation Study, *International Journal of Electrochemical Science*, *17* (2022), 220951

[31] Xiao, M., Choe, S. Y., Theoretical and Experimental Analysis of Heat Generations of a Pouch Type $LiMn_2O_4$/Carbon High Power Li-Polymer Battery, *Journal of Power Sources*, *241* (2013), Nov., pp. 46-55

[32] Chen, S. C., *et al*., Thermal Analysis of Spirally Wound Lithium Batteries, *Journal of the Electro-Chemical* Society, *153* (2006), 4, pp. A637*A648

[33] ***, COMSOL Multiphysics, Batteries and Fuel Cells Module, Application Library Manual, 1998-2016 COMSOL, Version: COMSOL 5.3, 2016

[34] Potnuru, S., *et al*., Computational Modelling on Lithium-Ion Battery Pack Forced Convection Cooling, in: *Talpa Sai, P. H. V. S., Intelligent Manufacturing and Energy Sustainability*, ICIMES 2023, Smart Innovation, Systems and Technologies, vol 372. Springer, Singapore, 2023

[35] Wang, Q., *et al*., A Critical Review of Thermal Management Models and Solutions of Lithium-Ion Batteries for the Development of Pure Electric Vehicles, *Renewable and Sustainable Energy Reviews*, *64* (2016), Oct., pp. 106-128

[36] Mishra, S., *et al*., A Comprehensive Review on Developments in Electric Vehicle Charging Station Infrastructure and Present Scenario of India, *Sustainability*, *13* (2021), 4, pp. 1-20

[37] Li, H., *et al.*, Investigating the Impact of Battery Arrangements on Thermal Management Performance of Lithium-Ion Battery Pack Design, *Advances in Mechanical Engineering*, *16* (2024), 9, pp. 1-15

[38] ***, COMSOL Multiphysics 6.2., Thermal Modelling of a Cylindrical Lithium-Ion Battery in 2D, Application ID: 10221

[39] ***, COMSOL Multiphysics 6.2., Thermal Modelling of a Cylindrical Lithium-Ion Battery in 3D, Application ID: 10224

Paper submitted: July 24, 2025
Paper revised: September 19, 2025
Paper accepted: September 25, 2025

Simulating Thermal Phenomena Occurring in Fast Electric Fuses Used for Power Electronic Protection

Patrichi Ștefan, Nițucă Costică, Chiriac Gabriel, Pleșca Adrian
"Gheorghe Asachi" Technical University of Iasi
Faculty of Electrical Engineering
Iasi, Romania
patrichi_stefan@yahoo.com

Zhiyuan Liu, Yingsan Geng
Xi'an Jiaotong University
Xi'an, China
Liuzy@mail.xjtu.edu.cn

Abstract—**This article presents a thermal analysis of fast electric fuses used for power electronic protection. By comparison of different quenching media to the quartz sand, there are presented recordings of voltage and current waveforms when the circuit breaks down due to the ultra-fast fuses with a rated current of 100 A. Considering the analogy between the electrical and thermal, similarly to the power semiconductors, it is analyzed the thermal condition in the fuses. The calculation of the fuse transient heating is done by OrCAD PSpice 9.0 software, where, given the analogy between the electric and thermal quantities, is simulated the fuse heating. In order to evaluate the thermal field in ultrafast fuses, the FLUX2D 7.40/6 simulation program was used. The thermal field variation along the whole fast fuse body and along the fuselink are presented and analyzed.**

Keywords—fast fuse; power electronic protection protection; fuselink; thermal model; simulations

I. INTRODUCTION

The operating failure of many power semiconductor devices is due to the application of overvoltage. Even a short time of blocking voltages and inverse stresses can give a breakdown that may occur in insulator piercing or arcing-over. The new semiconductor devices have a high capability in normal conduction mode, but are quite sensitive to short and highly intensive overcurrents, due to their low thermal capacity. These may be degraded or destroyed by overloads in direct conduction. The level of the degradation depends on the value and duration of the applied pulse currents. Injecting into the device a direct conduction current of a high value (overload current) over one or many periods, may cause the power-locking capability to be permanently affected.

If the direct conduction current pulses (unpredictable overload) are not followed by reapplying the blocking voltage, a gradual degradation of the semiconductor device appears. It has to be specified that, after this overload, the device temporarily loses its locking capability, and also the capacity to respond to gate control, until the temperature of the semiconductor element drops below 150^0C in thyristors.

Thus, temperature is a physical parameter having a very important influence on the semiconductor power device operation: it influences the magnitude of the electrical characteristics of the device, it influences the way the mechanical or climatic stresses.

Considering the thermal phenomena complexity for power semiconductors, it is difficult to study the heating processes in steady-state and transitory operating conditions, by using the traditional analytical models. The modeling concepts have their strength for different grades of complexity of the circuit. It is important to realize an efficient tradeoff between the necessary accuracy, required simulation speed and feasibility of parameter determination [1].

Many articles are based on the thermal RC networks which use the PSpice software [2], [3]. Electro-thermal simulations using finite element method are considered in [4]. Combination with the conventional RC thermal network in order to obtain a compact model is presented in [5].

Another study, [6] presents a new heatsink design and material process that allows porosity-free low cost heatsinks. A thermal resistance model was established in [7] in order to analyze the heat transfer in microchannel heatsinks. Thus, the major limitation of the stresses is a thermal limitation. In the transient regime or in the case of a variable load, the thermal circuit assumes/admits an equivalent circuit where every section of the diode-heatsink assembly is represented by its resistance and thermal capacity taking into account that in every section is accumulated a part of the heat released in the junction [8], [9].

Thermo-mechanical aspects of fuses used in power electronics are studied in [10] with microscopic analysis and FEM thermo-mechanical simulation estimating the temperature variation at the end hole of the fuse element. A method to select the fuse and MOSFET for a DC/DC converter is presented in [11], using the Joule-integral principle to estimate the energy associated with the fuse. Various fuse melting characteristics are considered to choose the suitable melting time by comparing them with the thermal characteristics of the circuit.

In order to study the thermal energy during the fuse melting, data analysis methods, such as sampling, variance analyze and residual sum of squares analyze, are considered [12]. These methods provide the optimal equation to describe the relationship between time, fault current and the thermal energy into the fuse, both in DC and AC.

In this article thermal aspects regarding the fast electric fuses are considered. In order to evaluate the thermal field in ultrafast fuses, the FLUX2D 7.40/6 simulation program was used. The thermal field variation along the whole fast fuse body and along the fuselink are presented and analyzed.

II. ULTRAFAST FUSE CHARACTERISTICS

The power semiconductors, such as diodes and thyristors, are protected against overcurrents by using ultrafast fuses connected in series with them.

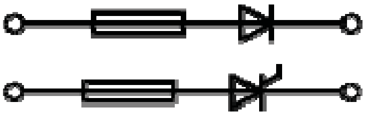

Fig. 1. Protection of diodes and thyristors with fast fuses.

Fig. 2 presents the main construction of a fast electric fuse. The essential part is the ultrafast fusible, which is made of one or many conductive bands, which have in their structure small section areas in order to assure the fusion at certain accurate zone areas. The geometry of the system is very important, because it influences the qualities of the fuse and of the interrupted circuit element.

The conductive bands are realized from copper, silver, or some alloys, having a good stability at acceptable temperatures and overloads. The use of aluminum has been tried too, but, from two important reasons, the aluminum is not very used: once, when the current is cut-off, there appears an exothermal reaction at aluminum burning, and second, under the influence of the electric arc high temperature, an important exothermal reaction occurs in the quartz sand environment.

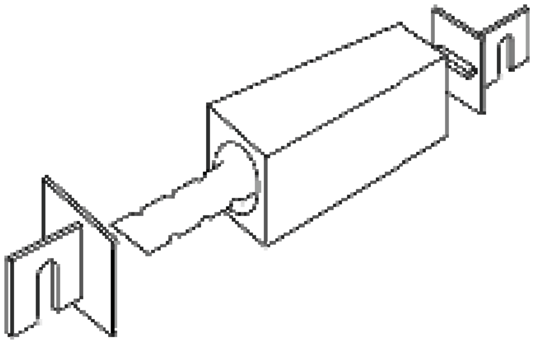

Fig. 2. Fast fuse construction.

Using the metals which do not oxidize in depth is based on the fact that the current densities in the strangled sections are excessively high and, likewise, the temperatures are the same. When it is used the copper, very high temperature lead to its oxidation, accelerated section reduction and, therefore, to the melting of the fusible. Silver is also oxidized, but the thickness of the AgO layer is in the order of about 10^{-9} m, and the oxide which is formed will prevent a further oxidation of material. Thus, silver is the most used material for the ultra-fast fuses achievement.

Considering that for the aluminum fusible bands, an exothermal reaction appears when the currents are cut-off, this aspect can be used in the production of silver plated aluminum fused bands on the outer surface, or a mix between copper and silver plated aluminum, by using a quenching medium, different from quartz sand, to have a maximum exothermal reaction.

The fused bands are usually located in quartz sand with a specific granulation and with a homogeneous porosity in order to absorb the thermal energy and to assure insulation after the circuit cut-off. The main function of the quenching medium is to disconnect, as fast as possible, the electric arc which appears inside the fuse. Another, function is to convey the heat released inside the fuse and to protect the fuse, and mainly the oxidizing fuses, against the external elements and the electric ageing.

It is evident that it is impossible in practice to assure these three requirements using the quartz sand and classic fill technologies. The quality of quartz sand must be in line with these demands. Thus, a good quartz sand must have in its composition, (from STAS 5923-76), more than 99% $SiO2$ and less than 0.5% $Al2O3$, 0.2% CaO, 0.03% $Fe2O3$, 0.04% $T2O2$.

The action of the quenching medium is also in connection with the quantity of metallic vapours produced by the fusible metals. Thus, copper and silver fuses give a lower quantity of metallic vapours in the electric arc, which favors its quenching.

Another important aspect is that the volume of the ceramic sleeve must be filled with a maximum quantity of sand. This can be assured by using an optimal grain size, i.e. choosing the correct ratio between the masses of the grains ranging: 0.1 and 0.2 and 0.3, 0.3 and 0.4, 0.4 and 0.5 mm, so that the total mass should be maximal. Other arc quenching materials are chalk - $CaCO3$, ZnO, and silicon carbide - SiC.

Further, by comparison to the quartz sand, there are presented voltage and current waveform oscillograms, when it is used an ultra-fast fuses with a rated current of 100 A, [13], all fuses were tested under the same conditions at a current of 500 A, Fig.3, Fig. 4, Fig. 5, Fig.6.

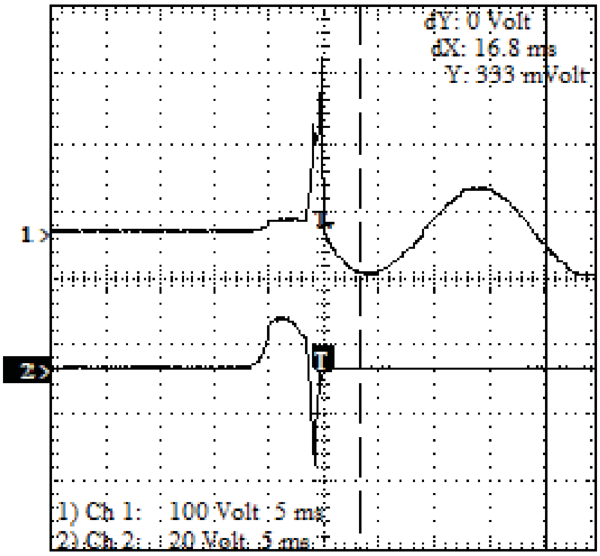

Fig. 3. Quartz sand filler.

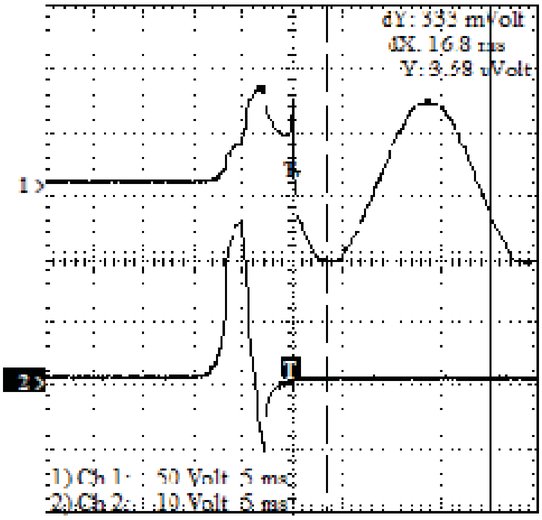

Fig. 4. CaCO3 filler.

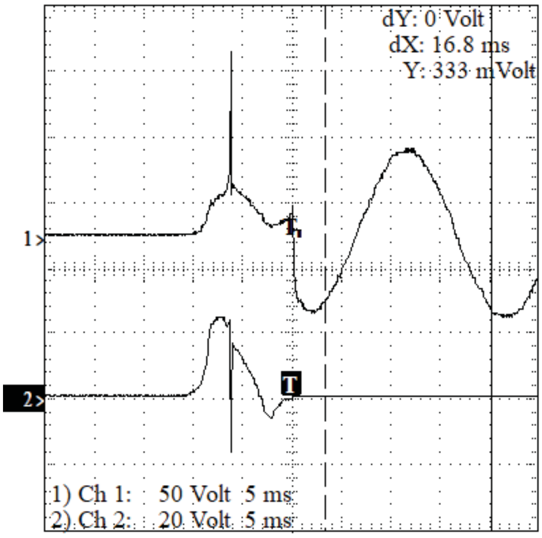

Fig. 5. ZnO filler.

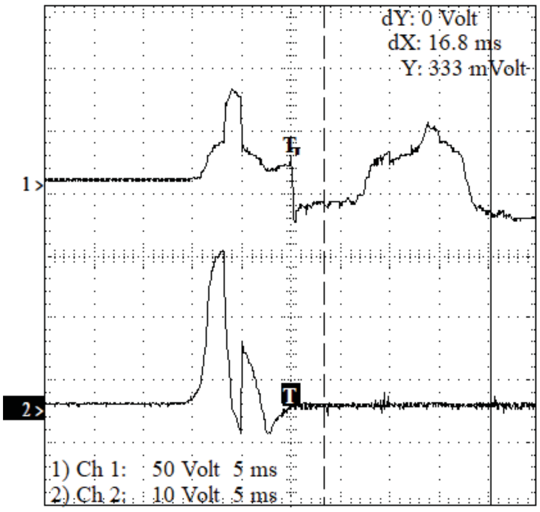

Fig. 6. SiC filler.

At all these oscillograms have been recorded the waveforms of the arc voltage which is the upper waveform on the graph and the arc current which is the lower recorded waveform on the graph. The shapes are different in concordance with the test conditions applied - different type of fillers which cover the fuselinks.

From the oscillograms, it results that in for the extinguishing medium of CaCO3 and ZnO, there appear very high overcurrents and overvoltages which would lead to the destruction of the semiconductor. When the silicon carbide is used as filling material, it is observe that the fuse does not have the capacity to break the current at a proper time, which, finally, gives an improper protection of the semiconductors.

Thus, as a result of these experimental researches it is to mention that the best quenching medium for the actual fuses is the quartz sand. In usual operating mode, the energy given by the Joule effect in the conducting bands is released to the exterior medium via conductors, filling material, connexions, and envelope.

For a high amplitude overload, the fuse element stores more energy than it can release, which causes an internal temperature increase which will cause the fusion of the small section areas. The current-time and voltage–time diagrams, corresponding to the operation of an ultrafast fuse run by a short circuit current are presented in Fig. 7. The main characteristics of an ultra-fast fuse in alternating current are:

- U_n, the nominal voltage, i.e. the highest effective value of the voltage that can be applied between the fuse terminals;
- I_n, the nominal current, the highest effective sinusoidal current that the fuse can withstand indefinitely, without burning the fuse and without changing its characteristics, considering a natural cooling of the fuse;
- t_p, the pre-arc time, the time elapsed between the apparition of the short circuit (t=0) and the time when the electric arc appears into the fuse ($t = t_p$); corresponding to this time, there is the pre-arc current integral, $(I^2t)_p = \int_0^{t_p} i_{sc}^2 dt$, which is a constant; During the pre-arc time, the fusible element passes from the solid state to the liquid state;
- t_a, arc–time, the time interval between the occurrence of the electric arc ($t = t_p$) and the moment of its extinction (circuit breaking, $t = t_t$); the arc current integral, $(I^2t)_a = \int_{t_p}^{t_t} i_{sc}^2 dt$, which is not a constant, and depends on the circuit parameters;
- t_t, the total time of power failure, the time between the moment of the short-circuit appearance and the moment when the current was cut off, this being the sum of the pre-arc and arc times,

$$tt = tp+ta. \qquad (1)$$

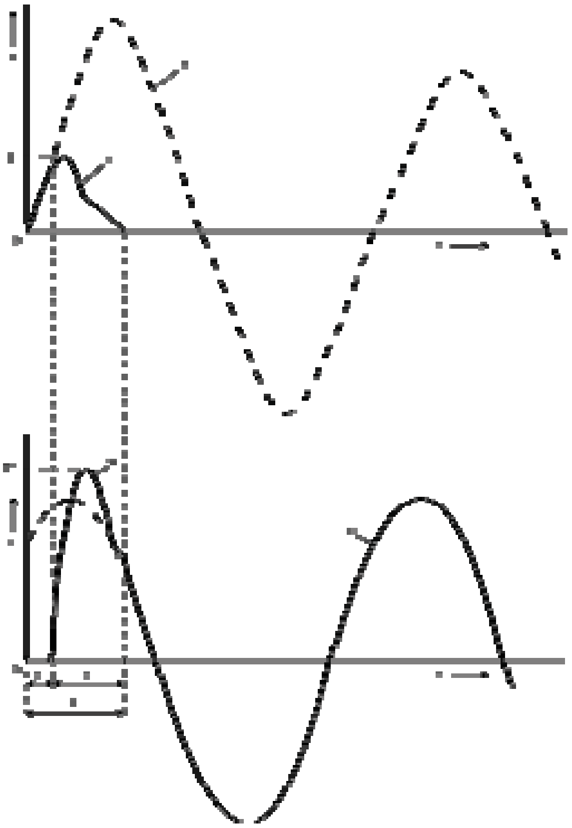

Fig. 7. Current – time and voltage – time diagrams for a fast fuse operating.

- I^2t, the total current of the fuse, is the sum of the pre-arc and arc current integrals:

$$I^2t = \int_0^{t_t} i_{sc}^2 dt = \int_0^{t_p} i_{sc}^2 dt + \int_{t_p}^{t_t} i_{sc}^2 dt . \qquad (2)$$

This is an indication of the energy released in the replacing element over its lifetime. The electric fuses producers provide the variations of I^2t in relation with the ratio of the effective value of the assumed fault current, I_p, to the effective value of the nominal current I_n, for an operation below the rated service voltage, U_n, the parameter being the nominal current, I_n, [9-12].

- t_p, pre-arc real time, depending on the effective value of the pre-arc current:

$$I^2 p = \frac{1}{t_p} \int_0^{t_p} i_{sc}^2 dt \qquad (3)$$

All of these allow checking the fuses in terms of the ability to withstand low amplitude overload currents [14], [15]. The temperature of the fuse links is influenced by their section. If these conductors are wrongly chosen, the fuse may be excessively loaded. Generally, the manufacturer's specifications on the fuses inform on which conductors should be used for connections.

In the case of Direct Current, the cutting-off of short-circuit current by using fuses is more difficult because [14], [16]:

- The current integral, I^2t, is approximately the same in direct and alternating current for the same short-circuit current value and for the same voltage, if the time constant of the circuit is lower than 20ms. At higher time constants, I^2t in direct current is approximately equal to I^2t of pre-arc, and it increases, approximately, by the square root of the time constant;
- The limiting current in DC situation is lower than that in the AC case. It has the current magnitude order at the moment of arc initiation. The limiting current in DC is not superior to the one obtained in AC, excepting for very low time constants (under 1.5ms).

In the case of AC and DC, respectively, the choice of the ultrafast fuse is assured depending on the effective current flowing through and the effective voltage that occurs at its terminals after its operation.

III. TRANSIENT HEATING

The estimation of the transient heating for the fuse is very important, in order to find the pre-arc times of specific imposed overcurrents, and to verify the temperatures reached on the fusible bands when the fuses must not work. The same is valid when the overload characteristic diagram is needed.

Fig. 8 described the equivalent thermal scheme considering, in a simplified way, the fuse concentrated parameters. This equivalent thermal scheme is not quite proper to practical calculations because, the thermal resistances of the component elements cannot be calculated precisely and, moreover, the equivalent scheme is much simplified. At this diagram, the included symbols mean the thermal resistance R_{th} for different main components of the fuse (fuselinks, filler material, ceramic body) and the thermal capacities C_{th} of the same components of the fuse. This diagram can be used for thermal analysis during transient conditions of the fuse.

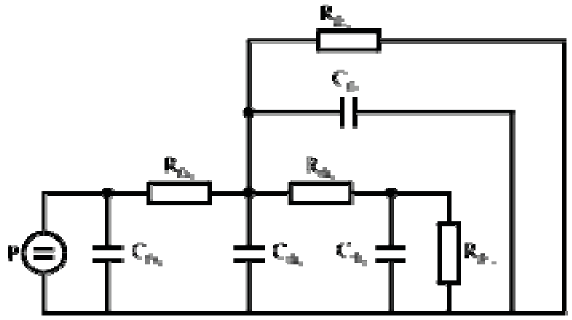

Fig. 8. Equivalent thermal circuit of the fuse during transient regime.

A better estimation may be done by using the OrCAD PSpice 9.0 software, where, given the analogy between the electric and thermal quantities, it can be simulated the fuse heating at different forms of power pulses, in a similar way to the power semiconductors. Thus, Fig. 9 presents a comparison between the temperature variation during transient conditions of the fast fuse fuselink temperature (T1 - upper waveform) and the power diode semiconductor junction temperature (T2 - lower waveform). Because of thermal power pulses, which means actually the thermal load for power semiconductor diode in series with the fast fuse, there are temperature increases and decreases. After approximate 4...5 thermal constants of the analyzed system, the temperatures will reach steady-state conditions.

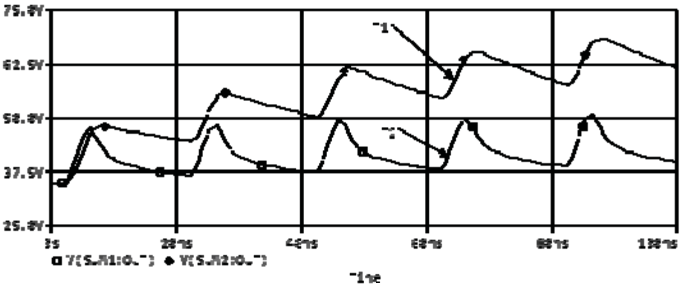

Fig. 9. Comparison between temperatures variation during transient regime in the case of rectifier diode and its fast fuse.

An example of a power rectifying deck has been considered, where the diodes have an average rectified current of 100A, each of them being protected by an ultrafast fuse of 200A. The simulation of the thermal field was realized for an ultra-fast current fuse with 100A nominal current. The environment temperature was considered as constant at 20^{0}C. Due to the symmetry of the fuse, only half of the simulation was realized, the thermal field in the other half being identical, the axis of symmetry passing through the contacts, the envelope, and the fusible band.

There are some steps necessary to the creation of the thermic spectrum for the fuse:

- Designing the geometry of the ultrafast fuse;
- Determining the mesh network, Which is important in calculating the thermal field by FEM;
- Establishing interdependencies with the electric circuit where the fuse is located;
- Considering the border conditions;
- Solving the electro-thermal type problem.

The thermal field corresponding to the set in its entirety was found at the moment t = 26.04s, and the components were analyzed at the moment t = 28.75s, the next calculation step corresponding to a maximum temperature of 988°C of the fusible band, it being already cut-off, which renders this moment useless to the analysis, because the silver fuse melts at 960°C.

Fig. 10 shows the thermal field along the hole fast fuse body at t = 26.04 seconds.

It results that the thermal field can be studied actually in any point inside the fuse, the thermal spectra confirming that the maximum values are obtained on the fusible band, while the lowest belong to the porcelain envelope.

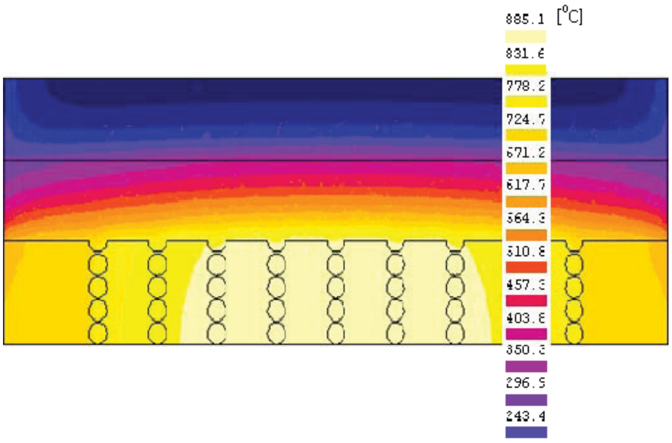

Fig. 10. Thermal field in whole fast fuse body at t = 26.04 seconds.

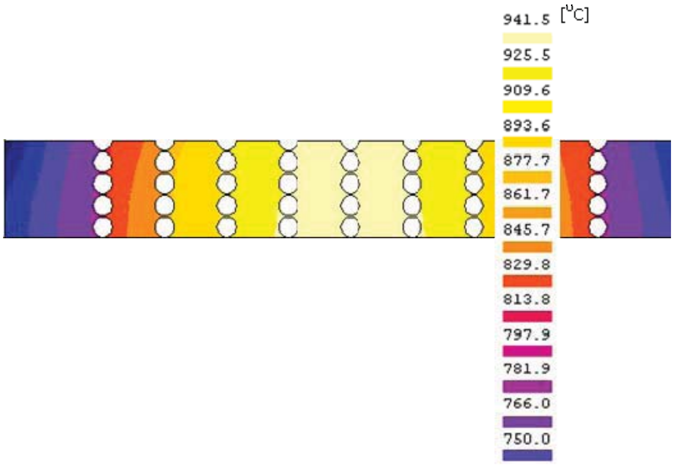

Fig. 11. Thermal field along fuse-link at moment t = 28.75 seconds.

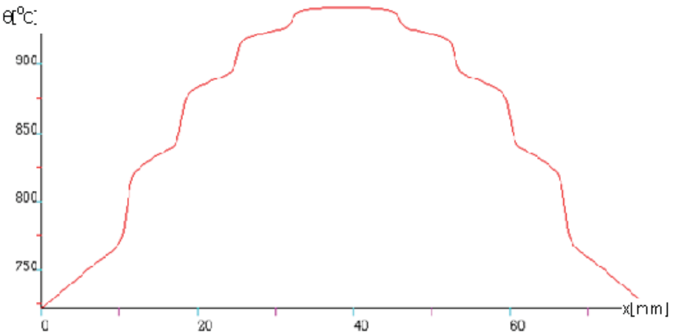

Fig. 12. Temperature distribution along fuselink at moment t = 28.75 seconds.

The temperature distribution along the fusible band, Fig. 11, presents the influence of the isthmus on the thermal field, which evolves somewhat in stages, up to the maximum value, placed in the middle of the fusible band.

IV. CONCLUSIONS

Temperature is a physical parameter having a very important influence on the semiconductor power device operation. By comparison to the quartz sand, there are presented voltage and current waveform oscillograms, when it is used an ultra-fast fuses with a rated current of 100 A. As a result of these experimental researches it is to mention that the best quenching medium for the actual fuses is the quartz sand. The necessary steps to the creation of the thermic spectrum for the fuse. By the simulations, the thermal field can be studied in any point into the fuse, resulting that the maximum values are obtained on the fusible band, while the lowest belong to the porcelain envelope.

ACKNOWLEDGMENT

This work was supported by a grant of the Romanian Ministry of Research and Innovation, CCCDI - UEFISCDI, project number PN-III-P3-3.1-PM-RO-CN-2018-0060/ 25BM/2018, within PNCDI III.

REFERENCES

[1] P. Aloisi, “L'avenir des IGBT”, REE, no.4, Avril, pp. 43-47, 1997.

[2] B.K. Bose, “Recent Advances in Power Electronics”, IEEE Trans. Power Electron, vol.7, no.1, pp. 2-6, 1992.

[3] B.K. Bose, “Evaluation of Modern Power Semiconductor Devices and Future trends of Converters”, IEEE Trans. Ind. App., vol.28, no.2, pp. 403-413, 1992.

[4] D. Braun, D. Pixler, and P. LeMay, “IGBT module rupture categorization and testing”, IEEE Industry Application Society, Annual Meeting, New Orleans, Louisiana, United States, pp. 1259-1266, 1997.

[5] J.P. Brozek, “DC overcurrent protection – where we stand”, IEEE Trans. Ind. Appl.s, vol.29, pp. 1029-1032, 1993.

[6] R. Eisele, K.K. Olesen, and F. Osterwald, “Shower Power — Brausestrahl versus traditionelle Flüssigkeitskühlung”, Elektronik Praxis, vol. 10, 2008.

[7] B. Allard, H. Garrab, and H. Morel, “Electro-thermal simulation including a temperature distribution inside power semiconductor devices”, Int. J. of Electronics, vol.92, pp. 189-213, 2005.

[8] K. Jakubiuk and W. Aftyka, “Heating of fuse-elements in transient and steady-state”, Proc. of the 7th Int. Conf. on Electric Fuses and their Applications (Gdansk), pp. 181-187, 2003.

[9] E. Torres, E. Fernandez, A.J. Mazon, I. Zamora, and J.C. Perez, “Thermal analysis of medium voltage fuses using the finite element method”, IEEE Russia Power Tech, pp. 1-5, 2005.

[10] A. S. Bahman, F. Iannuzzo, T. Holmgaard, R. Ø. Nielsen, and F. Blaabjerg, “Reliability-oriented environmental thermal stress analysis of fuses in power electronics”, Microelectro Reliab, vol. 76, pp. 25-30, 2017.

[11] J. L. Soon and D. D. C. Lu, ”Design of Fuse–MOSFET Pair for Fault-Tolerant DC/DC Converters”, IEEE Trans Power Electron, vol. 31(9), pp. 6069-6074, 2016.

[12] W. Tian, C. Lei, Y. Zhang, D. Li, R. Fu, and R. Winter, (2016, July).”Data analysis and optimal specification of fuse model for fault study in power systems”, IEEE Power and Energy Society General Meeting (PESGM), pp. 1-5, 2016.

[13] R.E. Simons, “Estimating parallel plate-fin heat sink thermal resistance”, Electronics Cooling, vol. 9, pp. 8-9, 2003.

[14] N.J. Zhou, J.Q. Zhang, and S.H. Zhou, “Electric and thermal simulation for short circuit busbar of aluminum reduction cells”, Journal of Central South University (Science and Technology), vol. 41, pp. 1609-1615, 2010.

[15] H.J. Beukes, J.H.R. Enslin, and R. Spee, “Busbar design considerations for high power IGBT converters”, PESC Record - IEEE Annual Power Electronics Specialists Conf. 2, pp. 847-853, 1997.

[16] M.J. Taylor, “Current diversion around a fragmenting wire during the voltage spike associated with exploding wires”, Proc. of the 7th Int. Conf. on Electric Fuses and their Applications (Gdansk), Poland, pp. 1-9, 2003.

Indian Journal of Science and Technology, *Vol 9(40), DOI: 10.17485/ijst/2016/v9i40/86733, October 2016*

ISSN (Print) : 0974-6846
ISSN (Online) : 0974-5645

Switched Reluctance Generator for Low Speed Wind Turbines with Counter-Rotary Drive

Costica Nituca[1]*, Dumitru Cuciureanu[2] and Gabriel Chiriac[1]

[1]Technical University "Gheorghe Asachi" Iasi, Faculty of Electrical Engineering, Bd. D. Mangeron, nr. 21- 23,
Iasi - 700050 Romania; costica_nituca@yahoo.com, gchiriac@tuiasi.ro
[2]"Q" SRL Iasi, Stradela Sf. Andrei nr.13, Iasi, Romania; office@qsrl.ro

Abstract

Background/Objectives: To design a new type of switched reluctance generator for low speed wind turbines which operate at low speed wind. Methods/Statistical Analysis: Structure and operation principle of the proposed switched reluctance machine are described. The generator-wind turbine is a direct-drive one and has two mobile parts which can be droved by two wind turbines in counter-rotary motion. A test bench was achieved and two types of experiments were realized: first, with a part of the generator fixed and the other in rotary motion, and second with the both parts in motion. Findings: Using the counter-rotary motion it results an important increasing of the output voltage of the generator for the same speed. The generator can be used both for the turbines with horizontal or vertical axle, with some advantages for the vertical axes case, especially in urban area, where safe operation of vertical axis wind turbines requires low rotational speeds to reduce noise, mechanical vibrations and proximity hazards. Applications/Improvements: The proposed direct-drive generator is more efficient than the classical structure with gears and the simple rotary motion.

Keywords: Counter-Rotary Motion, Low Speed Wind, Switched Reluctance Generator, Wind Turbine

1. Introduction

In nowadays context of energy crisis and consuming of the resources, the optimal utilization of the regenerative energy is a priority. The wind energy is one of the opportunities to have more clean energy with fewer drawbacks. Estimated wind capacity by the year of 2020 is expected to increased to about 1 260 000 MW, which will be about of 12% of the world's electricity consumption[1]. There are three types of generator systems for wind turbines[1]. The first type is a fixed-speed wind turbine system using a multi-stage gearbox and a standard squirrel-cage induction generator. The second type (developed from 1990s) represents a variable speed wind turbine system with a multi-stage gearbox and a doubly fed induction generator, with a power electronic converter feeding the rotor winding. The third type is also a variable speed wind turbine, but with a direct-drive generator, usually a low-speed high-torque synchronous generator. A power electronic converter for the full-rated power is necessary for the grid connection[2-4]. Usually, the conversion of the energy is realized by using the electric generators which are adapted to the parameters of the wind turbines. One solution is to use a step-up gear which increases the price, reduces the efficiency and needs maintenance. Heavy weight, large volume, noise, and vibrations are also significant drawbacks.

Another solution is to use a direct-drive Switched Reluctance Generator (SRG). This machine is robust, easy to construct, reliable, and it needs low maintenance. The use of power electronics and a good control will reduce some drawbacks as torque, current and voltage ripples and, as a consequence, the SRG has great developing potential in the area of wind power generation[5-7]. Distortion in main grid can disturb the protection equipments, being necessary supplementary tests and better protection to avoid interruption in power supply[8,9]. Some studies regard to produce the maximum output power at a given shaft speed for a SRG[10]. There is also interest in

---

Author for correspondence

harnessing wind power on-board of an electric vehicle using Switched Reluctance Generator (SRG) coupled to a wind turbine mounted on the vehicle[11]. Small-scale wind turbines are a solution for the energy consumption into the urban area and their modelling and analysis is a necessary step for their implementation[12]. Different controlling methods are used for the wind turbine applications, as neural network controller[13] or sliding mode control[14].

Moreover, safe operation of the Vertical Axis Wind Turbines (VAWT) in restricted urban spaces requires low rotational speeds to reduce noise, mechanical vibrations and proximity hazards[15]. The VAWT are better adapted to be installed nearby the residential and urban areas because they have lower start-up speed and low noise level. These are also appropriate to be installed in areas with strong winds and, as an important advantage, the VAWT are indifferent to wind direction[16].

In this paper a new type of switched reluctance generator for the variable low speed wind turbines with counter-rotary drive has been studied. It could be used for both vertical and horizontal axis wind turbines, in urban environments or in remote area without a grid connection.

2. The Wind Power

The kinetic energy of the air flow is estimated by using the energy flux density, which is the quantity of the energy which crosses, in a constant and uniform way, a unit surface normal to the wind direction in a unit of time. The specific power of an air flux is given by the relation (1)[17-20], where the density of the air could be considered as constant, the wind turbines being usually less then 100 m high:

$$P = \frac{1}{2}\rho_{air} A v^3_{wind}\,. \tag{1}$$

Where $\rho_{air} = 1.225$ kg/m^3 is the air density, v_{wind} is the speed of the wind and A is the swept area.

For a surface of A = 1m^2, the variation of the specific power for the air flux is drawn in Figure 1, resulting significant values starting with a wind speed of about 8m/s. Therefore, the nominal speed of the large wind turbines is about 10÷15 m/s[20]. A duplication of the wind speed will give an increasing of 8 times for the power of the wind turbine, which is given by[18,21,22]:

$$P_{turbine} = \frac{1}{2} C_p \rho_{air} A v^3_{wind}\,. \tag{2}$$

where C_p is the power coefficient.

An efficient utilisation of the low speed wind can be obtained with two coaxial rotors with counter-rotary motion, which will give a double equivalent speed comparing with a single rotor system at the same dimensions. The solution is useful especially for low dimensions of the rotors (about two meters) and with speeds of about 500…600 rot/min[17]. Figure 2 shows the variation of the specific power of air flow at low speed of the wind. For the wind turbines with one rotor it has values between 0.61÷76.56 [W/m^2] (curve 1), while, for the wind turbines with counter-rotary motion the power is double (curve 2), 1.22÷153.12 [W/m^2]. These values are relatively low, but, with an optimization of the system, these powers could be used for low or medium power applications. The efficiency of the wind energy conversion is estimated by using a power coefficient C_p. The Betz model[17] is based on a tube of current with a constant area; for a wind turbine this area is the surface corresponding to the blades motion. In reality this surface is not constant. The maximum power P_{maxH} given at the rotor of a wind turbine with horizontal axle is[17]:

$$P_{\max H} = \frac{1}{2}\rho_{air} A v^3_{wind}\frac{16}{27}\,. \tag{3}$$

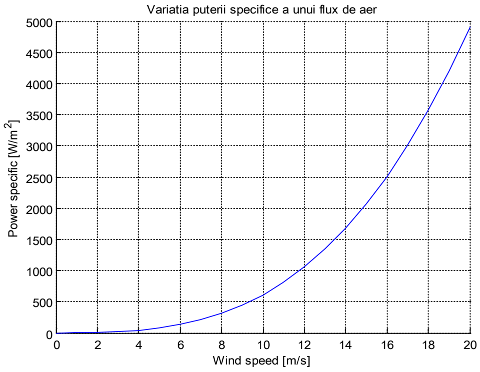

Figure 1. Specific power variation for the air flux.

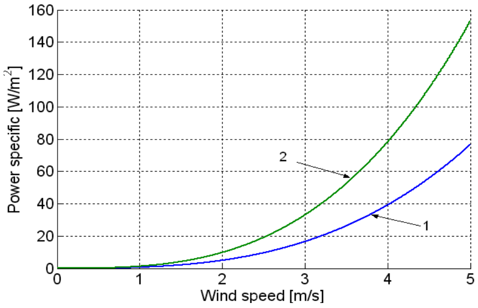

Figure 2. Specific power variation at low speed.

The power coefficient is:

$$C_p = \frac{P_{\max H}}{\rho_{air} A v^3_{wind} / 2} = \frac{16}{27} = 0.59. \tag{4}$$

For a wind turbine with vertical axle the maximum power $P_{\max V}$ and the power coefficient are[17]:

$$P_{\max V} = \frac{1}{2}\rho_{air} A v^3_{wind} \frac{4\sqrt[4]{5^3}}{25}, \tag{5}$$

$$C_p = \frac{4\sqrt[4]{5^3}}{25} = 0.53. \tag{6}$$

The values resulted from using the global methods are higher than the real values. In the aerodynamic theory, there are proposed mathematical models which study the dynamic equilibrium of the forces, with more appropriate values on the real ones. An example for the wind turbine with vertical axle is by using the method of the tube currents with a single coefficient of influence. This method offers a calculus for different values of the solidity[17], s = 0,2; 0,3; 0,4; 0,5; 0,6 using the relations[21]:

$$s = NC / R_r, \tag{7}$$

$$\lambda = \omega R_r / v_{wind}, \tag{8}$$

$$\overline{F}_n^* = \frac{F_n^M}{\rho_{air} a C v^2_{wind} / 2}, \tag{9}$$

$$C_p = \frac{P}{\rho_{air} a R v^3_{wind}}. \tag{10}$$

where: N -Number of the blades; R_r - Rotor radius; ω -Angular speed of the rotor, F_n^M - Maximum normal force relative to a rotating blade; $\overline{F}_n^*$ -Maximum normal force on the blade; a - influencing coefficient.

Considering the relations (7–10), in Figure 3 and Figure 4 are presented the force and the power coefficient. For this it was also considered the coefficient of lifting and the coefficient of resistance for the blade profile NACA 0012[17]. These theoretical methods are possible to apply while the constructive type of the wind turbine is corresponding to the model. Thus, for an optimal use of the low speed wind it is necessary to identify the type of turbine, the starting torque, the maximum power given by the wind and the optimum values of the speeds. For the wind turbines with vertical axle the best turbines are the ones with fixed blades and with oscillating blades[17].

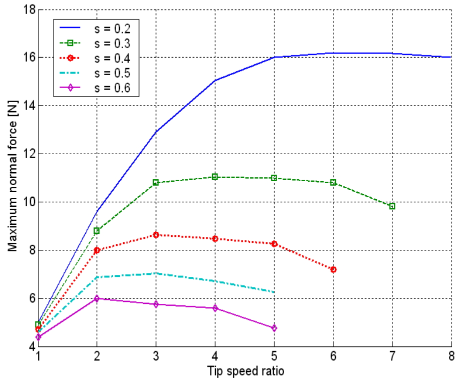

Figure 3. Maximum normal force on blade related to the tip speed ratio.

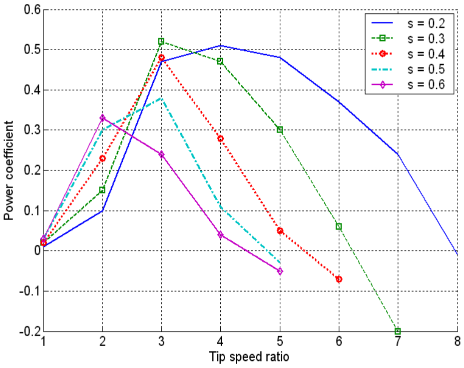

Figure 4. Power coefficient depending on the tip speed ratio.

In this situation, for the wind turbines with horizontal axle the best are the slow wind turbines (with many blades, which are adapted for low speed winds, at 1…3 m/s), at which the maximum efficiency is for a tip speed ratio of λ = 1 and C_p = 0.3, that is for an energy intake of about 50% from the Betz limit. This value corresponds for an optimal rotation speed:

$$n = \frac{60 v_{wind}}{\pi D} \approx 19 \frac{v_{wind}}{D} \tag{11}$$

3. Structure and Operation Principle of the Proposed Switched Reluctance Machine

3.1 Structure of the Proposed Switched Reluctance Machine

The construction of the proposed switched reluctance machine is presented in Figure 5. For this type of generator

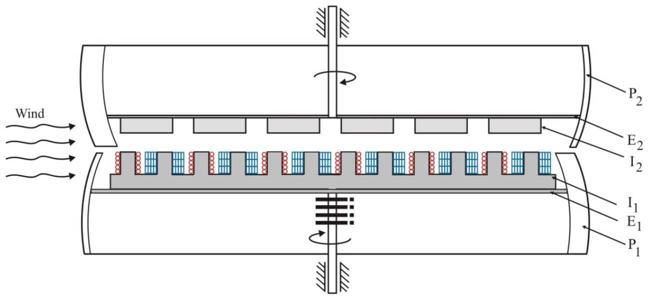

Figure 5. Schema of the proposal switched reluctance generator.

we will use the expressions "the function of inductor" and "the function of armature" and not the terms inductor and armature, because the both parts, the inductor and the armature, are in the same mechanical structure. This type of generator is proposed for operating at low speed because of some advantages as: simple construction, with the possibility to operate in counter-rotary regime; it is eliminated the kinematical chain because the turbine is directly connected to the axle of the turbine, so the energy loss are reduced; the generator is simple to adapt to the wind turbine operation both on constant or variable speed; there are no permanent magnets, so the costs are lower; the generator can operate in single-phase, three-phase or multi-phase construction.

The generator can be used both for the turbines with horizontal or vertical axle, with some advantages for the vertical axes case, especially in urban area, where safe operation of vertical axis wind turbines requires low rotational speeds to reduce noise, mechanical vibrations and proximity hazards. Also, they are well suited to such environments due to their inherent axisymmetric design[15].

According to the Figure 5, the magnetic circuit with function of inductor and armature (I_1), is built from sheet iron, fitted with teeth and notches which are uniformly distributed along the magnetic circuit, into a disc shape. Ahead of this circuit there is another disc magnetic circuit (I_2), made up from a succession of elementary magnetic circuit with the same tooth pitch as the magnetic circuit (I_1). These two parts, (I_1) and (I_2), can be droved in counter-rotary motion by two wind turbines (E_1) and (E_2), with vertical or horizontal axle. In the case of the horizontal axle, the counter-rotary motion is assured by a system of two counter-rotary co-axial turbines, while, for the vertical axle shown in Figure 5, the counter-rotary motion is assured by using two rotary turbines (E_1) and (E_2) with an appropriate orientation of the blades (P_1) and (P_2), so that, regardless the direction and the speed of the wind, the two turbines will have a counter-rotary motion.

This type of construction could have a small size (2 m diameter and 3 ÷ 4 m vertical axis) so they could be used on a special wind turbines in urban area on the rooftop of buildings, as discussed in[23].

3.2 The Operation Phases of the Switched Reluctance Generator

The main operation phases of the switched reluctance generator are presented in Figure 6. On the odd teeth 1, 3, 5 are realized the D.C. operating windings. The odd teeth, 1, 5, 9, 13 (defined by the relation 1 + 4n, n = 1...30), have operating windings which generate a positive excitation flux, while the odd teeth 3, 7, 11, 15,

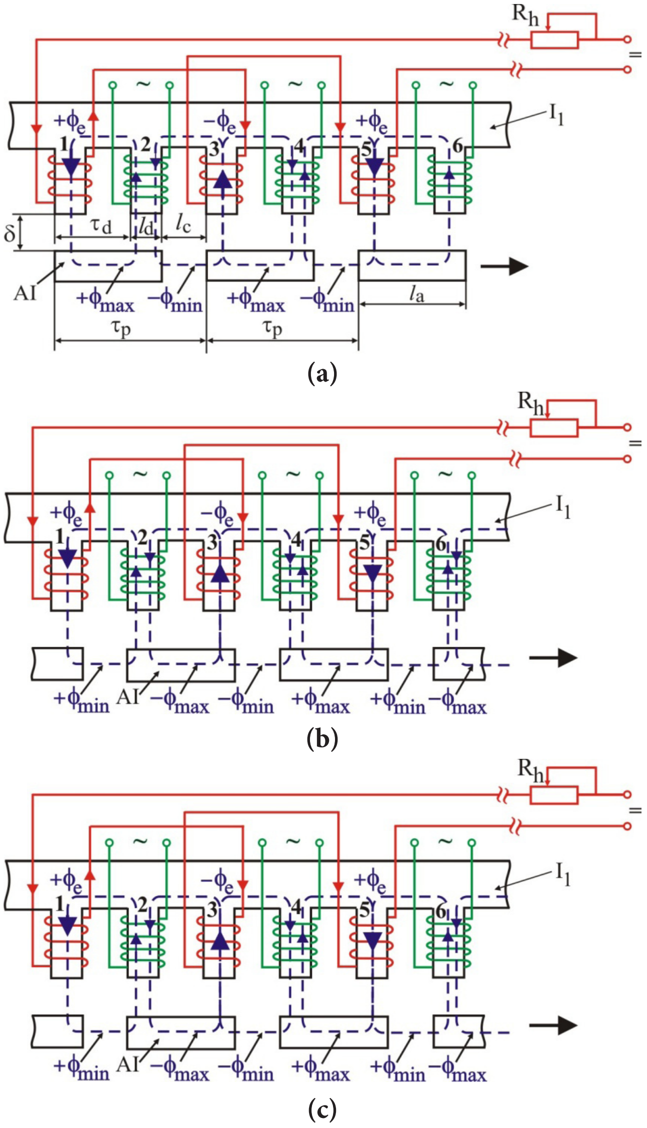

Figure 6. The main operation phases of the switched reluctance generator.

(defined by the relation 3+4n, n = 1...30), have operating windings which generate a backward (negative) excitation flux, from the tooth to the yoke of the machine. All these odd teeth are actually field poles with small size and they have the function of an inductor. Between these teeth there are the even dental/teeth 2, 4, 6, 8 etc with windings that have function of armature windings. It is to observe that between the magnetic circuit with teeth and notch (at a distance δ - air gap of the generator), there are some armatures for the inductor flux closing (denoted *AI* and arranged on a disk). The length of such an armature is $l_a = \tau_d + l_d$, where τ_d is the tooth pitch, and l_d is the width of a tooth. In Figure 6.a. the closing armature AI is exactly in front of two teeth, 1 and 2, and of a notch. The positive flux ($+\Phi_e$) created by the pole no. 1 closes by the tooth 1, air gap, the armature AI, air gap, the tooth no. 2 with the role of armature, by joke and again the tooth no. 1. The total air gap is minimum, that is 2δ, and the flux will be maximum, because the reluctance is minimum.

In Figure 6.b. the closing armature AI is moved a half of a tooth pitch, the edges of the armature being in front of the sideways of the teeth 1 and 3, and its middle being in front of the tooth no. 2, which has a role of armature. Along of a flux line it will be two air gaps and a quarter of circle at the right edge of the armature AI. The flux in tooth no. 1 is decreasing at ($+\Phi_{min}$) and will cross the tooth no. 2. At the same time, the pole on the tooth no. 3 will also generate a minimum flux ($-\Phi_{min}$), but in opposite direction ($-\Phi_e$), which will cross the tooth no. 2 in opposite direction and will cancel the effect of the flux ($+\Phi_{min}$). Thus, in this position of the armature, in the tooth no.2 the total flux will be zero. Continuing its movement, the armature AI will be in front of the teeth 2 and 3. Through the tooth no. 3 will cross a maximum flux, but with an opposite sign, $-\Phi_{max}$ and a positive flux $+\Phi_{max}$, which will also cross through the tooth no.2. As a consequence, it will be cross by the difference between the two fluxes ($-\Phi_{max} + \Phi_{min}$). During a variation cycle, the armature coil on the tooth no. 2 will be crossed alternatively by the flux variation given by ($+\Phi_{max} - \Phi_{min} > 0$) and ($-\Phi_{max} + \Phi_{min} < 0$). To estimate the variation space of this flux at the new type of generator, let us consider the space which has to be crossed in a complete variation period S_{pvc}. For this it can be written the relations:

$$S_{pvc} = 2\tau_p \text{, but } \tau_p = 2\tau_d \text{, and it results,}$$
$$S_{pvc} = 2 \cdot 2\tau_d = 4\tau_d \text{,} \tag{12}$$

where τ_p is pole pitch.

The proposal generator has a large number of poles, both as inductors and as armatures but of small size. This allows to put in series many induced windings and so the resulted voltage will have significant values even for low speed variation of the inductor flux. The efficiency of the machine depends on the ratio between the maximum and minimum reluctance.

4. Experimental Data

Two types of experiments were realised. First experiment was realized with a part of the generator (I_1) fixed and the other part (I_2) in rotary motion, droved by an electric motor M2 (the K2 switch is closed) shown in Figure 7. A second experiment was realized with the both parts of the generator in motion (both K1 and K2 are closed). The two motors are permanent magnet motors (24 V, 120 W, 150 rpm) and they drive the (I_1) and (I_2) in counter-rotary motion, which simulates the rotation of the two wind turbines (E_1) and (E_2).

The air gap is of 4 mm and the diameter of the generator is 1 m. For both experiments the generator was droved with speeds corresponding to the wind speed of 0.5…4 m/s, respectively 9.5…76 rot/min. In order to start from a low speed, the inductor windings are supplied from a D.C. source with an excitation voltage of $U_{exc} = 10.5 \div 29.4$ V, and an excitation current of $I_{exc} = 0.5 \div 1.5$ A. The generator will deliver power to a resistive circuit with a value of $R_s = 2\Omega$. Figure 8.a presents the load diagram of the generator $U_{gen} = f(I_{exc})$ for the first experiment, with (I_1) fixed and (I_2) in rotary motion for speeds between 9.5 rot/min to 76 rot/min. It is noted that as the excitation current increases between $I_{exc} = 0.5 \div 1.5$ A, the voltage

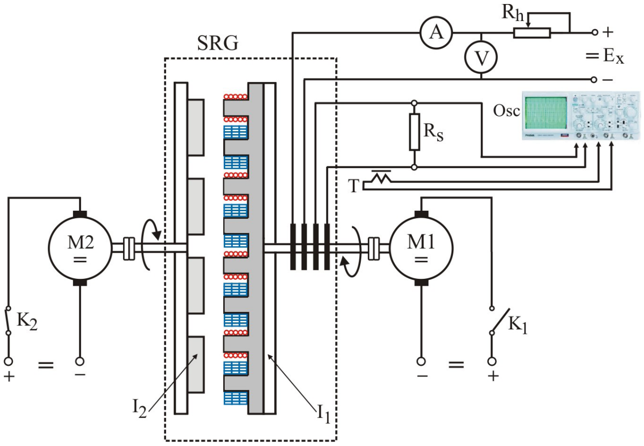

Figure 7. The schema of the experimental bench.

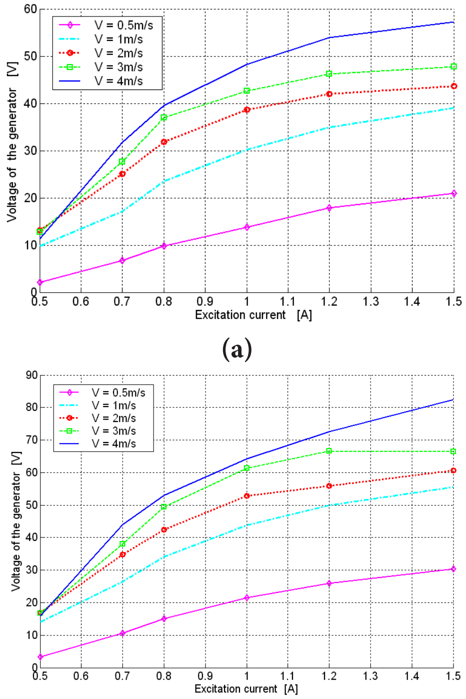

(a)

(b)

Figure 8. (**a**) Ugen = f(Iexc) characteristics for the simple rotary motion (**b**) Ugen = f(Iexc) characteristics for the counter-rotary motion.

at the terminals of the generator is also increasing to a maximum value corresponding to the saturation process of the magnetic circuit. The voltage is increasing also with the speed, having a minimum value of U_{gen} = 2.12V for an initial current of I_{exc} = 0.5 A and for a speed of 0.5 m/s (9.5 rot/min) and reaching a maximum value of U_{gen} = 57.26 V for I_{exc} = 1.5 A and for a speed of 4 m/s (76 rot/min). For an excitation current of 0.5 A and for the others speeds (from 1 m/s to 4 m/s) the voltage has narrow values of about 9.78…13.2 V.

Figure 8.b presents the load diagram of the generator $U_{gen} = f(I_{exc})$ for the second experiment, with (I_1) fixed and (I_2) in counter-rotary motion for the same speeds, between 9.5 rot/min to 76 rot/min. It is noted that for I_{exc} = 1.5A, the voltages at the terminals of the generator are higher than in the first experiment (considering the same speeds):

- for v_{wind} = 0.5 m/s, n = 9.5rot/min, I_{exc} = 1.5 A, it results U_{genI} = 20.91 V, U_{genII} = 30.31 V, so $U_{genI} < U_{genII}$;
- for v_{wind} = 1 m/s, n = 19 rot/min, I_{exc} = 1.5 A, it results U_{genI} = 39.08V, U_{genII} = 55.49V, so $U_{genI} < U_{genII}$;
- for v_{wind} = 2 m/s, n = 38 rot/min, I_{exc} = 1.5 A, it results U_{genI} = 43.6 V, U_{genII} = 60.6 V, so $U_{genI} < U_{genII}$;
- for v_{wind} = 3 m/s, n = 57 rot/min, I_{exc} = 1.5 A, it results U_{genI} = 47.8, U_{genII} = 66.4V, so $U_{genI} < U_{genII}$;
- for v_{wind} = 4 m/s, n = 76 rot/min, I_{exc} = 1.5 A, it results U_{genI} = 57.26V, U_{genII} = 82.45V, so $U_{genI} < U_{genII}$;
- U_{genI} is the voltage at the terminals of the generator for the first experiment;
- U_{genII} is the voltage at the terminals of the generator for the second experiment.

The experimental tests have been performed using a digital oscilloscope type LeCroy Wave Surf 400 with four channels. On the Channel 1 was measured the current of the generator on a resistive load with R_s=2Ω, by a Hall transducer LA55-P (with a ratio of 50A/50 mA). The waveform has been recorded with a measurement resistance of 100Ω, resulting a new ratio of 50A/5V. The output voltage at the terminals of the generator was measured by a voltage Hall transducer with a ratio of k = 500 (on Channel 2). Figure 9 presents four oscillograms with waveforms for voltage and current at different speeds of the induced circuit (I_2). For these tests the voltage and the current had the values U_{exc} = 10.5V, I_{exc} = 0.5A. Figure 9.a. presents the

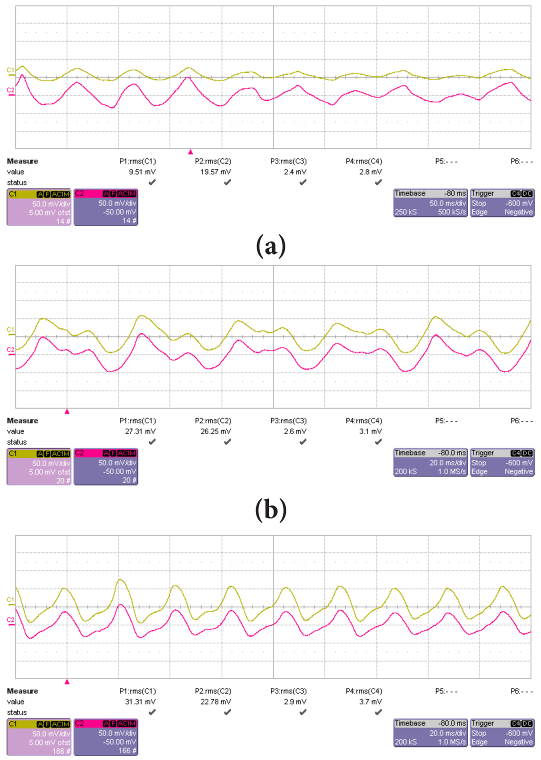

(a)

(b)

(c)

Figure 9. (**a**) Waveforms for a speed of 1 m/s. (**b**) Waveforms for a speed of 2 m/s. (**c**) Waveforms for a speed of 4 m/s.

waveforms for a speed of 1 m/s (19 rot/min for I_2). It is to notice a small value of the current $I_g = 0.15A$ for a voltage of $U_{gen} = 9.78V$. The waveforms are not sinusoidal and have important harmonics.

In Figure 9.b. the value of the current is increasing to 0.24A and the voltage to 13.12V. An important aspect is the fact that the waveform of the current is in phase with the waveform of the voltage because of the resistive load. The speed of the induced circuit (I_2) is of 2 m/s (28 rot/min). The last oscillogram (Figure 9.c.) has been recorded for a speed of 4 m/s (76 rot/min). The current increases to 0.33A and the voltage decreases from 12.7V to 11.39V. As above, both the output current and the output voltage of the generator are in phase.

5. Conclusions

A new type of Switched Reluctance Generator (SRG) for the low speed wind turbines with vertical or horizontal axle is presented. The solution generator-wind turbine is a direct-drive one and has two mobile parts which can be droved by two wind turbines in counter-rotary motion by the appropriate orientation of the blades. A test bench was achieved, with the two mobile parts driven by two electric motors with variable speed. Experimental data has been obtained and analyzed for two situations: first, when the mobile part (I_1) is stationary–fixed and the mobile part (I_2) is free to rotate and second, when both elements (I_1) and (I_2) are free to rotate in counter-rotary motion. Using the counter-rotary motion it results an important increasing of the output voltage of the generator for the same speed. Thus, the proposed direct-drive generator is more efficient that the classical structure with gears and the simple rotary motion.

Nomenclature

P - The specific power of the air flux;
$P_{turbine}$ - The power of the wind turbine;
ρ_{air} - The air density;
A - Swept area of the blades;
v_{wind} - The speed of the wind;
C_p - Power coefficient; the fraction of the wind power that is captured by wind turbine blades;
s - Turbine solidity;
λ - Tip speed ratio;
N - Number of the blades;
R_r - The radius of the rotor;
ω - The angular speed of the turbine;
$\overline{F}_n^*$ - The maximum normal force on the blade;
F_n^M - The maximum relative normal force on the blade for a rotation;
δ - The air gap of the generator;
l_a - The length of a simple magnetic circuit for flux closing;
τ_d - The tooth pitch;
τ_p - The pole pitch;
l_d - The width of a tooth;
l_c - The width of a notch;
S_{pvc} - The space of complete variation of the induced flux;
U - The terminal voltage;
I - The phase current;
R - The phase resistance;
Φ - The flux linkage;
P_{gen} - The power of the generator;
u_{exc} - Voltage supply on the inductive windings;
i_{exc} - The current in the inductive windings;
u_{gen} - The output voltage of the generator;
i_{gen} - The current on the terminals of the generator;

6. References

1. Li H, Chen Z. Overview of different wind generator systems and their comparisons. IET Renewable Power Generation. 2008; 2(2):123–38.
2. Polinder H, Bang DE, Li H, Chen Z. Concept report on generator topologies, mechanical and electromagnetic optimization. Project up Wind. 2007.
3. Zuher A, Mehrdad K. An analytical literature review of stand-alone wind energy conversion systems from generator viewpoint. Reneweable and Sustainable Energy Reviews. 2013; 28:597–15.
4. Polinder H, De Haan SWH, Dubois MR, Slootweg JG. Basic operation principles and electrical conversion systems of wind turbines. 4th Nordic Workshop on Power and Electronics and Drives; 2005; 15(4):43–50.
5. Darie E, Cepisca C. The use of Switched Reluctance Generator in wind energy applications. In: Hammons TJ, editors. 13th Renewable Energy, in Technology; 2007. p. 448–62.
6. Arifin A, Al-Bahadly IH, Mukhopadhyay SC. State of the Art of Switched Reluctance Generator. Energy and Power Engineering. 2012; 4:447-58.
7. Arifin A, Al-Bahadly I H. Switched reluctance generator for variable speed wind energy applications. Smart Grid and Renewable Energy. 2011; 2(1):227–36.
8. Plesca A, Scintee A. Testing of power electrical apparatus using modular high current source. IREE. 2010; 5(3):1218–24.

9. Plesca A. Busbar temperature monitoring and correlation with protection electrical apparatus. IREE. 2011; 6(5):2659–65.
10. Choi DW, Byun SI, Cho YH. A study on the maximum power control method of switched reluctance generator for wind turbine. IEEE Transactions on Magnetics. 2014; 50(1).
11. Bao YJ, Cheng KWE, Cheung NC, Ho SL. Experimental examination on a new switched reluctance wind power generator system for electric vehicles. IET Power Electronics. 2012; 5(8):1262–9.
12. Ajao KR, Mahamood MR, Iyanda MO. Interface for modeling the power output of a small wind turbine. Indian Journal of Science and Technology. 2009 May; 2(5).
13. Rajaji L, Kumar C. neural network controller based induction generator for wind turbine applications. Indian Journal of Science and Technology. 2009 Feb; 2(2).
14. Menon Parvathy V, Gnanambigai M. Stability analysis of the variable speed wind turbine using sliding mode control. Indian Journal of Science and Technology. 2015 Apr; 8(S7).
15. Yen J, Ahmed N. Improving safety and performance of small-scale vertical axis wind turbines. Procedia Engineering. 2012; 49:99–106.
16. Messineo Av, Culotta S. Evaluating the performances of small wind turbines: A case study in the South of Italy. Energy Procedia. 2012; 16:137–45.
17. Ilie V, Almasi L, Nedelcu S. Utilizarea energiei vantului. Tehnica, Bucuresti. 1984.
18. Patel MR. Wind and Solar Power Systems. New York: CRC Press; 1999.
19. Bostan I, Dulgheru V, Sobor Iv, Bostan V. Sisteme de conversie a energiilor regenerabile: Eoliana, solara, hidraulica. Tehnica-Info, Chisinau. 2007.
20. Martinez J. Modelling and Control of Wind Turbines. London, UK: Imperial College; 2007.
21. Barros TA, Dos S, Filho AJS, Filho ER. Direct Power Control for Switched Reluctance Generator. In: Muyeen M, (editor). Wind Energy, Modeling and Control Aspects of Wind Power Systems. USA: Intech; 2013.
22. Nassereddine M, Rizk J, Nagrial M. Switched reluctance generator for wind power applications. World Academy of Science, Engineering and Technology. 2008; 2(5):583–7.
23. Fiedler AJ, Tullis S. Blade offset and pitch effects on a high solidity vertical axis wind turbine. Wind Engineering. 2009; 33(3):237–46.

Indian Journal of Science and Technology, *Vol 9(40), DOI: 10.17485/ijst/2016/v9i40/88878, October 2016*

ISSN (Print) : 0974-6846
ISSN (Online) : 0974-5645

Force Estimation of an Asymmetrical Pantograph for Different Damper Positions

Dumitru Cuciureanu[1], Costica Nituca[2*] and Gabriel Chiriac[2]

[1]"Q" SRL Iasi, Stradela Sf. Andrei nr.13, Iasi, Romania; office@qsrl.ro
[2]Technical University "Gheorghe Asachi" Iasi, Faculty of Electrical Engineering,
Bd. D. Mangeron, nr. 21- 23, 700050 Iasi, Romania;
gchiriac@tuiasi.ro, costica_nituca@yahoo.com

Abstract

Objectives: To estimate the optimal position of the damper (resort) for an asymmetrical pantograph drive system used for electric trains supply. **Methods/Analysis:** Different solutions to attach the damper are studied, considering the pull bar position, and the equations accordingly to every solution are estimated. The pantograph is droved by a resort, but it could be used any other mechanism, like pneumatic or hydraulic drive system. **Findings:** These analyses can be used to identify the optimal position of the pull bar from the main axle of the pantograph, in order to find the optimal work area of the pantograph, with small variation of the contact force and with a better contact between the pantograph and the contact line. **Novelty/Improvement:** An asymmetrical pantograph model at a scale of 1/4 is used for experiments, considering the force variation for lifting and descending of the pantograph. For the situations when the resort is attached by a crank (above or below of the oscillation point), in the relation of the force it appears a new expression.

Keywords: Contact Force, Damper Position Optimization, Pantograph, Resort

1. Introduction

Different pantographs are currently used in train vehicles around the world. With the exception of the Shinkansen 500 series telescopic pantograph, all high-speed railway pantographs are of the two-stage type[1]. The main characteristic of a pantograph is to assure a good current collecting, without interruptions of the current regardless of the height of the pantograph. For this, it is necessary for the pantograph to have a contact plan irrespective of the movement of the mechanical articulated system, a small inertia, a good lateral and transversal stability, to obtain in static and dynamic regime a contact pressure irrespective of the string height, and have a low sensibility at the aerodynamics effects. More of this, the pantograph needs to have a crosshead slipper with an adequate shape and way of suspension for the contact characteristics. Its shape, size and fixation depend on the characteristics of the electric current, on the geometrical characteristics of the contact line[2] especially on the catenary irregularities which may cause serious fluctuation of contact force, even leading to the pantograph coming off the catenary[3].

In the general nonlinear model, the pantograph model is represented in terms of the following kinematic linkages: a lower frame arm, an upper frame arm and a head link. The entire mechanism is raised by a torque applied to a link of the arm. A frame suspension model provides an uplift force to the pantograph. The input force is assured by a suspension, usually a resort or pneumatic system (actuator) which acts horizontally, applying a torque to the lower arm. This input force may vary in time and has to overcome the weight of the mechanism but also must provide the uplift force against the wire[4]. In some cases there are used only dampers (resorts) to assure the uplift force, as for the pantograph for the Korean high speed train[5]. The model of the pantograph can be realized with two masses[6] with accent on the active control of the pantograph but also a model in three dimensions with the advantages to consider many hypothesizes[7].

Low contact forces may lead to loss of contact,

** Author for correspondence*

resulting in electric arcing and power interruptions. On the other hand, too large contact forces may cause rapid wear of the carbon skates. Moreover, the pantograph may exhibit unexpected motions even when the contact-force variation is kept within a reasonable range. Thus, vertical dynamics of the carbon-strip suspension is also studied with an aim of improving the reliability and safety of running trains[8]. The variation on the head suspension resort stiffness reflects factors related to operation conditions, maintenance and material degradation. The variation on the lower damper of the pantograph represents factors related to usage in service, degradation and lack of maintenance[9].

The pneumatic actuator is working typically at 3.5-4.5 barr and in order to obtain a constant transmission ratio from air pressure to static force between sliding surfaces, the geometry of coupling between the actuator and pantograph is optimized[10]. To improve the dynamical response of the pantograph are used different solutions according to the position of the active suspension stage of the pantograph: a) active suspension system between sliding bows and mobile frame and b) active actuator on the mobile frame, with a passive suspension system placed under sliding bows. The layout *b* is preferred usually because their shape has less effect on the aerodynamic behavior of the pantograph[10], has lesser limitation concerning shape, weight and is better protected from the harsh environmental conditions.

There are also studies regarding unconventional methods to supply the electric traction vehicles[11]. All these studies have to be considered having into attention the environmental friendly aspects of the different types of transportation systems, considering the large efforts to improve the quality of the emissions and to reduce the pollution over the medium[12].

With these considerations it is useful to study the resort/damper position according to the frame of the pantograph, in order to estimate the pantograph dynamics and forces.

2. Estimation of the Lifting Force of the Pantograph

First it is to estimate the vertical force F developed due to the resort R of the pantograph over the contact line CL depending on the high of the pantograph. To simplify, the pantograph is considered as a bar T with the weight *G*, length *l*, and jointed in the point O (Figure 1). In the point O_2 the bar is linked to the upper arm of the pantograph (Figure 2). The resort *R* with a length of $l_R = a + (b + x) + c$ drives the bar, where *x* is a variable. It is considered that there is no friction into the joints of the pantograph. The pantograph will have a vertical motion $v_{v.}$ (Figure 1)

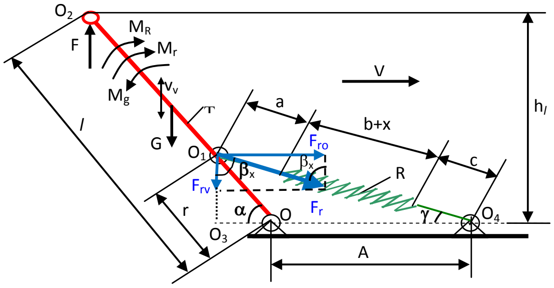

Figure 1. Kinematics of the asymmetrical pantograph.

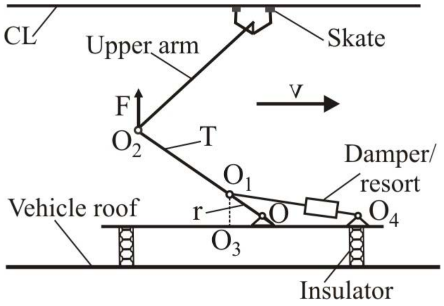

Figure 2. Simplified physical representation of the asymmetrical pantograph.

The torque due to the force G related to the point O is:

$$M_g = G\frac{l}{2}\cos\alpha \tag{1}$$

The torque M_r related to the point O due to the resort can be estimated starting from the force F_r given by the resort, composed from horizontal and vertical components, $\overline{F}_r = \overline{F}_{ro} + \overline{F}_{rv}$:

$$M_r = F_{ro} r \sin\alpha - F_{rv} r \cos\alpha \tag{2}$$

where $OO_1 = r$.

Considering $F_{ro} = F_r \sin\beta_x$ and $F_{rv} = F_r \cos\beta_x$ and replacing into the equation (2) it results:

$$\begin{aligned} M_r &= F_r r \sin\beta_x r \sin\alpha - F_r \cos\beta_x r \cos\alpha \\ &= F_r r\left(\sin\beta_x \sin\alpha - \cos\beta_x \cos\alpha\right) \end{aligned} \tag{3}$$

But $\cos\beta_x = \frac{r\sin\alpha}{k_1 + x}$ and $\sin\beta_x$

$$= \sqrt{1 - \frac{r^2\sin^2\alpha}{(k_1 + x)^2}} \text{with} k_1 = a + b + c$$

Replacing into equation (3):

$$M_r = F_r r\left[\sin\alpha\sqrt{1-\frac{r^2\sin^2\alpha}{(k_1+x)^2}}-\frac{r\sin\alpha}{k_1+x}\cos\alpha\right] \tag{4}$$

and

$$M_r = F_r r\sin\alpha\frac{1}{(k_1+x)}\left[\sqrt{(k_1+x)^2-r^2\sin^2\alpha}-r\cos\alpha\right] \tag{5}$$

In the triangle $O_1O_3O_4$

$$(k_1+x)^2 = r^2\sin^2\alpha+(r\cos\alpha+A)^2 \tag{6}$$

and

$$x=\sqrt{r^2\sin^2\alpha+r^2\cos^2\alpha+2Ar\cos\alpha+A^2}-k_1, \tag{7}$$

or

$$x=\sqrt{A^2+r^2+2Ar\cos\alpha}-k_1. \tag{8}$$

Replacing the value (k_1+x) into (5) it results the intermediate relation:

$$M_r = F_r r\sin\alpha\frac{1}{k_0+x}\left[\sqrt{r^2\sin^2\alpha+(r\cos\alpha+A)^2-r^2\sin^2\alpha}-r\cos\alpha\right]$$

Finally:

$$M_r=\frac{F_r rA\sin\alpha}{k_0+x} \tag{9}$$

The force of the resort is given by a relation as:

$$F_r = k_0x \tag{10}$$

where k_0 is a constant of the resort and x is the elongation of the resort. Thus:

$$M_r=\frac{F_r rA\sin\alpha}{k_1+x}=\frac{k_0xAr\sin\alpha}{k_1+x} \tag{11}$$

Replacing the value of x in (8):

$$\begin{aligned}M_r&=\frac{k_0Ar\sin\alpha\left(\sqrt{A^2+r^2+2Ar\cos\alpha}-k_1\right)}{\left(k_1+\sqrt{A^2+r^2+2Ar\cos\alpha}-k_1\right)}\\&=\frac{k_0Ar\sin\alpha\left(\sqrt{A^2+r^2+2Ar\cos\alpha}-k_1\right)}{\sqrt{A^2+r^2+2Ar\cos\alpha}}\end{aligned} \tag{12}$$

Considering by notation $A^2+r^2=m$ and $2rA=n$ it results:

$$\begin{aligned}M_r&=\frac{k_0Ar\sin\alpha\left(\sqrt{m+n\cos\alpha}-k_1\right)}{\sqrt{m+n\cos\alpha}}\\&=k_0Ar\sin\alpha\left(1-\frac{k_1}{\sqrt{m+n\cos\alpha}}\right)\end{aligned} \tag{13}$$

Summing the torques M_r and M_g:

$$\begin{aligned}M_R&=M_r+M_g=k_0Ar\sin\alpha\\&\left(1-\frac{k_1}{\sqrt{m+n\cos\alpha}}\right)-G\frac{1}{2}\cos\alpha\end{aligned} \tag{14}$$

The force due to the torque M_R into the point O_3 (Figure 3):

$$F=\frac{M_R}{l\cos\alpha}=\frac{k_0Ar\sin\alpha}{l\cos\alpha}\left(1-\frac{k_1}{\sqrt{m+n\cos\alpha}}\right)-\frac{G}{2} \tag{15}$$

Replacing $\frac{k_0Ar}{l}$ with k_2 it results:

$$F=k_2\sin\alpha\frac{1}{\cos\alpha}\left[1-\frac{k_1}{\sqrt{m+n\cos\alpha}}\right]-\frac{G}{2} \tag{16}$$

or

$$F=k_2\mathrm{tg}\alpha\left[1-\frac{k_1}{\sqrt{m+n\cos\alpha}}\right]-\frac{G}{2} \tag{17}$$

3. Resort Position for the Pantograph Drive System

The equation (17) shows the link between the force F of the pantograph acting on the contact line and the angle α, and the link between the force F and the height of the pantograph skate h_l because of the relation:

$$h_l = l\sin\alpha \tag{18}$$

The equation (17) has three elements:

$$1.)\quad k_2\mathrm{tg}\alpha;\quad 2.)\quad \frac{k_1k_2\mathrm{tg}\alpha}{\sqrt{m+n\cos\alpha}};\quad 3.)\quad \frac{G}{2}. \tag{19}$$

where:

$$\begin{aligned}m&=A^2+r^2 n=2Ar;k_2=\frac{k_0Ar}{l};k_3\\&=A-(a+b);k_4=\frac{k_0rk_3}{l};k_5=\frac{k_0r^2}{l}\end{aligned} \tag{20}$$

For a variation of the angle $\alpha = 0\ldots90^0$, the first and the second expressions vary in different ways, that is the vertical force F is not constant and depend on the high of the skate. Thus, it is not possible to have a perfect constant force by using a resort.

Thus, it is important to know which the best options to obtain a constant force are. In this situation, it is important to analyze the modalities to attach the resort on the bar of the pantograph related to a fixed point.

4. Possibilities for the Resort Drive System Attachment

In this chapter there are presented some solutions for the resort position which is attached between the pantograph bar and a fixed point. There are also presented the equations accordingly to every solution. The pantograph is considered as a simplified system with a bar supported by the roof of the locomotive and used to collect energy from the contact line. With the above conditions, it results different situations to attach the resort and the bar and we consider for the analysis 12 cases.

In the first case, in extension of the bar T, in the point O_1, there is a pull bar on length *r*. One of the resort ends is jointed in the point O_1, and the other end is fixed in the point O_4, at the distance A, in the same plane with the inferior arm *r*, which is, in the same time, the support and the joint point O of the bar of the pantograph. Considering the movement direction of the train (the direction of the speed of the vehicle *V*), we consider that the resort is placed "in front" of the pantograph.

In the second case, the pull bar r is in the same position as the in the first case, but the support and the joint point of the pantograph bar is the point O_1, in the extension of the bar T with the bar *r*. The resort is "behind" the pantograph.

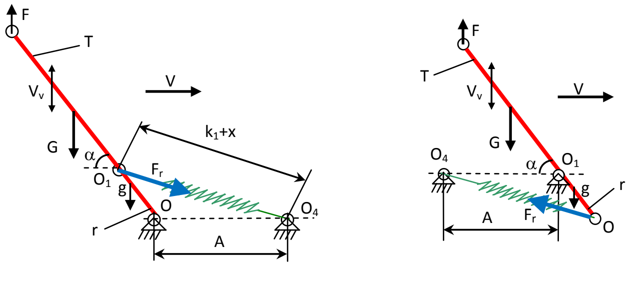

Figure 3. (a) 1st case: the resort is placed "in front" of the pantograph, (b) 2nd case: the resort is placed "behind" of the pantograph.

Considering the Figures 3(a) and 3(b):

$$1^{st}\text{ case: } F = k_2 tg\alpha - \frac{k_1 k_2}{\sqrt{m + n\cos\alpha}} tg\alpha - \frac{G}{2} \quad (21)$$

$$2^{nd}\text{ case: } F = k_2 tg\alpha - \frac{k_1 k_2}{\sqrt{m + n\cos\alpha}} tg\alpha - \frac{1}{2}\left(G - g\frac{r}{1}\right) \quad (22)$$

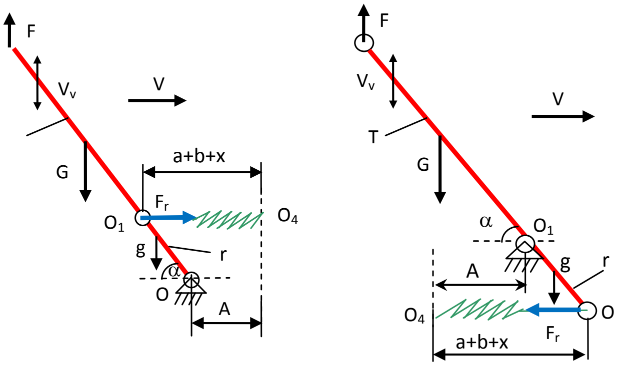

Figure 4. (a) 3rd case: the resort is horizontal and "in front" of the pantograph. (b) 4th case: the resort is horizontal and "behind" of the pantograph.

In the 3rd case the pull bar r is in the same position as in the first case, but the resort is jointed in horizontal plane "in front" of the pantograph. One of its ends is on the point O_1 and the other in the point O_4, at the distance *A*. In the 4th case the pull bar r is as in the second case, but the resort is horizontal and "behind" the pantograph, at the distance A from the support in O_1. Considering the Figures 4(a) and 4(b):

$$3^{rd}\text{ case: } F = k_4 tg\alpha + k_5 \sin\alpha - \frac{G}{2} \quad (23)$$

$$4^{th}\text{ case: } F = k_4 tg\alpha + k_5 \sin\alpha - \frac{1}{2}\left(G - g\frac{r}{1}\right) \quad (24)$$

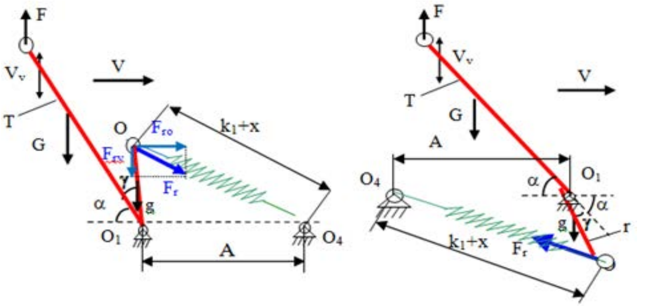

Figure 5. (a) 5th case: the pull bar r is "in front" and above of the pantograph, at an angle γ, (b) 6th case: the pull bar r is "in front" and below of the pantograph, at an angle γ.

In case 5 the pull bar *r* is rigid fixed on the inferior part of the bar T, in the point O_1 (a joint point for the bar T) "in front" of the pantograph at an angle γ (which is considered as constant) from the normal position of the pantograph (Figure 5(a)). At the other end of the bar *r*, in point O, is fixed an end of the resort *R*. The other end of the resort is fixed in point O_4.

In case 6 (Figure 5(b)) the pull bar *r* is in extension of the bar T, but at the angle γ. The resort has an end in the point O and the other in O_4, in the same plane with the point O_1.

5thcase
$$\begin{gathered} F = k_2 \frac{\sin(\alpha+\gamma)}{\cos\alpha} - \frac{k_1 k_2}{\sqrt{m + n\cos\alpha}} \\ \frac{\sin(\alpha+\gamma)}{\cos\alpha} - \frac{1}{2}G - \frac{g}{2}\frac{r}{l}\frac{\cos(\alpha+\gamma)}{\cos\alpha} \end{gathered} \tag{25}$$

6th case:
$$\begin{gathered} F = k_2 \frac{\sin(\alpha+\gamma)}{\cos\alpha} - \frac{k_1 k_2}{\sqrt{m + n\cos\alpha}} \\ \frac{\sin(\alpha+\gamma)}{\cos\alpha} - \frac{1}{2}G + \frac{g}{2}\frac{r}{l}\frac{\cos(\alpha+\gamma)}{\cos\alpha} \end{gathered} \tag{26}$$

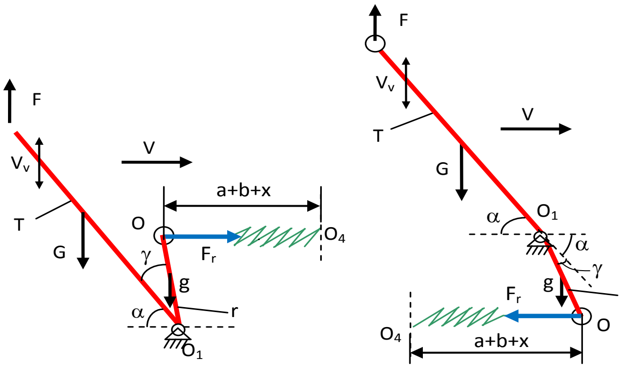

Figure 6. (a) 7th case: the pull bar is "in front" of the pantograph, at an angle γ, with horizontal resort, (b) 8th case: the pull bar is "behind" of the pantograph, at an angle γ, with horizontal resort.

In case 7 (Figure 6(a)) the bar *r* is as in the case 5, but the resort is horizontally placed "in front" of the pantograph between the point O and O_4, at a distance a + b + x.

In case 8 (Figure 6(b)) the bar *r* is as in the case 6, but the resort is horizontally placed "below" the pantograph, between the point O and O_4, at a distance a + b + x.

7th case
$$\begin{gathered} F = k_4 \frac{\sin(\alpha+\gamma)}{\cos\alpha} + k_5 \frac{\sin(\alpha+\gamma)}{\cos\alpha} \\ \cos(\alpha+\gamma) - \frac{1}{2}G - g\frac{r}{2l}\frac{\cos(\alpha+\gamma)}{\cos\alpha} \end{gathered} \tag{27}$$

8th case
$$\begin{gathered} F = k_4 \frac{\sin(\alpha+\gamma)}{\cos\alpha} + k_5 \frac{\cos(\alpha+\gamma)}{\cos\alpha} \\ \sin(\alpha+\gamma) - \frac{1}{2}G + \frac{1}{2}\frac{gr}{l}\frac{\cos(\alpha+\gamma)}{\cos\alpha} \end{gathered} \tag{28}$$

In case 9 the bar *r* is fixed in the point O_1, "behind" the pantograph and at the angle g from the normal position of the pantograph, as seen in Figure 7(a). In the point O is fixed one of the ends of the resort and the other is fixed in point O_4, "in front" of the pantograph, at distance A.

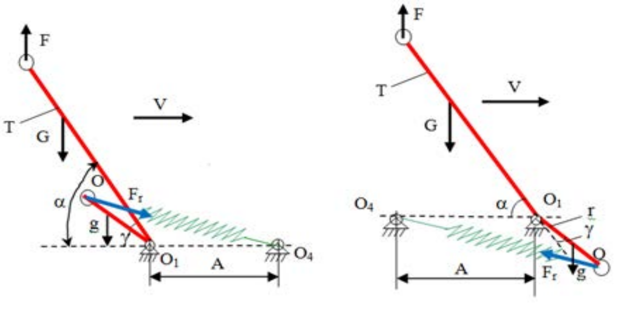

Figure 7. (a) 9th case: the pull bar is "behind" and above of the pantograph point O1, at an angle γ, (b) 10th case: the pull bar is "in front" and below of the pantograph point O1, at an angle γ

In case 10 (Figure 7(b)) the bar *r* is place in extension of the bar T "in front" of the pantograph at the angle g. The resort is fixed between the points O, below the pantograph, and the point O_4, in the same horizontal with the point O_1.

case 9:
$$\begin{gathered} F = k_2 \frac{\sin(\alpha-\gamma)}{\cos\alpha} - \frac{k_1 k_2}{\sqrt{m + n\cos(\alpha-\gamma)}} \\ \frac{\sin(\alpha-\gamma)}{\cos\alpha} - \frac{1}{2}\left[G + g\frac{r}{l}\frac{\cos(\alpha-\gamma)}{\cos\alpha}\right] \end{gathered} \tag{29}$$

case:10.
$$\begin{gathered} F = k_2 \frac{\sin(\alpha-\gamma)}{\cos\alpha} - \frac{k_1 k_2}{\sqrt{m + n\cos(\alpha-\gamma)}} \\ \frac{\sin(\alpha-\gamma)}{\cos\alpha} - \frac{1}{2}\left[G - g\frac{r}{l}\frac{\cos(\alpha-\gamma)}{\cos\alpha}\right] \end{gathered} \tag{30}$$

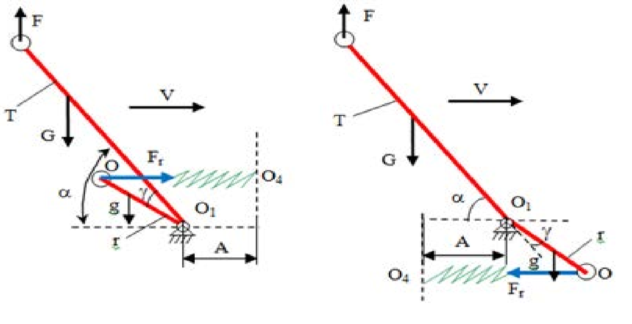

Figure 8. (a) 11th case: the pull bar is "behind" of the pantograph, at angle γ, with horizontal resort, (b) 12th case: the pull bar is "in front" of the pantograph, at angle γ with horizontal resort.

In case 11 (Figure 8(a)), the bar is placed as in the case 9, and the resort is placed horizontally “in front” of the pantograph. In case 12 (Figure 8(b)) the bar is placed as in the case 10 and the resort is placed horizontally “below” the pantograph.

case:11 $$F = k_4 \frac{\sin(\alpha-\gamma)}{\cos\alpha} + k_5 \frac{\sin(\alpha-\gamma)}{\cos\alpha} \cos(\alpha-\gamma) - \frac{1}{2}G - \frac{g}{2}\frac{r}{l}\frac{\cos(\alpha-\gamma)}{\cos\alpha} \quad (31)$$

Case:12 $$F = k_4 \frac{\sin(\alpha-\gamma)}{\cos\alpha} + k_5 \frac{\sin(\alpha-\gamma)}{\cos\alpha} \cos(\alpha-\gamma) - \frac{1}{2}G + \frac{g}{2}\frac{r}{l}\frac{\cos(\alpha-\gamma)}{\cos\alpha} \quad (32)$$

5. Simulations and Results

For the simulations there are considered the data[13]: l=0.510

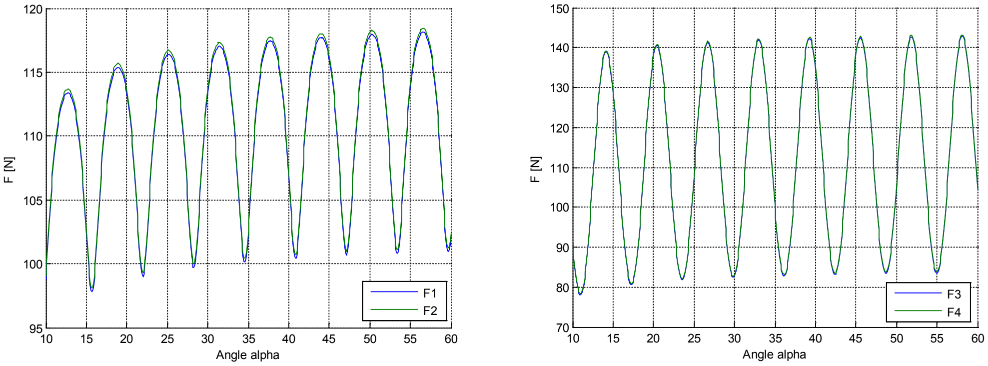

(a) 1st and 2nd cases. (b) 3rd and 4th cases.

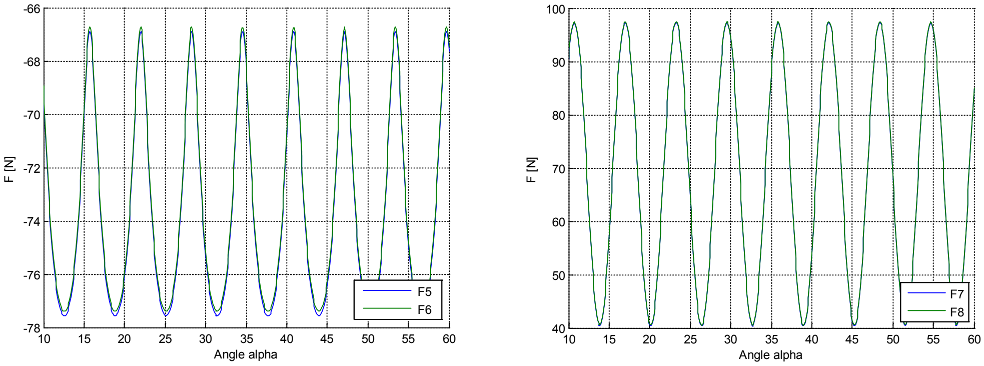

(c) 5th and 6th cases. (d) 7th and 8th cases.

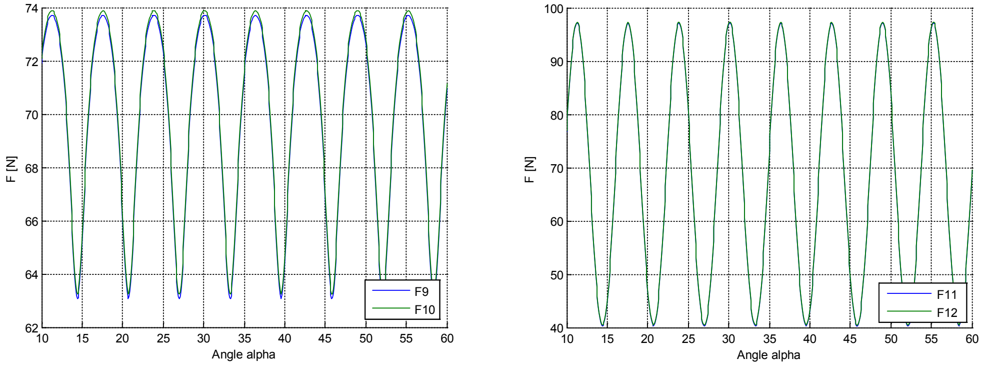

(e) 9th and 10th cases. (f) 11th and 12th cases.

Figure 9. Simulations for the vertical force in cases 1-12.

Table 1. Contact force values

	F_1 [N]	F_2 [N]	F_3 [N]	F_4 [N]	F_5 [N]	F_6 [N]	F_7 [N]	F_8 [N]	F_9 [N]	F_{10} [N]	F_{11} [N]	F_{12} [N]
Minimum values	97.8	98.09	78.11	78.4	-77.57	-77.4	40.35	40.52	63.06	63.23	40.28	40.45
Maximum values	118.1	118.4	142.9	143.2	-66.89	-66.7	97.27	97.44	73.72	73.89	97.28	97.29
Force variation	20.3	20.31	64.79	64.8	-10.68	-10.7	56.92	56.92	10.66	10.66	57.0	56.84

m; G=5.550 kg; a=0.01 m; b=0.255 m; c=0.01 m; x=0.225 m; $\alpha=600$; $\gamma=50$; r=0.55 m; A=1.650 m; k_0=50Ns/m; g=0.550 kg. The results of the simulations are presented in Figure 9 and Table 1.

The pantograph has a movement close to a sinusoid. To avoid large amplitudes and the detachments from the contact wire, the pantograph has to assure the maximum and minimum amplitude of the sinusoid. These values depend on the position of the pull bar and of the resort drive system. Analyzing the simulations in Figure 9 and the values in table 1, we can conclude:

a. The forces have positive values, except the case 5 and the case 6

b. There are three groups according to the variation of the force:

- Large variation of the force, with the cases 3rd (64.79N), 4th (64.8N), 7th (56.92N), 8th (56.92N), 11th (57N) and 12th (56.84N); these cases cannot be considered because the variation of the force is to large, which gives a delayed reaction time for the pantograph in order to follow the trajectory of the contact wire;
- Medium variation of the force, with the cases 1st (20.3N) and 2nd (20.31N). These cases could be considered for the pantograph system drive, because the reaction time is lower and the skate of the pantograph can easily follow the trajectory of the contact wire; and
- Small variation of the force, with the cases 9th (10.66N), 10th (10.66N), 5th (-10.68N) and 6th (-10.7N). In these situations there are two cases with positive values and two with negative values. In practice, this can be realized by replacing the expansion resort with a compression one, with the same mechanical parameters. In these cases the reaction times are low assuring a good contact between the skate and the contact wire. These solutions are to be recommended for the pantograph drive system.

c. The medium value for the maximum forces considering all the twelve cases is 99.42 N, while the medium value for the minimum forces is 66.27 N.

6. Test bench Experiments

A practical analysis is made considering the force variation on lifting and descending of the pantograph. From the 12 cases presented above we consider two cases, the 4th case and the 9th case, because they have the resort horizontal and "behind" the pantograph, at the distance A from the support in O1 (case 4), and the bar r is fixed "behind" the pantograph and at the angle γ from the normal position of the pantograph, but in the point O is fixed one of the ends of the resort and the other is fixed in point O4, "in front" of the pantograph, at distance A (case 9).

For these two extreme situations there are determined the static characteristic F =f(α) of the pantograph for lifting and descending, considering a bench stand as in Figure 10. An asymmetrical pantograph (1) at a scale of ¼ as regarding a real system. The pantograph has two graphite skates (2) and the classical mechanical lifting (resort) system (3) used for the main lifting force. The pull bar *r* could be placed in different positions, (4) and (5), "in front" and "behind" of the pantograph in order to analyze the considered positions.

The pantograph model has a low inertia, a good lateral stability, a constant contact pressure for a specific high and a low wear of the graphite skate.

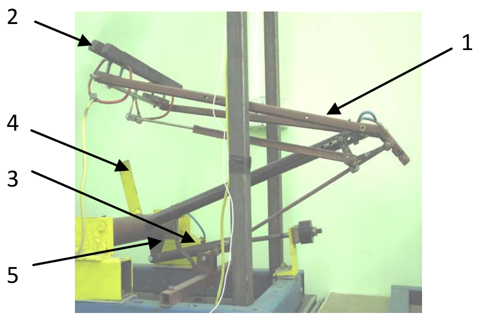

Figure 10. The asymmetrical pantograph used for the experimental tests.

Figure 11 presents the static characteristics F =f(α) for the 4th case. The experimental characteristic has a maximum of 145 N for lifting and 144 N for descending, while the minimum values are 76 N for lifting and 74 N for descending. It is to observe the difference of 2 N between the lifting force and descending force. Comparing with the simulations for the 4th case, the difference is about 1.8 N for the maximum force and 4.4 N for the minimum force.

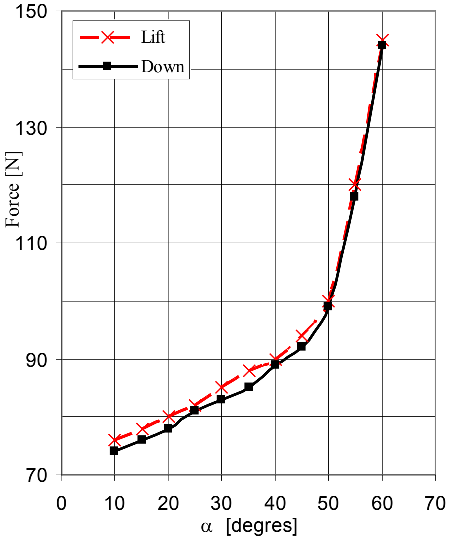

Figure 11. The static characteristic F =f(α) for the 4th case.

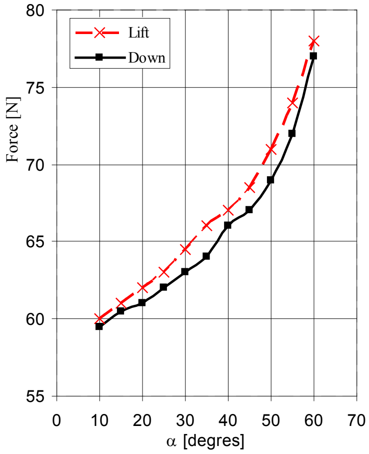

Figure 12. The static characteristic F =f(α) for the 9th case.

Figure 12 presents the static characteristics F =f(α) for the 9th case. The experimental characteristic has a maximum of 78 N for lifting and 77 N for descending, while the minimum values are 60 N for lifting and 59.5 N for descending. The difference between the lifting force and descending force is maximum 1N. Comparing with the simulations, the difference is about 4.28 N for the maximum force and 3.56 N for the minimum force.

It is to say that these analyses can be used to identify the optimal position of the pull bar from the main axle of the pantograph, in order to find the optimal work area of the pantograph, with small variation of the contact force and with a better contact between the pantograph and the contact line.

7. Conclusions

One of the current collecting problems is to assure a permanent contact between the pantograph and the contact line but without using too high forces. Knowing the relation between the contact force and the high of the skate of the pantograph gives the possibility to estimate the place to attach the resort on the pantograph's bar.

In the cases 1, 2, 5, 6, 9, 10 the resort is attached in a slanting way. In the cases 3, 4, 7, 8, 11, 12 the resort is horizontal attached for every high of the pantograph. To estimate the influence of the resort position related to the oscillation point in the cases 1, 3, 5, 7, 9, 11 the resort is attached above of the oscillation point and in cases 2, 4, 6, 8, 10, 12 it is attached below the oscillation point. Analyzing the 12 cases we can conclude:

- If the resort is attached above of the oscillation point all the coefficient of the trigonometrically functions are the same;
- The contact force variation depends strongly by the position of the resort: if the resort is horizontal (above or below of the oscillation point) the variation curve is the same.
- For the situations when the resort is attached by a crank (above or below of the oscillation point), in the relation of the force it appears a new expression.
- The 9th case offers a low variation of the force, assuring a better power collecting for the vehicle.

It is to mention that the pantograph is droved by a resort, but it could be used any other mechanism, like pneumatic or hydraulic drive system.

8. References

1. Ambrosio J, Pombo J, et al. A computational procedure for the dynamic analysis of the catenary-pantograph interaction in high-speed trains. *Journal of Theoretical and Applied Mechanics, Warsaw.* 2012; 50(3):681-99.
2. Niţucă C, Rachid A, et al. Constructive and experimental aspects regarding the electric power collecting for very high speed train. *Analele Univ. Din Craiova.* 2007; 31(II):290-93.

3. Qin Y, Zhang Y, et al. An analysis method for correlation between catenary irregularities and pantograph–catenary contact force. *J. Cent. South Univ*. 2014; 21:3353-60.
4. Eppinger SD, O'Connor DN, Seering WP, Wormley DN. Modeling and experimental evaluation of asymmetric pantograph dynamics. *Transactions of the ASME*. 1988; 110:168-74.
5. Eom BG, Mok JY, Lee HS. Influencing Factors on Dynamic Characteristics of Pantograph of Korean High Speed Train. *IJR Int. Journal of Railway.* 2009; 2(4):187-92.
6. Rachid A. Pantograph Catenary Control and Observation using the LMI Approach. In: *50th IEEE Conference on Decision and Control and European Control Conference (CDC-ECC)* Orlando, FL, USA, 2011, p.2287-92.
7. Lee JH, Kim YG, et al. Performance evaluation and design optimization using differential evolutionary algorithm of the pantograph for the high speed train. *Journal of Mechanical Science and Technology.* 2012; 26(10):3253-60.
8. Huan RH, Zhu W, et al. Vertical dynamics of a pantograph carbon-strip suspension under stochastic contact-force excitation. *Nonlinear Dyn*. 2014; 76:765-76.
9. Pombo J, Ambrósio J. Influence of pantograph suspension characteristics on the contact quality with the catenary for high speed trains. *Computers and Structures*. 2012; 110-111:32-42.
10. Allotta B, Pugi P, Bartolini F. An active suspension system for railway pantographs: the T2006 prototype. *J. Rail and Rapid Transit. Part F.* 2009; 223:15-29.
11. Plesca A. Electric arc power collection system for electric traction vehicles. *International Journal of Electrical Power & Energy Systems*. 2014; 57: 212-21.
12. Satyanarayana Murthy YVV, Sastry GRK, Satyanaryana MRS. Experimental Investigation of Performance and Emissions on Low Speed Diesel Engine with Dual Injection of Solar Generated Steam and Pongamia Methyl Ester. *Indian Journal of Science and Technology*. 2011 Jan; 4(1):29-33.
13. Nituca C. Probleme de captare a curentului de la linia de contact pentru vehicule acţionate electric (in Romanian), Doctoral thesis, Technical University of Iasi, Romania, 2003.

Appendix 1

Nomenclature

A - Distance between the jointed point O1 and the jointed point of the resort, O4.

a, b, c – Constant parameters of the resort;

F – Vertical force due to the resort of the pantograph;

F_r – Force due to the resort;

F_{r0} , F_{rv} – Horizontal and vertical components forces for the force F_r;

G – Weight of the inferior arm of the pantograph;

g – Mass of the pull bar when the resort is not attached directly to the inferior arm;

h_l – High of the skate;

k_0 – Elastic constant of the resort;

$k_1 = a + b + c$ - Elongation of the resort;

x – Variable parameter of the resort;

l – Length of the inferior arm of the pantograph;

M_g – Torque due to the weight of the inferior arm of the pantograph;

M_r – Torque due to the resort;

M_R - the resultant torque;
r – Length of the pull bar.

Indian Journal of Science and Technology, *Vol 9(40), DOI: 10.17485/ijst/2016/v9i40/86736, October 2016*

ISSN (Print) : 0974-6846
ISSN (Online) : 0974-5645

Critical Speed Impact over the Pantograph-Catenary System's Behaviour

Gabriel Chiriac[1], Dumitru Cuciureanu[2] and Costica Nituca[1]*

[1]Technical University "Gheorghe Asachi" Iasi, Faculty of Electrical Engineering, Bd. D. Mangeron, nr. 21- 23,
Iasi - 700050, Romania; gchiriac@tuiasi.ro, costica_nituca@yahoo.com
[2]"Q" SRL Iasi, Stradela Sf. Andrei nr.13, Iasi, Romania; office@qsrl.ro

Abstract

Objectives: To estimate the impact of the critical speed over the power collecting system for the electric trains. **Methods/Analysis**: Two models regarding the critical speed estimation related to the resonance phenomenon in the pantograph-catenary system are studied: firstly, by the differential equation of the contact point trajectory, and secondly by the maximum kinetic energy and the maximum potential energy over a span. Simulations for the pantograph-catenary interaction at train speeds close to the critical ones are done. Tests for different speeds were realised on an experimental stand. **Findings:** Records of the pantograph-catenary system's behavior show the influence of the critical speeds over the power collecting system and knowing the critical speeds on different trucks, it can be established the maximum speeds for the railway vehicles. It is to observe that the critical speed depends strongly on the mechanical tensions in the contact line and on the linear mass of the contact line. **Applications/Improvements**: Two relationships were established for the critical speed, one considering mechanical tension into the wire and another considering the length span. A test bench was developed for the pantograph-catenary researches.

Keywords: Critical Speed, Electric Trains, Pantograph-Catenary Interaction, Test Bench

1. Introduction

The pantograph-catenary system assures all along the track the power supply for the traction motor and for the equipment of the electric trains. The catenary system is used from the beginning of the electric railway, being an efficient system, but it has some drawbacks. As the train speed increases, the current collecting complexity increases too, due to some parameters such as: speed, train vibrations, catenary oscillations, aerodynamics, the catenary and pantograph construction, etc[1]. The problems regarding the contact between the pantograph and the contact wire are largely studied in the literature with important results, considering the pantograph-catenary models and simulations[1,2]. In[3] it is assumed that the contact occurring between contact strip and contact wire is mostly influenced by the dissipated power at the contact due to arcing, friction effect and Joule effect. Thermal problems of the contact are also important, in order to avoid the over-heating due to the high currents, being necessary to consider the analysis of the thermal model of electric contacts in electric rails system[4,5].

A limitation of the operational speed of trains is the wave propagation velocity on the contact wire C[6], given by the relation $C = \sqrt{\left(\pi^2 E \big/ \rho L^2\right) + \left(T/\rho\right)}$, where T is the tension of the contact wire, ρ is the contact wire mass per length unit, EI is the beam bending stiffness and L is the beam length. For high-speed catenaries, the second term of the relation dominates the critical speed and the first term becomes negligible. When the train speeds approach the wave propagation velocity of the contact wire, the contact between the pantograph and the catenary is harder to maintain due to the increasing in the amplitude of the catenary oscillations and to the bending effects. In order to avoid the deterioration of the contact quality, the current regulation imposes a limit to the train

---

**Author for correspondence*

speed of $V = 0.7C$[6]. Even for the foundation of the truck there are studies on the critical speeds, as in[7,8].

These critical speeds (above 200 m/s)[7] are higher than for the contact wire but the results have direct application on estimates of ground vibrations induced by high-speed trains, and permit to evaluate the level of the additional loading factor to which high speed trains and tracks must be designed. Normally, train speed is less than 70% of the wave speed of the contact wire. If the vehicle's operation speed approaches to the wave speed of the contact wire, the probability of loss of contact is increased. Because of this loss of contact accompanying electric arcs between them, the current collector system becomes seriously damaged. Therefore, it is very important to maintain a stable contact force between the catenary and the collector plate of the pantograph. Because of the increasing interest in high-speed railway vehicles, the dynamic interaction between the catenary and the pantograph at high speeds has been studied extensively[9]. There are also studies regarding unconventional methods to supply the electric traction vehicles[10].

To study the pantograph-catenary interaction in real conditions, that is on trains, is difficult due to the high costs, the perturbation of the trains schedule, the necessity to adapt the current collecting system to the necessity of the data acquisition. This is why there are used test benches for the researches[11] using different systems for the pantograph-catenary interaction structure.

In this paper we realise an analysis of the critical speed for the pantograph-catenary system considering different relations to estimate it. It is analyzed the mathematical model of the interaction pantograph-catenary by simulations at the speeds of the train close to the critical speeds. On an experimental stand it is analyzed the interaction pantograph-catenary at critical speed.

2. Critical Speed Estimation

2.1 Critical Speed Estimation considering the Trajectory of the Contact Point

For the pantograph-catenary system it is important to estimate the differential equation of the trajectory of the contact point, with some simplified assumptions[12,13]:

The pantograph-catenary structure is considered to be a system with elastic masses which are placed vertically, one above another; the contact force will determine the variation of the height of the contact point linked to the kinetic energy of the masses. It is considered that the pantograph-catenary system has only one degree of freedom, which is in vertical direction;

There are neglected the dynamic forces due to the vibrations;

It is neglected the friction force between the contact wire and the skate of the pantograph;

It is neglected the aerodynamic influence (the air drag, the lateral wind);

The stiffness of the contact wire has a sinusoidal variation along a span;

The contact force due to the mechanical system of the pantograph (the spring) is constant.

Even considering these hypotheses, it is difficult to establish a mathematical model that reflects the phenomenon in its all complexity, because there are many parameters to estimate. Figure 1 presents the simplified model for the catenary and the pantograph.

The mathematical model is described by the next relationships[14]:

- For the vertical movement of the catenary:

$$m_c v^2 \frac{d^2 y}{dx^2} + b_c \frac{dy}{dx} = F_k - k_c y \tag{1}$$

For the vertical movement of the pantograph:

$$m_p v^2 \frac{d^2 y}{dt^2} = F_0 - F_k \tag{2}$$

From the equations (1) and (2) it results the differential equation of the trajectory of the contact point:

$$\left(m_c + m_p\right) v^2 \frac{d^2 y}{dx^2} + b_c \frac{dy}{dx} + k_c y = F_0 \tag{3}$$

Considering a sinusoidal variation over a span length for the mass of the catenary m_c and the stiffness coefficient k_c:

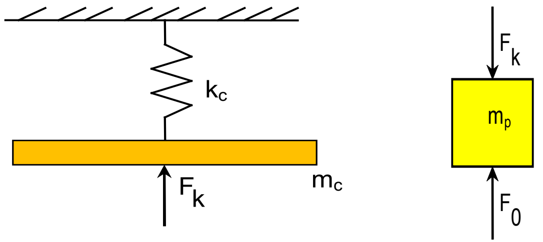

(a) (b)

Figure 1(a). The catenary model. (**b**). The pantograph model.

$$m_c = m_{c0}\left(1-\alpha_m \cos\frac{2\pi}{L}x\right),$$

$$k_c = k_{c0}\left(1-\alpha_k \cos\frac{2\pi}{L}x\right) \tag{4}$$

where the coefficient of irregularity of the mass of the catenary α_m and the coefficient of irregularity of the stiffness of the catenary α_k are given by:

$$\alpha_m = \frac{m_{\max} - m_{\min}}{m_{\max} + m_{\min}}, \ \alpha_k = \frac{k_{\max} - k_{\min}}{k_{\max} + k_{\min}}, \tag{5}$$

and

$$M = \left[m_{c0}\left(1-\alpha_m \cos\frac{2\pi}{L}x\right) + m_p\right]. \tag{6}$$

The differential equation (3) becomes:

$$Mv^2\frac{d^2y}{dx^2} + b_c\frac{dy}{dx} + k_{c0}\left(1-\alpha_k \cos\frac{2\pi}{L}x\right)y = F_0\,. \tag{7}$$

For the estimation of the critical speed it is proposed the solution[14,15]:

$$y = a_0 + a_1\cos\frac{2\pi}{L}x + b_1\sin\frac{2\pi}{L}x \tag{8}$$

with:

$$\left.\begin{aligned}
a_0 &= \frac{F_0}{k_{c0}} + \frac{\alpha_k^2 F_0\left(k_{c0} - Mv^2\dfrac{4\pi^2}{L^2}\right)}{b_c^2 v^2\dfrac{4\pi^2}{L^2} + \left(k_{c0} - Mv^2\dfrac{4\pi^2}{L^2}\right)^2}\\
a_1 &= \frac{\alpha_k^2 F_0\left(k_{c0} - Mv^2\dfrac{4\pi^2}{L^2}\right)}{b_c^2 v^2\dfrac{4\pi^2}{L^2} + \left(k_{c0} - Mv^2\dfrac{4\pi^2}{L^2}\right)^2}\\
b_1 &= \frac{\alpha_k^2 F_0 b_c^2 v\dfrac{4\pi}{L}}{b_c^2 v^2\dfrac{4\pi^2}{L^2} + \left(k_{c0} - Mv^2\dfrac{4\pi^2}{L^2}\right)^2}
\end{aligned}\right\} \tag{9}$$

Considering the damping coefficient of the catenary as $b_c = 0$, it results $b_1=0$, and the relation (8) becomes:

$$y = a_0 + a_1\cos\frac{2\pi}{L}x \tag{10}$$

The formula for the critical speed v_k results considering the conditions when the coefficient a_0 and a_1 become infinite (and also y). These conditions are fulfilled if the denominator of the a_0 and a_1 from the equation (9) are zero[14].

The relation for the critical speed is:

$$v_k = \frac{L}{2\pi}\sqrt{1-\frac{1}{2}\alpha_k^2}\cdot\sqrt{\frac{k_{c0}}{M + m_{c0}\left(1-\dfrac{\alpha_m\alpha_k}{2}\right)}}\,. \tag{11}$$

2.2 Estimation of the Critical Speed Considering the Kinetic Energy and the Potential Energy of the Contact Wire

Another possibility to analyze the critical speed is based on the analysis of the maximum kinetic energy, respective the maximum potential energy for a length L of a span for the vertical movement of the pantograph-catenary system, neglecting the influence of the dissipative forces. Thus, during the oscillations due to the force F_0 of the springs of the pantograph (which will lift the contact wire), the contact wire could be considered to have a parabola shape.

Thus, the total kinetic energy E_c, corresponding to the vertical movement of the catenary mass m_{c0} on the span length L, will be depicted as,

$$E_c = \frac{1}{2}2\int_0^{\frac{L}{2}}\left(\frac{dh}{dt}\right)^2\frac{d}{dx} \tag{12}$$

where dh/dt represents the speed of motion of the mass of the catenary $m_{c0}dx$ at the distance x from the centre.

According to the Figure 2, for the lifting h of a point from the contact line placed at the distance x from the middle of the span:

$$h = h_0\left(1-\frac{4}{L^2}x^2\right) \tag{13}$$

The oscillation of the contact line is considered to be a harmonic one[16]:

$$h_0 = h_{0\max}\sin\omega t \tag{14}$$

where h_{0max} is the amplitude of the oscillation in the middle of the span.

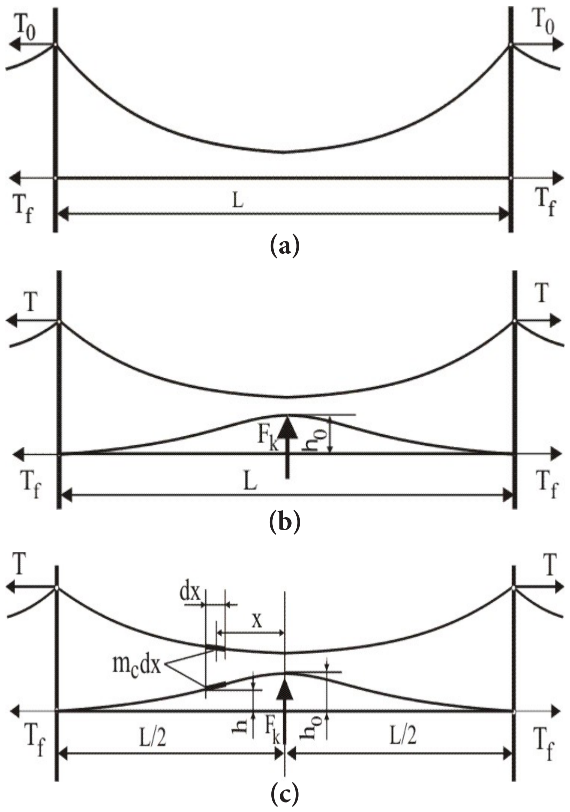

Figure 2. The forces acting on the catenary. **(a)** The catenary at standstill. **(b)** The shape of the catenary when the pantograph is on the middle of the span. **(c)** Catenary analysis for a distance *x* from the middle of the span.

It is considered that the value of the maximum kinetic energy occurs when the contact wire passes through horizontal position ωt = kπ, (k = 0,1,2…). In these conditions, the maximum kinetic E_{cmax} energy equation will be written as:

$$E_{c\max} = \int_0^{\frac{L}{2}} m_{c0}\left(\omega h_{0\max}\left(1-\frac{4}{L^2}x^2\right)\right)^2 dx = \frac{4}{15} m_{c0} L h_{0\max}^2 \omega^2 \quad (15)$$

The maximum potential energy corresponds to the maximum value of the catenary displacement, which is for ωt =π/2+ kπ. If the force of motion F_0 is a function of h_0, the maximum potential energy will be:

$$E_{p\max} = \int_0^{h_{\max}} F_0 dh_0 \quad (16)$$

There are considered two situations:

$$\text{a) } F_0 = h_0 \frac{4\left(T_0 + T_f\right)}{L}\frac{1}{\xi}, \quad (17)$$

where ξ is a damping coefficient due to the sectional static stiffness.

For $T = T_0$ it is established as ξ =*1*.

$$\text{b) } F_0 = \frac{h_0}{y_0}, \quad (18)$$

where $y_0 = (\xi \cdot L)/(4 \cdot (T_0 + T_f))$ is considered constant, independent of F_0.

For the first case, the potential energy relationship can be written in the form of:

$$E_{p\max} = \frac{4\left(T_0+T_f\right)}{L}\frac{1}{\xi}\int_0^{h_{\max}} h_0 dh_0 = \frac{2\left(T_0+T_f\right)}{\xi L} h_{0\max}^2, \quad (19)$$

and for the second case:

$$E_{p\max} = \frac{1}{y_0}\int_0^{h_{\max}} h_0 dh_0 = \frac{1}{2y_0} h_{0\max}^2 \quad (20)$$

Taking into account the equations (15) and (19), and the equations (15) and (20), it results

$$\frac{4}{15} m_{c0} L h_{0\max}^2 \omega^2 = \frac{2\left(T_0+T_f\right)}{\xi L} h_{0\max}^2 \quad (21)$$

and

$$\frac{4}{15} m_{c0} L h_{0\max}^2 \omega^2 = \frac{1}{2y_0} h_{0\max}^2 \quad (22)$$

with $\omega = \sqrt{\frac{15}{2}\frac{\left(T_0+T_f\right)}{\xi m_{c0} L^2}}$, and ξ =*1*.

The frequency of the free oscillations can be described by:

1. Considering mechanical tension into the wires:

$$v_{(a)} = \frac{0{,}436}{L}\sqrt{\frac{T_0+T_f}{m_{c0}}} \quad (23)$$

2. Considering the length of the span:

$$v_{(b)} = 0{,}218\sqrt{\frac{1}{m_{c0} L y_0}} \quad (24)$$

Under these circumstances, critical speed can be described with the following relation:

$$v_{cr(a)} = L v_{(a)} = 0{,}436\sqrt{\frac{T_0+T_f}{m_{c0}}}, \quad (25)$$

or

$$v_{cr(b)} = L v_{(b)} = 0{,}218\sqrt{\frac{L}{m_{c0} y_0}} \quad (26)$$

Since the stiffness from a span to another are different, (it is minimum in the front of the pillars and maximum in the middle of the span), when the pantograph passes under the contact wire, especially at high speed, the wire is influenced by a mass force given by the alternative motions of the pantograph, resulting an oscillation of the wire[16]. In the case of the sinusoidal trajectory, for the low speed of the trains, the force of inertia is variable between minimum at the front of the pillars and maximum in the middle of the span. Considering the same simplified assumptions as above, in Figure 3 it is presented a model[17-19], for the interaction between the pantograph and the catenary.

The mechanical parameters characterizing the pantograph-catenary interaction in Figure 3 have periodic variations along a span and can be described by the relationships (27), which represent a Fourier series of the parameters of the catenary, considering the second and the third harmonics:

$$\left.\begin{aligned} m_c(t) &= m_{c0} + \sum_{i=1}^{3} m_{ci} \cos\left(\frac{2i\pi}{L}x(t)\right) \\ b_c(t) &= b_{c0} + \sum_{i=1}^{3} b_{ci} \cos\left(\frac{2i\pi}{L}x(t)\right) \\ k_c(t) &= k_{c0} + \sum_{i=1}^{3} k_{ci} \cos\left(\frac{2i\pi}{L}x(t)\right) \end{aligned}\right\} \qquad (27)$$

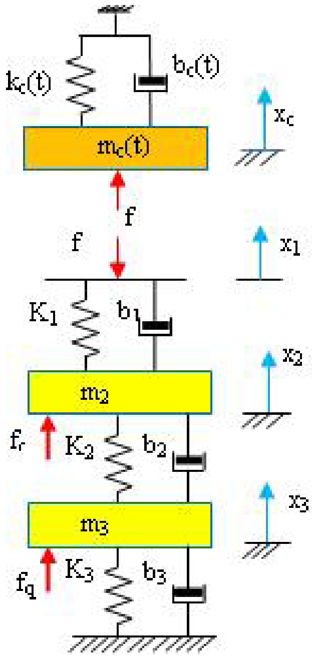

Figure 3. The model of the pantograph-catenary interaction.

The contact force acting on the elastic system pantograph-catenary can be described by[17]:

$$f = \max\{k_1(x_2 - x_1) + b_1(\dot{x}_2 - \dot{x}_1), 0\} \qquad (28)$$

During the transfer of the electric current from the contact wire to the pantograph, it is considered that the pantograph is in permanent contact with the wire $x_1 \equiv x_c$ and thus, the contact force *f* will have positive values. In this context, according to the Figure 3, it can be written:

$$\left.\begin{aligned} & m_c(t)\ddot{x}_1 + b_c(t)\dot{x}_1 + k_c(t)x_1 = k_1(x_2 - x_1) + b_1(\dot{x}_2 - \dot{x}_1) \\ & m_2\ddot{x}_2 + b_2\dot{x}_2 + k_2x_2 = k_2x_3 + b_2\dot{x}_3 + f_c(t) - k_1(x_2 - x_1) + b_1(\dot{x}_2 - \dot{x}_1) \\ & m_3\ddot{x}_3 + (b_2 + b_3)\dot{x}_3 + (k_2 + k_3)x_3 = k_2x_2 + b_2\dot{x}_2 + f_q(t) \end{aligned}\right\} \qquad (29)$$

where $y(t) = f(t)$ is the contact force.

3. Simulations of the Pantograph-Catenary System for Critical Speeds

For a comparative analysis of the critical speeds established by the relations (11) and (26), there are considered the parameters with the following values: m_{c0} = 195 kg, m_p = 17.1 kg, k_{c0} = 7000 N/m, α_m = 0.95, α_k = 0.95, $T_0 = T_f$ = 20 kN, h_0 = 0.35 m, L= 60 m. The speeds are denoted as v_{k1} for the relation (11), v_{k2} for the relation (26).

The maximum values of the critical speeds are estimated as: v_{k1max} = 73.92 m/s (266 km/h) and v_{k2max} = 69.44 m/s (233.7 km/h) shown in the Figure 4.

It is to observe a low difference between the critical speeds values, resulting that the vehicle could run safely on such a contact line with lower speeds than the critical

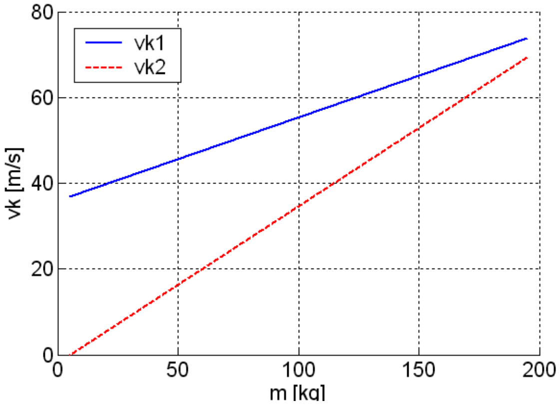

Figure 4. Variation of the critical speed V_k depending on the linear mass m_c.

one. It has considered as reference speed the values for v_{k1} the Equation (11). So, it has been computed the errors for the speed v_{k2} which uses the Equation (26). From the errors computation it results for formula (26) the error $\varepsilon_1 = \pm \frac{v_{k2} - v_{k1}}{v_{k1}} \cdot 100\% = -6.06\%$, which is a low value.

It is also to observe that the critical speed depends strongly on the mechanical tensions in the contact line and on the linear mass of the contact line. Thus, an increasing of the tension will result in an increase of the critical speed. The critical speed also depends on inverse ratio with the mass of the catenary. The oscillations of the contact line at the critical speed can be analyzed considering the model in Figure 3, the relations in (27) and the parameters with the following values: $m_{c0} = 195kg$, $m_{c1} = 100kg$, $m_{c2} = 20kg$, $m_{c3} = 5kg$, $b_{c0} = 240Nm^{-1}s$, $b_{c1} = 240Nm^{-1}s$, $b_{c2} = 50Nm^{-1}s$, $b_{c3} = 12Nm^{-1}s$, $k_{c0} = 7000Nm^{-1}s$, $k_{c1} = 3360Nm^{-1}s$, $k_{c2} = 650Nm^{-1}s$, $k_{c3} = 160Nm^{-1}s$, $m_2 = 7{,}6kg$, $m_3 = 9{,}5kg$, $b_1 = 5000Nm^{-1}s$, $b_2 = 20Nm^{-1}s$, $b_3 = 5000Nm^{-1}s$, $k_1 = 10^5 Nm^{-1}s$, $k_2 = 3421Nm^{-1}s$, $k_3 = 0$, $F_0 = 100N$ [17].

Figure 5 presents the variation of the parameters of the contact line along the truck for a speed of v = 100 km/h, (below the critical ones). The stiffness of the contact line k_c varies between a minimum of 4134 N/m·s and a maximum of 11170 N/m·s; the damping coefficient is between the $38.11Nm^{-1}s$ and $542Nm^{-1}s$ and the catenary mass oscillates between 110 kg and 320 kg. These variations have constant amplitudes all along the truck and it can be considered that for this speed of the vehicle there are no problems regarding the power collecting on the vehicle.

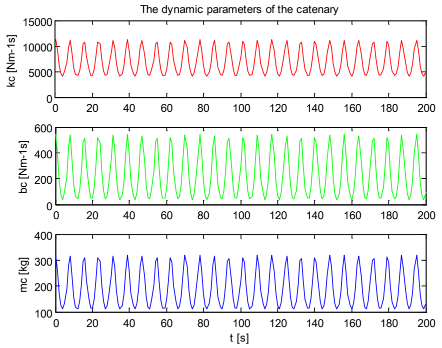

Figure 5. Parameters variation of the contact line for a speed of v = 100 km/h.

Figure 6 presents the variation of the parameters of the contact line on the same truck side. The speed of the pantograph is v = 150 km/h, which is below the critical speed. The maximum values for the stiffness coefficient of the contact line k_c oscillate between the $9954\ Nm^{-1}s$ and $11170Nm^{-1}s$ and a minimum of $4134Nm^{-1}s$.

The damping coefficient of the catenary b_c oscillates with values between $452.1Nm^{-1}s$ and $542Nm^{-1}s$, with a minimum of $38.04Nm^{-1}s$. The mass of the catenary has maximum values of 283.1 kg and 320 kg and a minimum of 110 kg. In these conditions it results that the contact line has relatively constant amplitudes and the energy transfer from the line on the vehicle is achieved in good conditions.

Figure 7 presents the variation of the parameters of the contact line on the same truck side. The pantograph has the critical speed given by the relation

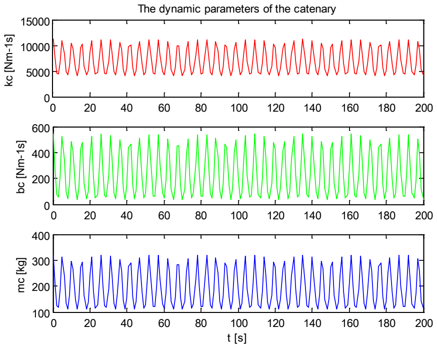

Figure 6. Parameters variation of the contact line for the speed v = 150 km/h.

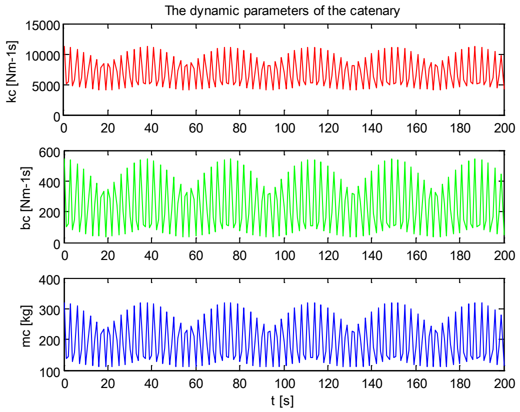

Figure 7. Parameters variation of the contact line for the speed v_{k1max} = 266 km/h.

(8), v_{k1max} = 266 km/h. From the graphics it results a variation of the amplitudes with a period time of T = 38s.

The stiffness coefficient of the contact line k_c has the same maximum and minimum ($11170Nm^{-1}s$ and $4134Nm^{-1}s$) for t = 18 s, 56 s, 94 s, 132 s a.s.o.. For a period of time of T = 38s it has a different maximum and minimum, which are $8251Nm^{-1}s$ and $4132Nm^{-1}s$. The damping coefficient b_c has the maximum and minimum as above ($542Nm^{-1}s$ and $38.04Nm^{-1}s$) for the same moments in time $t = (18s, 56s, 94s, 132s)$. Also, for a period time of T =38 s, it has maximum and minimum values of $327.1Nm^{-1}s$ and $38.13Nm^{-1}s$. The mass of the catenary has also a variation with the period time T =38 s, with values of 231.7 kg and 110.1 kg.

Considering these oscillations, the movement of the pantograph could not be considered being safe, because at any of these moments it could appear detachments between the collector head and the contact line, with negative effects in power collecting on the vehicle. With the above parameters, considering the model in Figure 3 and the relations (27-29), there are estimated the variation of the contact force, see Figure 8, and the variation of the contact point, Figure 9, for a vehicle speed of 100 km/h and a critical speed of v_{k1max} = 266 km/h. In Figure 8(a) and 8(b) it can be observed that the contact force oscillates around the values of 100 N, with a maximum of F_{max} = 113.2 N and a minimum of F_{min} = 85.78 N.

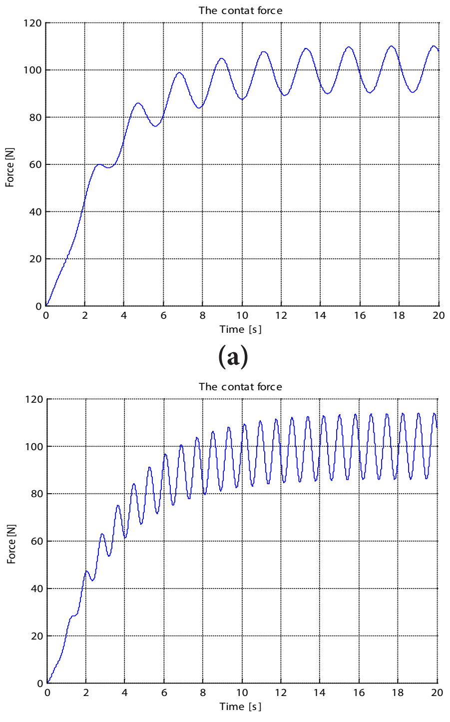

(a)

(b)

Figure 8. Variation of the contact force. **(a)** v = 100 km/h; **(b)** v_{k1max} = 266 km/h.

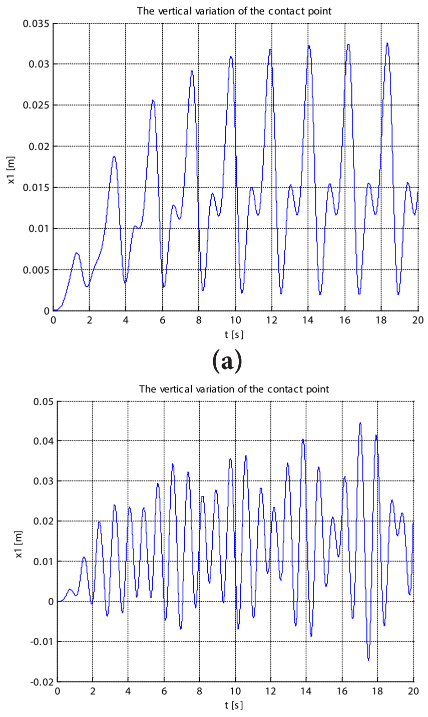

(a)

(b)

Figure 9. Variations of the contact point: **(a)** v = 100 km/h; **(b)** v_{k1max} = 266 km/h.

(a) presents the lift of the contact point for a speed of the vehicle of 100 km/h, with positive variations between a minimum of x_{1min} = 0.002 m and a maximum of x_{1max} = 0.032 m. Figure 9(b) shows the variation of the contact point for the critical speed of 266 km/h. In this case there is a lift of 0.01 m at t = 1.5 s, and after that it appears some oscillations with negative amplitudes.

Thus, the contact point has a minimum of x_{1min} = -0.014 m and a maximum of x_{1max} = 0.044 m. These negative values give the detachments of the collector head from the contact line with consequences in power collecting interruptions on the vehicle.

4. Experimental Analysis of the Pantograph-Catenary System at Critical Speed

An experimental stand was developed in order to study the pantograph-catenary system's behaviour at different speeds shown in Figure 10.

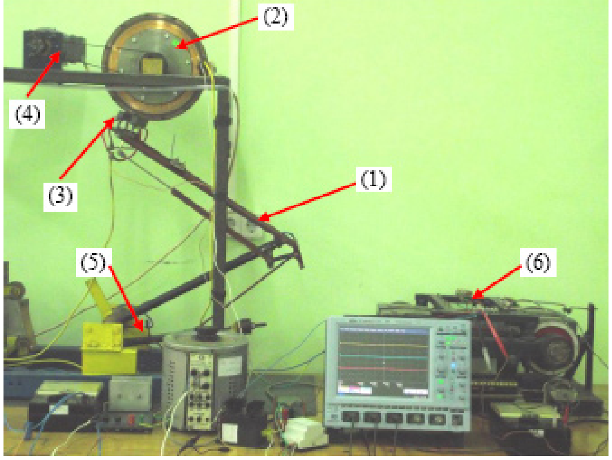

Figure 10. Pantograph-catenary experimental stand.

An asymmetrical pantograph, 1. At a scale of 1:4 as regarding a real system (a real pantograph used on an electric locomotive and the distance between the two consecutive droppers) is used. A rotating copper disk, 2. With a diameter of Φ_{Cu} = 477 mm and a thickness of g_{Cu} = 8 mm is used as a contact line. 3. The rotating disc is in contact with the graphite skate. The disc has an eccentricity and it is elastically fixed in order to reproduce the oscillations of the contact line.

The disc is droved by an electric motor, 4. Controlled with a static converter for linear speeds v_D corresponding from 0 to 75 km/h. For the scale 1:4 the maximum corresponds to a train speed of 300 km/h. It is to mention that the pantograph has the classical mechanical lifting (springs) system, 5. Used for the main lifting force. The pantograph model has a low inertia, a good lateral stability, a constant contact pressure for a specific height and a low wear of the carbon skate. As load it is used a model bogie, 6. With two D.C. traction motors. The speed of the vehicle is simulated by the rotation of the copper disk. Thus, for a speed of 100 km/h, the disk rotates with a speed of 1109.1 rot/min and for 266 km/h the disk rotates with 2959.7 rot/min. The disk is mounted with an eccentric axle in order to reproduce closely the real contact line between two suspension points. Thus, it will result a sinusoidal trajectory of the contact point.

With the aim of recording the current and voltage waveforms, a digital oscilloscope type LeCroy Wave Surf 400 has been used. On the first channel (C1) the load current has been recorded using a current probe Hall LA 55P type, with a transform ratio of 50A/50 mA. A resistance standard of 100 Ω was used, which, finally, resulted in a voltage ratio of 50A/5V. The voltage at the terminals of the traction motor was recorded on channel 2 (C2). The voltage signal was acquired by a voltage probe Hall LV 100-100 type, with a voltage ratio of 100V/50mA. Using a 100 Ω standard resistance it results in a transform ratio of 100V/5V. The waveform of the contact voltage was recorded directly on channel 3 (C3).

Figure 11 shows the experimental waveforms for current and voltage for the speed of 100 km/h. In this case the waveforms haven't important variations: there are no important variations of the load current (Channel C1) and the voltage on the traction motor (Channel C2) and the voltage drop between the pantograph and the contact line (Channel C3).

These waveforms have been recorded at the speed of 100 km/h, lower than the critical speed of 266 km/h, hence, at this speed; there are no risks of detachments of the collector head from the disk.

Figure 12 shows the experimental waveforms for current and voltage for the critical speed of v_{k1max} = 266 km/h. In this case the waveforms have important oscillations. It can be observed that there is no variation in the load current (Channel C1) but there are variations of the voltage of the motor (Channel C2). Also, it can be notice that the voltage across the pantograph and the contact line (Channel C3) has important variations, between 250 mV and almost 2 V. Hence, at the same value of the load

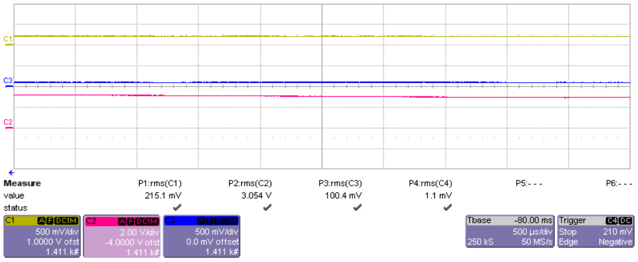

Figure 11. Experimental waveforms for current and voltage for v=100 km/h.

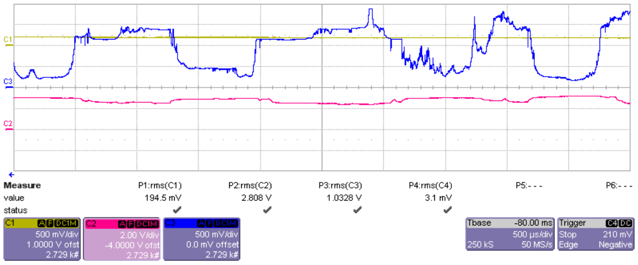

Figure 12. Experimental waveforms for current and voltage at v_{k1max} = 266 km/h.

current, the contact resistance between the pantograph and the contact line increases and that means power losses at high values.

The contact voltage has large variations because of the detachments between the collector head and the disk with the risk of occurring an electric arc between them. These tests show the influence of the critical speed over the pantograph-catenary system's behaviour.

5. Conclusions

In order to provide a permanent contact between the collector head and the contact line the pantograph has to trace closely the contact line. Because of the contact force of the pantograph the contact wire is lifted up, and, in combination with the vehicle's movement, it results a movement of the deformation of the contact line. This longitudinal deformation of the contact line propagates along the truck as elastic waves. As the speed of the vehicle increases, there also increases the speed of the propagation of the deformation, approaching the critical speed of the catenary.

This paper presents an analysis of critical speeds considering some models regarding the critical speed estimation on the pantograph-catenary system related to the resonance phenomenon in the pantograph-catenary system. A comparative analysis is also presented for the critical speed depending on the mechanical tensions in the contact wire and its mass. It was analyzed the mathematical model of the interaction pantograph-catenary and were performed simulations at the speeds of the train close to the critical speeds. The variations of the contact force, the damping coefficient of the catenary, the stiffness coefficient along a span of the catenary, and the mass of the catenary distributed along a span are analysed as simulations results. On an experimental stand it is analyzed the interaction pantograph-catenary at critical speed. Records of the pantograph-catenary system's behaviour show the influence of the critical speeds over the power collecting system and knowing the critical speeds on different trucks, it can be established the maximum speeds for the railway vehicles.

6. References

1. Rachid A. Pantograph Catenary Control and Observation using the LMI Approach. 50th IEEE Conference on Decision and Control and European Control Conference (CDC-ECC); Orlando, FL, USA. 2011. p. 2287–92.
2. Collina A, Bruni S. Numerical simulation of pantograph-overhead equipment interaction: Vehicle system dynamics. Int J Veh Mech Mobility. 2002; 38(4):261–91.
3. Walters S, Rachid A, Mpanda A. On modelling and control of pantograph catenary systems. International Conference on Pantograph Catenary Interaction Framework for Intelligent Control (PACIFIC); Amiens, France. 2011 Dec 8–9.
4. Plesca A. Thermal analysis of a traction system with double conducting points in steady state conditions. Electr Power Syst Res. 2013; 97:126–32.
5. Plesca A. Thermal analysis of sliding electrical contacts with mechanical friction in steady state conditions. Int J of Thermal Sciences. 2014; 84:125–33.
6. Jorge A, Joao P, Manuel P, et al. A computational procedure for the dynamic analysis of the catenary-pantograph interaction in high-speed trains. J Theor Appl Mech. 2012; 50(3):681–99.
7. Dimitrovova Z, Varandas JN. Critical velocity of a load moving on a beam with a sudden change of foundation stiffness: Applications to high-speed trains. Comput Struct. 2009; 87: 1224–32.
8. Huang H, Chrismer S. Discrete element modelling of ballast settlement under trains moving at critical speeds. Constr Build Mater. 2013; 38:994–1000.
9. Lee JH, Kim YK, et al. Performance evaluation and design optimization using differential evolutionary algorithm of the pantograph for the high speed train. J Mech Sci Technol. 2012; 26(10): 3253–60.
10. Plesca A. Electric arc power collection system for electric traction vehicles. International Journal of Electrical Power and Energy Systems. 2014; 57:212–21.
11. Bruni S, Bucca G, et al. Numerical and hardware-in-the-loop simulation of pantograph-catenary interaction. Pantograph Catenary Interaction Framework for Intelligent Control Conference (PACIFIC); Amiens, France. 2011 Dec 8–9.
12. Nituca C. Probleme de captare a curentului in tractiunea electromecanica [Ph.D. thesis]. Romania: Romanian, Technical University of Iasi; 2003.
13. Cantemir CG. Cercetari privind dinamica pantografelor asimetrice, (in Romanian) [Ph.D thesis]. Romania: Technical University of Iasi; 1997.
14. Pasca N, Scorţeanu R. Influenţa diversilor parametri asupra traiectoriei punctului de contact dintre pantograf si catenars, la viteze mari de circulatie, studiata pe calculatorul analogic (in Romanian). Revista Transporturilor si Telecomunicatiilor. 1974; 4:210–5.
15. Chen Z, Jian Z, Jidong H. The evaluation of the electromagnetic emission from high-speed railway by pantograph and network parameters. Asia-Pacific Conference on Environmental Electromagnetics (CEEM'2000); Shanghai, China. 2000 May 3-7. p. 279–84.

16. Turos G. Vehicule neconvenţionale de tractiune feroviara (in Romanian). Vol. 1. Timisoara: Traian Vuia IP, (editors). 1976. p. 42.
17. Cho YH. Numerical simulation of the dynamic responses of railway overhead contact lines to a moving pantograph, considering a nonlinear dropper. J Sound Vib. 2008; 315:433–54.
18. Mokrani N, Rachid A. A robust control of contact force of pantograph-catenary for the high-speed train. European Control Conference; Zurich. 2013 Jul 17-19. p. 4568–73.
19. Pisano A, Usai E. Contact force estimation and regulation in active pantographs: An algebraic observability approach. Proceedings of 46th IEEE Conference on Decision and Control; New Orleans, Louisiana. 2007 Dec 12–14. p. 4341–6.

Nomenclature

b_c – Damping coefficient of the catenary;
E_c – Kinetic energy of the catenary;
E_{cmax} – Maximum kinetic energy of the catenary;
E_{pmax} – Maximum potential energy of the catenary;
F_k – Contact force between the collector head and the contact wire;
F_0 – Force of the resort of the pantograph;
$f_q(t)$ – Control force on the lower arm of the pantograph;
$f_c(t)$ – Control force on the upper arm of the pantograph;
h – Vertical amplitude of the contact wire;
h_0 – vertical amplitude of the contact wire in the middle of the span;
h_{0max} – maximum vertical amplitude of the contact wire in the middle of the span;
k_c – Stiffness coefficient along a span of the catenary;
k_{c0} – Medium stiffness coefficient;
L – Distance between two successive suspensions of the catenary;
M – The sum of the equivalent mass of the pantograph and of the contact wire;
m_p – Total mass of the pantograph;
m_{c0} – Linear mass of the contact line;
m_c – Mass of the catenary distributed along a span;
T_0 – Mechanical tension into the messenger wire in standstill;
T – Mechanical tension into the messenger wire during the pantograph movement;
T_f – Mechanical tension into the contact wire;
v – Train speed; $b_c(t)$
v_k – Critical speed of the pantograph–catenary system;
y_0 – Cross static elasticity of the contact wire;
α_m – Coefficient of irregularity for the mass of the catenary;
α_k – Coefficient of irregularity for the stiffness of the catenary;
$\nu(a)$, $\nu(b)$ – Free oscillation frequency for the catenary.

Journal of
Energy
Technology

JET Volume 14 (2021) p.p. 47-55
Issue 2, October 2021
Type of article 1.01
www.fe.um.si/en/jet.html

GEOMETRY DESIGN AND ANALYSIS OF AN ELECTRIC BUS FOR THE INTERIOR THER-MAL MODELLING

DIZAJNIRANJE IN ANALIZA TERMIČNEGA MODELIRANJA NOTRANJOSTI ELEKTRIČ-NEGA AVTOBUSA

Costică Nițucă[1], Gabriel Chiriac[1ℜ], Georgel Gabor[1], Ilie Nucă[2], Vadim Cazac[2], Marcel Burduniuc[2,]

Keywords: heat transfer, electric bus, passenger comfort, geometry design, thermal modelling

Abstract

The heating, ventilation and air-conditioning (HVAC) system represents the main auxiliary load for any type of bus. Being the most significant energy-consuming auxiliary load for the electric bus, it must be given special attention in an electric bus system design. To study the heat transfer and thermal optimization for passenger comfort in the electric bus computer-aided design (CAD) is used. The geometry of an electric bus interior is designed considering the main components of the vehicle: passenger cabin, driver's cabin, windows, walls, and seats. Materials of the same type as those used in the real bus are considered for the geometry model. Based on the heat transfer theory, a thermal model and simulations are made for the heat transfer inside the electric bus. The simulated data are compared with measurement data, and based on these, it can be concluded that the thermal model of the electric bus can be validated and used further for a wide variety of thermal simulation types.

[ℜ] Corresponding author: Lecturer Ph.D., Chiriac Gabriel, Tel.: +040 727 645058, Mailing address: Bd. Prof. Dimitrie Mangeron, nr. 21-23, 700050 Iasi, Romania, E-mail address: gchiriac@tuiasi.ro

[1] "Gheorghe Asachi" Technical University from Iasi, Faculty of Electrical Engineering, Romania

[2] Technical University of Moldova, Chisinau, Faculty of Power and Electrical Engineering, Republic of Moldova

Povzetek

Sistem ogrevanja, prezračevanja in klimatizacije (HVAC) predstavlja glavno dodatno obremenitev za vse vrste avtobusov. Ker gre za sistem z največjo porabo energije pri električnem avtobusu, mu moramo posvetiti posebno pozornost pri dizajniranju električnega avtobusa. Pri študiji prenosa toplote in optimizaciji v smislu udobja potnikov smo uporabili računalniško podprto dizajniranje (CAD). Postavitev notranjosti električnega avtobusa je zasnovana glede na glavne komponente vozila: prostor za potnike, prostor za voznika, okna, stene in sedeže. V oblikovanem modelu so uporabljeni materiali iste vrste kot v realnih avtobusih. Na podlagi teorije o prenosu toplote smo naredili model in simulacije prenosa toplote znotraj električnega avtobusa, nakar smo primerjali podatke iz simulacije s podatki iz meritev. Iz izvlečkov omenjene primerjave lahko zaključimo, da je termični model električnega avtobusa mogoče validirati in nadalje uporabiti za najrazličnejše termične simulacije.

1 INTRODUCTION

Energy consumption per trip for an urban vehicle is a major design factor, which is influenced by the driving pattern, the topology, the climate conditions and the payload. The energy required by the auxiliaries is not negligible, so that the efficiency enhancement of the auxiliaries could lead to an improvement of global energy use in the vehicle, which is particularly important for innovative means of transport which are characterised by a limited range, such as that of an electric bus.

The importance of energy consumption for non-traction needs is revealed when considering the percentage distribution of energy consumption in annual scales for a bus system *[1]*: traction needs represent about 52%, non-traction needs on stopping about 13% and non-traction needs for route operation about 35%.

A key parameter affecting the auxiliary energy consumption is the external temperature. A rise of 10 ^{o}C can lead to an energy consumption increase of about 0.75kWh/km *[2]*.

An important input parameter is the setpoint temperature within the electric bus cabin. Usually, the setpoint is kept at a constant temperature that is comfortable for the passengers inside the bus, but the “comfort aspect” is a relative aspect concept. What a person perceives as a comfortable temperature depends on many parameters, such as *[3]* air humidity, air velocity, radiation, seasonal effects, and metabolism.

Attention is given to the optimization of the thermal system of electric vehicles. This functionality can be synthesized as:

1. Dynamic temperature setpoint: By considering the different aspects of comfort, an energy-optimized temperature setpoint control can be implemented. For example, a temperature setpoint can vary over the day to account for ambient temperature changes. This results in lower energy consumption of the HVAC system *[3]*.

2. Pre-conditioning: The energy that is required for the heat to control the cabin climate is taken from the battery. Therefore, this might affect the driving range of the vehicle. Besides minimizing the energy consumption of the HVAC system, pre-conditioning can also be applied to improve the vehicle’s driving range of the vehicle. Pre-conditioning means that the cabin

climate is already controlled towards the desired temperature while the vehicle is still connected to the charger, either in the depot or en route at terminal stops.

Heat transfer theory, heat balance method and U-Value definition are the foundations used in calculations and modelling *[4]*. Based on the heat transfer theory, there are three mechanisms for transferring heat: conduction, convection and radiation.

The Heat Balance Method is a common method for calculation of heating and cooling loads in a space or zone *[4]*. The total heat released into the cabin is given by:

- Ambient load, as the thermal load caused by the temperature gradient between inside air and the ambient temperature,
- Radiation loads,
- Metabolic load, generated by human body,
- Ventilation load, as the flow of fresh air,
- Engine/Motor load, due to the bus motors,
- AC load, for keeping the internal temperature in the comfort zone by heating or cooling.

The heating, ventilation and air-conditioning (HVAC) system represents the main auxiliary load for any type of bus. Being the most significant energy-consuming auxiliary load for the electric bus, it must be given special attention in an electric bus system design. The HVAC systems usually implemented in electric buses is composed from a rooftop unit comprising a compression refrigeration machine and several heat exchangers for air cooling and heating. Heating can be also performed by heaters placed at the floor level and supplied from the main power supply, or from an auxiliary supply system (such as a battery), *[5-8]*.

Energy needs for resistance heating can significantly increase the vehicle’s energy consumption. From measurements on a 12 m electric bus *[9]*, it is estimated the average electric power necessary to keep the interior of the vehicle at 17 ^{o}C on a cold winter day with ambient temperature of approximately -10 ^{o}C is around 24 kW. Assuming a specific energy demand for traction and non-HVAC auxiliaries of 1.2 kWh/km, a plausible value according to measurements, a constant 24 kW load for heating will increase vehicle consumption by 1.3 kWh/km at an average velocity of 18 km/h and 2 kWh/km at an average velocity of 12 km/h.

Possible measures to reduce energy consumption of the HVAC system include improved thermal insulation, double-glazed windows, door air curtains and using improved control systems. Differently from the conventional HVAC system on current buses, *[10]* an integrated air-conditioning and heating system specifically for an electric bus are proposed. For an i-HVAC (integrated HVAC) system, an electrical heat pump type should be considered.

2 HEAT TRANSFER MODEL

Thermal conduction is estimated considering Fourier's Law, with heat flux given by:

$$q=-k\cdot dT/dx \text{ [W/m2]} \tag{2.1}$$

where:

q is the heat flux,

k is the thermal conductivity, [W/m^{2}K],

T is temperature, [^{o}C],

x direction of the heat flux, [m].

Thermal convection is considered for the heat transfer between the air and the solid structure of the bus. Newton's formula is considered in this case for the heat flux estimation:

$$q=-h\cdot(T_s-T_f) \text{ [W/m2]} \tag{2.2}$$

where:

q is the heat flux,

h heat transfer coefficient, [W/m^{2}K],

T_s is the temperature of the solid, [^{o}C],

T_f is the temperature of the fluid, [^{o}C].

3 DESIGNING THE INTERIOR GEOMETRY MODEL OF THE ELECTRIC BUS

To study the heat transfer and thermal optimization for passenger comfort in the electric bus, computer-aided design (CAD) is used, COMSOL Multiphysics, which has a special application for thermal aspects, the Heat Transfer Module. In order to simulate the heat process inside the bus, the following steps are to be followed: geometry modelling, physics settings, solving, and results.

The geometry of the electric bus is constructed as a basic geometry and is composed from: passenger cabin; driver's cabin; bus walls; windshield; windows; floor; roof; doors; wheels; passengers seats; electric air heat units inside the passenger cabin; heating block inside the driver's cabin.

The dimensions of the electric bus are designed in the geometry model according to the actual dimensions of the real vehicle, an E321 electric bus used currently in public transportation in Chisinau, Republic of Moldova *[11, 12]*. This is a low-floor compartment vehicle with a capacity of about 100 passengers, with a 150kW electric motor, with four heating units inside the passenger cabin. The components of the vehicle described above are also designed on the geometry model considering their actual dimensions on the electric bus. Thus, the model and the simulation results will be close to reality.

The first step to build the geometry model of the electric bus was to design the passengers' cabin and the driver's cabin. For the modelling and simulations these areas will be considered to be filled with air.

The second step in designing the geometry model is to design the exterior components, such as the front wall, rear wall, lateral walls, front windows (windshield), rear window, lateral windows and the doors. For this, a 2D representation was used (Figure 1), as a work plane design and plane geometry design. For each of these components, coordinates for the size, shape and position are transferred into the geometry model.

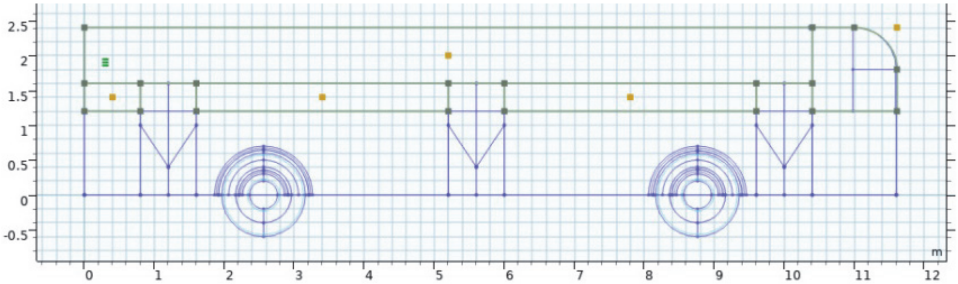

Figure 1: *2D design of the bus*

Having the main structure of the geometry model, the heaters can be designed inside the cabins. The passenger cabin is designed with four heaters and the driver's cabin with one heater (Figure 2). Thus, in the passenger cabin, the first heater is placed on the right side of the vehicle, next to the third door, a second heater is placed on the left side of the vehicle, in the middle area, the third heater is placed on the right side, after the second door, and the fourth heater is placed in front of the cabin, next to the glazed partition which separates the driver's cabin from the passenger compartment (Figure 2).

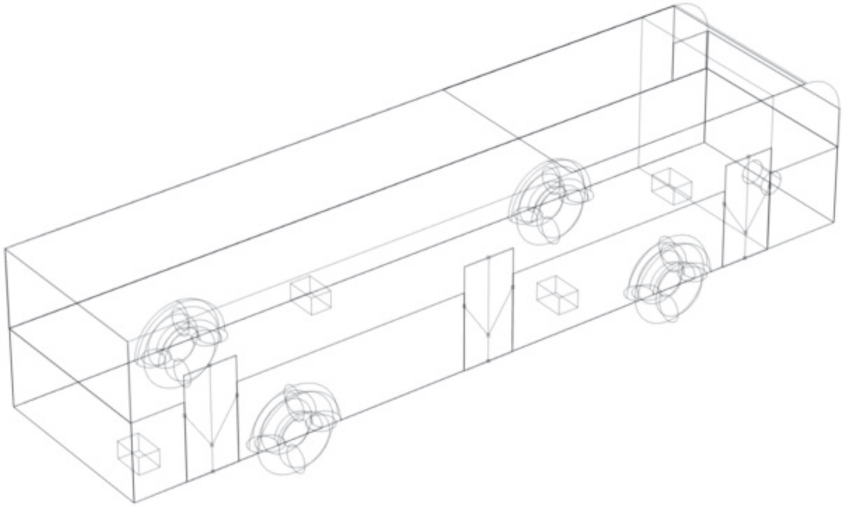

Figure 2: *Heater positions inside the electric bus*

A non-transparent view can be used for a better identification of some of the components, as in Figure 3, where the front door is selected to accentuate its position, dimensions, and properties. A 3D grid can be also displayed in order to estimate the spatial distribution of the components.

The last main component of the geometry model is the current collecting system of the electric bus. This system is placed on the vehicle roof and consists of two skates placed on two core bars, which assure the vehicle's energy supply when it operates in a non-autonomous way, like a trolley-bus (Figure 4).

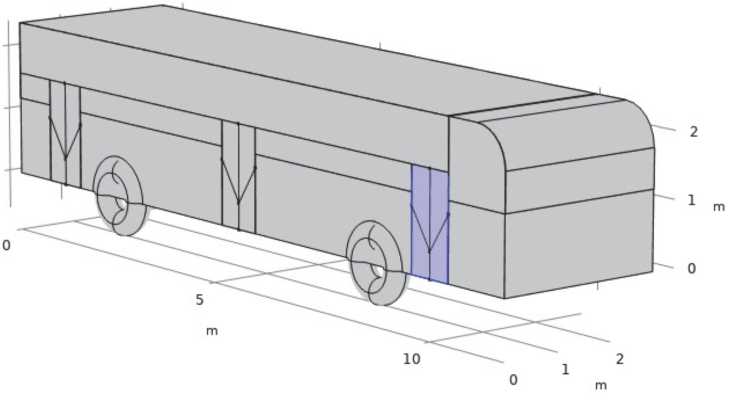

__Figure 3:__ Non-transparent view of the geometry model

The finalized geometry has 87 domains, 676 boundaries, 1351 edges, and 773 vertices. This results in the basic geometry model of the electric bus, which will be used for the simulations.

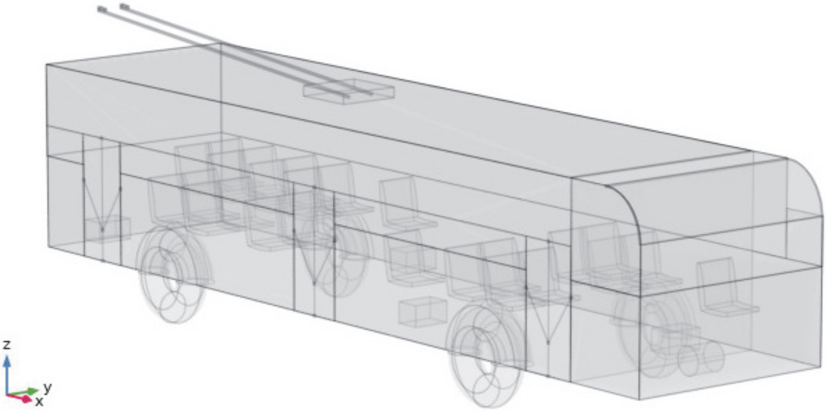

__Figure 4:__ The basic geometry model of the electric bus; transparent view

The materials considered for the components of the bus for the model are iron, glass, acrylic plastic, fibreglass and PMMA – polymethyl methacrylate. The interior volume of the bus is modelled as filled with air.

4 SIMULATION RESULTS AND ANALYSIS

The main results of the simulations based on the thermal model are shown in Figure 5. Figure 5 shows the temperature distribution inside the electric bus with a view from the right side of the vehicle. The temperatures are estimated at the surfaces of the bus components. It can be observed that the highest temperature, as expected, is at the heaters (40 °C), and the lowest temperature is at the exterior surface of the roof, next to the power collecting box system where the trolleys are attached (17.3 °C).

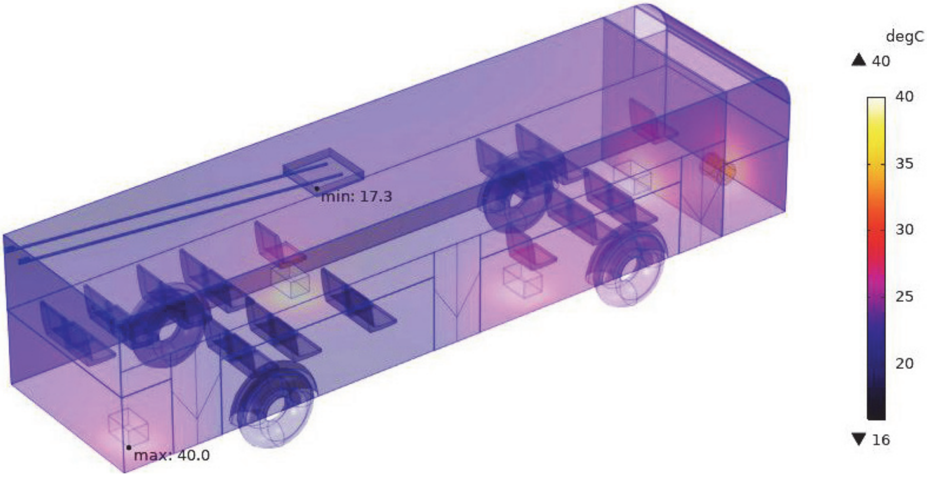

Figure 5: *Simulation results for the temperature distribution in the bus*

For a better visualization of the temperature distribution, it can be seen from the temperature variation along the electric bus that the higher temperatures are measured around the area where the heaters are placed and the lower temperature (between 17 °C and about 25 °C) in the area farthest from the heaters. For the validation of the thermal model, some experimental measurements of temperatures were taken at the various points in the interior of the electric bus. The results of the simulations were compared with the measured temperatures.

The temperatures were measured in different areas inside the electric bus with a point-and-shoot infrared camera (FLIR thermal-imaging camera). The temperature measured in the driver's cabin is 27.8 °C, quite comfortable for the driver. The temperature measured inside the electric bus, next to a heater, is 41.3 °C. These measurements are compared with the values resulting from the thermal simulation presented above. As seen in Figure 5, the simulated maximum temperatures inside the driver's cabin are between 25.2 °C and 27.9 °C, which are quite close to the measured temperature of 27.8 °C (Figure 6). As for the heaters, the simulated temperature is 40 °C, which is close to the measured one of 41.3 °C. Comparing the simulated and measured temperatures, it can be concluded that the thermal model of the electric bus can be validated as correct and be used further for a wide variety of simulation types in order to estimate the optimal solution to improve heat transfer inside the electric bus.

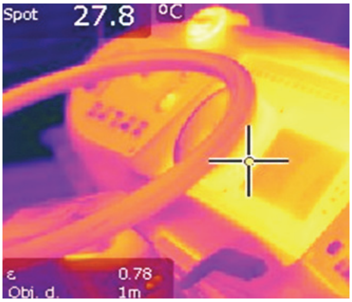

Figure 6: *Temperature measured with a thermal-imaging camera on the driver's cabin*

5 CONCLUSIONS

The geometry of an electric bus interior is designed considering the main components of the vehicle: passenger cabin, driver's cabin, windows, walls, seats and the main materials in accordance with a real bus. To study the heat transfer into the electric bus, a computer-aided design is used based on the heat transfer theory. A thermal model and simulations are made for the heat transfer inside the electric bus. The simulated data are compared with measurement data, and based on these data, it can be concluded that the thermal model of the electric bus can be validated and used further for various thermal simulations.

References

[1] **I. Evtimov, R. Ivanov, M. Sapundjiev:** *Energy consumption of auxiliary systems of electric cars*, MATEC web of conferences, EDP Sciences Vol. 133, p. 06002, 2017

[2] **M. Bartłomiejczyk, R. Kołacz:** *The reduction of auxiliaries power demand: The challenge for electromobility in public transportation*, Journal of Cleaner Production, 252, 119776, 2020

[3] **M. M., Hasan, J., Maasc, M. El Baghdadia, R. de Grootc, O. Hegazya:** *Thermal Management Strategy of Electric Buses towards ECO Comfort*, In proceedings of 8th Transport Research Arena Conference, TRA, 2020

[4] **H. Sahraei:** *Interior Climate U-Value calculation and optimization for electric buses at Volvo buses,* Master's thesis, Department of Mechanics and Maritime Sciences Chalmers University of Technology Gothenburg, Sweden, 2020

[5] **D. Göhlich, T.-A. Ly, A. Kunith, D. Jefferies:** *Economic assessment of different air-conditioning and heating systems for electric city buses based on comprehensive energetic simulations,* In EVS28 International Electric Vehicle Symposium and Exhibition, Kintex, Korea, May 3_6 (ed. Electric Vehicle Symposium (EVS)), 2015

[6] **M. Vražić, O. Barić, P. Virtič:** *Auxiliary systems consumption in electric vehicle*, *Przegląd* elektrotechniczny, Vol. 90, Iss. 12, p.p. 172-175, 2014

[7] **T. Zhang, C. Gao, Q. Gao, G. Wang, M. Liu, Y. Guo, Y.Y. Yan:** *Status and development of electric vehicle integrated thermal management from BTM to HVAC*, Applied Thermal Engineering, Vol. 88, p.p. 398-409, 2015

[8] **H. He, M. Yan, C. Sun, J. Peng, M. Li, H. Jia:** *Predictive air-conditioner control for electric buses with passenger amount variation forecast,* Applied energy, Vol. 227, p.p. 249-261, 2018

[9] **D. Göhlich, T. A. Fay, D. Jefferies, E. Lauth, A. Kunith, X. Zhang:** *Design of urban electric bus systems,* Design Science, Vol. 4, 2018

[10] **I. S. Suh, M. Lee, J. Kim, S.T. Oh, J.P. Won:** *Design and experimental analysis of an efficient HVAC (heating, ventilation, air-conditioning) system on an electric bus with dynamic on-road wireless charging*, Energy, Vol. 81, p.p. 262-273, 2015

[11] https://bkm.by/en/

[12] **V. Esanu, A. Motroi, I. Nuca, Iu. Nuca:** *Electrical Buses: Development and Implementation in Chisinau Municipality*, *Moldova*, 2019 International Conference on Electromechanical and Energy Systems (SIELMEN), 2019

Acknowledgement

This paper is a result of researches funded by the European Union on Joint Operational Programme Romania- Republic of Moldova – financed by the European Neighbourhood Instrument (ENI), Cross Border Cooperation (CBC), within the project: “ELBUS - Improving the cross-border public transportation using electric buses supplied with renewable energy”, project reference number 2SOFT/3.1/54.

Nomenclature

(Symbols)	(Symbol meaning)
h	heat transfer coefficient, [W/m^{2}K]
k	thermal conductivity, [W/mK]
q	heat flux
T	temperature, [^{o}C]
T_s	temperature of the solid, [^{o}C]
T_f	temperature of the fluid, [^{o}C]
x	direction of the heat flux, [m]